



UNIVERSITY OF CATANIA

Department of Electrical Electronic and Computer Engineering

PhD Course in Systems, Energy, Computer and Telecommunications Engineering

Claudio Tosto

Advanced Materials for Additive Manufacturing

Industrial PhD Project - XXXIV Cycle

Coordinator:

Prof. Paolo Pietro Arena

Tutor:

Prof. Gianluca Cicala

Academic year 2021/22

*Learning is the only thing the mind never exhausts,
never fears, and never regrets.*

Leonardo Da Vinci

Abstract

The Industrial PhD project “Advanced Materials for Additive manufacturing” (AMA), funded by MIUR, is focused on the development of novel materials for additive manufacturing (AM) and technologies to exploit the use of AM in composite’s manufacturing. The research carried out in the AMA project focused on: the development of innovative reinforced materials for use in AM; use of innovative polymeric materials as soluble mandrel or permanent molds in the manufacture of fiber-reinforced composite materials; use of AM for metal inserts. In terms of industrial impact, AMA research strived to develop new AM materials and technologies focusing, especially, on their application in the composites manufacturing field. Industry interest in this field is high with more companies using AM for ready-to-use components (FFF/FDM printing of fiber-reinforced composites) as well as tools (core materials and lay-up/trim tools) for the manufacturing of composite parts. However, still wide margins for improvement are possible in terms of material performance, cost, and usability. The research was carried out by first studying specific methodologies for mechanical testing of FDM (Fused Deposition Modeling) parts, then formulating and studying blends for the printing of AM mandrels useful for the application of composite molds for AM technologies varying from FDM to LCD. Finally, time and costs analyses of the 3D printing approaches developed during the PhD activity were carried out.

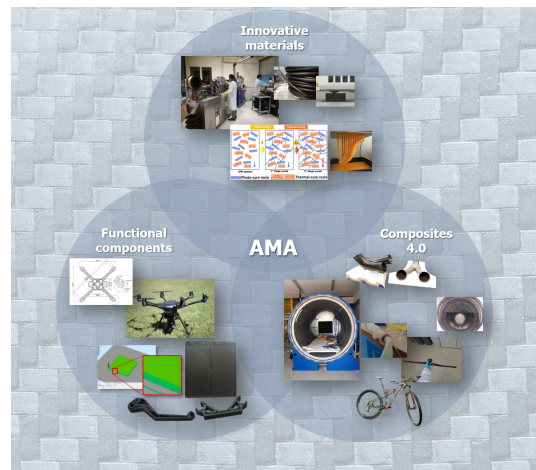


Figure 1: Graphical abstract of the AMA PhD project.

Contents

Thesis structure	1
1 State of the Art on AM	5
1.1 FDM/FFF standards and materials	5
1.2 Composite Tooling	7
1.3 LCD Printing	7
1.4 Metal-filled filament for FFF	9
2 Fiber reinforced filaments	11
2.1 CF-reinforced filaments production	11
2.2 Mechanical Characterization	21
2.2.1 Mechanical testing for FDM/FFF materials	21
2.2.2 Mechanical characterization of CF-reinforced FFF components	34
3 AM materials and techniques for Composite Tooling	41
3.1 AM mandrels	41
3.1.1 FDM mandrels	41
3.1.2 FDM/LCD comparison	45
3.2 LCD resin Formulation	52
4 Metal AM for Tooling and Inserts	61
4.1 Stainless steel 316L particles filled filament	62
4.2 Stainless steel 17-4 PH	73
Conclusions	79
Dissemination activity results	85
Awards	85
Indexed papers	85

National and international conferences ¹	87
Bibliography	101
A AM Standards and Filaments	103
B LCD Formulations	111
C Metal AM	115

¹In bold the name of the author who presented the work.

Nomenclature

AM	Additive manufacturing
ANOVA	Analysis of variance
ASTM	American Society for Testing and Materials
BJ	Binder Jetting
CAM	Computer Aided Manufacturing
CLIP	Continuous Liquid Interface Production
C _p	Heat Capacity
DETDA	Diethyltoluene diamine
DGEBA	Diglycidyl ether of bisphenol A
DMA	Dynamic Mechanical Analysis
DMLS	Direct Metal Laser Sintering
DoE	Design of experiments
DSC	Differential Scanning Calorimetry
E'	Storage modulus
EBM	Electron Beam Melting
EDS/EDX	Energy Dispersive X-ray Spectrometry
FDM	Fused Deposition Modeling
FDMet	Fused Deposition of Metals
FFF	Fused Filament Fabrication

Nomenclature

ILSS	Interlaminar Shear Strength
ISO	International Organization for Standardization
LCD	Liquid Crystal Display
LENS	Laser-Engineered Net Shaping
MIM	Metal Injection Molding
MJP	Multi Jet Printing
PEI	Polyetherimide
SBS	Short-Beam Strength
SEM	Scanning Electron Microscopy
SLA	Stereolithography
SLM	Selective Laser Melting
T _g	Glass-transition temperature
UTS	Ultimate Tensile Strength

List of Figures

1	Graphical abstract of the AMA PhD project.	v
2.1	Extrusion line for filament production. [QR-code link]	12
2.2	Particular of PLA CF-reinforced filament extrusion.	13
2.3	Frequency plots of filaments diameter.	14
2.4	3D printed samples by PLA (left) and PLA CF-reinforced (right) extruded filaments.	15
2.5	Average stress-strain curves.	16
2.6	Effects plots for the response: a) tensile modulus, b-c) tensile strength, d) elongation at break.	17
2.7	SEM image of a cross-section of a 3D printed PLA+CF30 sample with raster angle 0°.	18
2.8	3D printing components by PLA+CF30.	18
2.9	Laser Flash test setup.	19
2.10	Optical image of laser flash 3D printed samples: a) PLA+CF10, b) PLA+CF20, c) PLA+CF30.	20
2.11	Graphical abstract of the cited work.	21
2.12	DMA analysis on Ultem9085.	22
2.13	DSC analysis on Ultem9085.	23
2.14	Average stress-strain curve for tensile test.	24
2.15	Normal probability plot for: (a) Young's modulus; (b) ultimate tensile strength; (c) flexural strength; and (d) interlaminar shear strength.	25
2.16	Normal probability plot for tensile test (Young's modulus response).	26
2.17	Effects plot for tensile test (Young's modulus response).	27
2.18	Fracture surface morphology for a tensile sample (tan resin). Red ellipse highlights the adhesive failure on the transverse rasters. The green arrow highlights the yielded longitudinal rasters.	28
2.19	Average flexural stress versus displacement curves.	29
2.20	Average ILSS versus displacement curves.	30

2.21	Normal probability plot for SBS test. A: material; B: geometry; AB: interaction.	30
2.22	Effects diagram for SBS test.	31
2.23	SBS specimens: (a) side down is the face on the build platform during printing, side up is the opposite one; (b) TUP testing configuration is shown and it means that the fibers stretched belong to the side up.	31
2.24	SAverage ILSS vs. displacement curves.	32
2.25	Half normal effects plot for ILSS.	32
2.26	Interactions plot for ILSS.	33
2.27	Experimental setups for: a) tensile, b) SBS, b) impact test.	35
2.28	Effects plot for tensile test, response Young's Modulus (GPa): a) PA66-CF10, b) XT-CF20, c) Drying, d) Not Drying.	36
2.29	Effects plot for tensile test, responses Yield Stress a) and b), Elongation at Break c): a) Not Drying, b) Drying, c) Average raster angle.	36
2.30	SEM images for: a) XT-CF20 filament, b) XT-CF20 printed, c) PA66-CF10 filament, d) PA66-CF10 printed.	37
2.31	Frequency plots for the CF length of: XT-CF20 filament (a) and 3D printed parts (b); PA66-CF10 filament (c) and 3D printed parts (d).	38
2.32	Box plot of CF length for printed and filament materials.	38
2.33	Effect plot for SBS test (response ILSS).	39
2.34	Effect plot for impact test (response Total Energy).	39
2.35	Impact tested sample (PA66CF10).	40
3.1	One of the application of industrial interest for the company involved in the AMA PhD (handlebar bike).	41
3.2	Mandrel, mold and composite part.	42
3.3	Intake mandrel geometry: a) Hollow intake; b) Honeycomb intake. Mandrel cross section.	43
3.4	Stages of the dissolution process for the honeycomb intake.	45
3.5	Tan δ and E' versus temperature diagrams for the composite specimens treated for different time in the ultrasonic bath. The sample Rif refers to the untreated sample.	45
3.6	Model of the designed amphora to be manufactured in composites (all dimensions in mm).	46
3.7	AM mandrels: a) FDM - shell 1 mm, b) FDM - shell 2 mm c) FDM - collapsed sparse design after applying the autoclave pressure (5 bar), d) LCD - breakable 2 mm mandel with particular on the good internal surface quality.	47
3.8	Cost modeling for different printers and number of amphoras to be produced (varied from 1 to 21).	48

3.9	Box-shape mandrels.	49
3.10	3D printed mandrels, a) FDM; b) FFF; c) LCD.	49
3.11	Mandrels removal and composite parts: a) FDM; b) FFF; c) LCD.	51
3.12	Bar charts of mechanical properties: a) Flexural modulus; b) Flexural strength; c) Elongation at break.	51
3.13	Graphical abstract of the cited work.	52
3.14	DSC analysis on the hard cream resin: first scan (black); second scan (red).	54
3.15	DSC analysis on the epoxy-based blends in their uncured state.	54
3.16	Complex viscosity of the uncured epoxy-based blends: C (blue); CE7030 (red); CE5050 (green).	55
3.17	Printing trials for the CE7030 blend with the same printing conditions used for the cream resin (see Table 3.4).	56
3.18	Printing trials for the CE7030 blend with the optimized printing conditions after photocuring optimization (see Table 3.4).	57
3.19	Isothermal DMA curing test on LCD printed Hard Cream specimens: Storage modulus versus time.	58
3.20	Ramp rate DMA test on isothermally cured Hard Cream resin.	59
3.21	DMA analysis for the LCD printed sample after the post-curing cycle (isothermal cure at 140 C for 2 h, ramp at 2C/min to 180 C and hold at 180 C for 2 h).	59
3.22	Glass transition temperatures (T _g) obtained as Tan peaks measured by DMA plotted versus the epoxy content.	60
4.1	Graphical abstract of the cited work. [87]	61
4.2	Cross section SEM analysis of the Ultrafuse 316L filament: (a) magnification 50; (b) magnification 2500.	64
4.3	Knotted filament of Ultrafuse 316L.	64
4.4	SEM images of the mesostructure for the green printed parts using Ultrafuse 316L: (a) cross section (magnification 300); (b) cross section (magnification 2000); (c) contour (magnification 500); (d) contour (magnification 100).	65
4.5	SEM Images of the mesostructure for the green printed parts using the 17-4 PH system by Markforged: (a) contour (magnification 500); (b) contour (magnification 6000).	65
4.6	Optical image of the sintered 316L samples.	66
4.7	Tensile stress–strain curves for the sintered parts: (a) Ultrafuse 316L and (b) Markforged 17-4 PH. (Flat: red; upright: blue).	67
4.8	Morphology of the fracture surface of the fractured specimens manufactured using 17-4 PH: (a) flatwise; (b) upright.	68

4.9	Defects observed in the cross section of a flatwise sample of 17-4 PH: (a) porosity between the raster; (b) details of particle inclusions.	69
4.10	Inclusions observed on the raster's surface of an upright sample printed with 17-4 PH.	69
4.11	EDX spectra for the raster's surface and an inclusion observed for the 17-4 PH samples.	70
4.12	Morphology of the fracture surface of the fractured specimen manufactured using Ultrafuse 316L: (a) flatwise; (b) upright.	71
4.13	Mold geometry used for cost comparison.	72
4.14	Green and sintered molds.	73
4.15	Tensile test samples printed on Ultimaker S5.	75
4.16	Green and sintered parts of one printing profile (printing profile strong).	76
4.17	Radar chart for 17-4 PH sintered tensile samples.	77
A.1	Calibration cubes from a printing with wrong settings.	103
A.2	Calibration cubes from optimized printing.	103
A.3	ANOVA table for tensile modulus response.	104
A.4	ANOVA table for tensile strength response.	105
A.5	ANOVA table for elongation at break response.	105
A.6	Collected data for tensile test of CF-reinforced filaments.	109
B.1	Data obtained from the DSC analysis of the uncured blends.	111
B.2	Sample part for LCD printing.	111
B.3	Width overcure: (a) negative, resin not fully cured; (b) null, properly cured resin; (c) positive, resin over cured.	112
B.4	Comparison of the properties of epoxy based blends with some commercial LCD/DLS-Dual Curing resin. *Producers reported HDT rather than Tg.	113
C.1	Slicing view of the 17-4PH samples: a) Upright and flatwise build orientations; b) Infill of the upright samples; c) Infill of the flatwise samples.	115
C.2	Tensile test configuration.	116

List of Tables

2.1	ID of studied formulations.	12
2.2	Factors and levels studied in DoE plan.	14
2.3	Average tensile properties. Standard deviation is depicted in brackets. RA: raster angles, E: tensile modulus, UTS: ultimate tensile strength, Eb: elongation at break.	15
2.4	Comparison of PLA filaments.	17
2.5	Thermal diffusivity of 3D printed samples.	19
2.6	ANOVA table for tensile test (response is Young's modulus).	24
2.7	ANOVA table for tensile test (response: UTS).	25
2.8	ANOVA table for flexural test (response: flexural strength).	27
2.9	ANOVA table for ILSS test (response: short-beam strength).	29
2.10	Factors and levels of the designed plan.	35
3.1	FDM settings for prining tooling.	42
3.2	Cost breakdown for the different manufacturing strategies. The unit for the prepreg GG200TDT121R is square meter.	44
3.3	Resin formulations studied.	53
3.4	LCD printing conditions used for specimens manufacturing.	53
3.5	Average mean values and standard deviations (Std Dev) of the printing trials on the square prism for the LCD printing optimization with the epoxy-based blends.	57
4.1	Printing settings for the Ultrafuse 316L.	62
4.2	Standard (ASTM D638) and Green part dimensions for Ultrafuse 316L samples.	63
4.3	Standard (ASTM D638) and Green part dimensions for Ultrafuse 316L samples.	63
4.4	Standard (ASTM D638) and Green part dimensions for Ultrafuse 316L samples.	67

4.5	Tensile properties for the sintered parts produced in this paper. The properties reported in the technical data sheet of the producer are reported for comparison. *The data were extracted from the technical data sheet (TDS) released by the producer (BASF for the 316L and Markforged for the 17-4 PH). **The data were extracted from the technical data sheet released by Desktop Metal with their Studio System™.	67
4.6	Tensile properties for the 17-4 PH upright sample corrected to account for the real load bearing area.	69
4.7	Mechanical properties for 316L and 17-4 PH processed by different technologies. DMLS: Direct Metal Laser Melting; SLM: Selective Laser Melting; MIM: Metal Injection Molding, EBM: Electron Beam Melting. YS: Yield Strength; TS: Tensile Strength; TM: Tensile Modulus; Sb: Strain at Break.	72
4.8	Cost modelling comparison for the sample mold produced by 316L: Fused Filament Fabrication (FFF) vs. SLM.	73
4.9	Printing parameters for Ultrafuse 17-4 PH.	74
4.10	Density and porosity of sintered parts.	76
A.1	Printing parameter for PLA and PLA CF-reinforced on Ultimaker S5.	104
A.2	Tensile test experimental results obtained from 20 runs.	106
A.3	Flexural test experimental results obtained from 20 runs.	107
A.4	SBS test experimental results obtained from 20 runs.	108

Thesis structure

The aim of the proposal is the study of Advanced Materials for Additive Manufacturing (AMA). The research carried out in the AMA PhD project was focused on the following research activities:

- development of innovative materials for additive manufacturing;
- use of innovative polymeric materials for soluble mandrels or permanent molds to be used in the manufacture of fiber reinforced composite materials;
- use of innovative metal filled materials to print functional part such as mould or inserts

From the industrial perspective, the AMA PhD project focused on the development of novel fiber reinforced materials for AM, but also on the use of AM technologies in real production replacing or integrating conventional manufacturing process. The latter was focused mostly in the field of fiber reinforced polymers manufacturing of hollow and complex shaped parts. In this case, the industrial interest is strong as demonstrated by more companies integrating AM materials and related technologies into their manufacturing processing.

Different products are industrially relevant already as ready-to-use “as-build” (3D printing - FFF/FDM - of fiber-reinforced composites), and as an aid (“core material” or “lay-up/trim tool”) for the production of composite components.

The research activity carried out during the AMA PhD project addressed three critical key areas:

- the study of specific methodologies for testing components produced by the FDM (Fused Deposition Modeling) process;
- formulations and study of blends for printing AM mandrels useful for the application of composite tooling;
- time and cost analysis of 3D printing applications for an industrial company.

AMA PhD project is entirely centered on the so called "Intelligent Factory" area as defined by the MIUR research strategy described in the "Strategia Nazionale di Specializzazione Intelligente" (SNSI). SNSI listed as sub-areas included in the "Intelligent Factory" area: Production and use of Innovative Materials; Technologies for sustainable manufacturing; Advanced manufacturing processes. Among the customization economies, AMA focused on the cancellation of production constraints to free the construction geometries and on the incidence of variable costs through the comparative analysis referred to technological materials for advanced uses.

The PhD thesis is organized in four chapters. Chapter 1 describes a brief review of the state of the art for AM materials and processes which are of relevant interest for the topics studied in the AMA PhD project.

Chapter 2 is focused on the study of fiber reinforced filaments for FDM. This type of filaments are of potential interest for the making of permanent mold or as self-standing structures. The latter is finding increasing application as substitute of reinforced injection molded parts or, in perspective, even fiber reinforced polymers or composite's parts. The chapter 2 presents both the development of an internally designed formulation containing 30wt% of recycled carbon fibers and the detailed characterization of commercially available reinforced filaments. In this chapter, the characterization of specimens printed using PEI filaments on an industrial FDM printer. This part of the study is aimed to develop a better understanding of the mechanical behavior of FDM printed part and to rationalize the results DoE (design of experiments) was used to quantify the effect of the relevant parameters. The choice to characterize PEI printed parts was due to the inherent strong dependency of interlaminar bonding on such type of polymer when 3D printed which, as results, display a highly anisotropic behavior.

Chapter 3 deals with the development and use of AM materials and technology as tooling for composites manufacturing. Tooling is a key component for the shaping of composite materials. Traditionally tooling can be hand made, for low cost components, or machined by CNC. However, in some cases these solutions are not effective. This is particularly true for very complex hollow shapes where tooling removal after curing is not easy. However, these types of shapes are those where the use of composites is of pivotal importance. AM is also well accepted as a technology allowing freeform design for its suitability to print complex 3D shapes. Therefore, using AM for composite tooling is a logical choice. However, composite's tooling requires to ensure certain specification such as: surface quality, dimensional tolerance, heat resistance, heat distortion factors etc. In the AMA study a special case of tooling was studied: the removable mandrel. This tooling is special because it must allow for reliable laying up of sheets of dry or prepregged fabrics while still allowing to easy demold parts from the tools. The latter requirement can be satisfied

by properly designing the AM material in order to be either simple to break away or soluble to be washed away. In chapter 3 the solutions tested in the course of the thesis will be discussed. The materials analyzed ranged from commercial dissolvable FDM materials to breakaway LCD materials developed here. In addition to that, to enlarge the spectrum of solution available for the tooling design engineer a high temperature resin for LCD have been formulated in the present thesis. The latter resin aims to be used as tooling material for permanent high temperature curing tooling which might be of interest in the aerospace field where curing cycles up to 175 °C are used. All the solutions investigated in chapter 3 were analyzed by cost and production time analysis comparing them to standard approaches or materials.

Finally, chapter 4 is focused on the characterization of a novel class of metal filled filaments purchased from BASF. These materials attracted a lot of interest only in the very last years thanks to the launch on the market of Desktop Metal company in 2015. The concept behind the use of metal filled materials in FDM is to print the so called green part using the standard approach used for plastic FDM and then, by following a debinding and sintering cycle, transforming the part into a fully dense metal one. This approach is foreseen to allow to use all the potential of FDM printing while obtaining very resistant metal parts. In chapter 4 two materials were deeply investigated: Ultrafuse 316L and Ultrafuse 17-4PH. The filaments were thoroughly characterized to understand their composition and then printed using two commercial printers available in the laboratory. The printed parts were characterized and tested to understand the mechanical performance of the parts after the full debinding/sintering cycle. All the study was carried out rationalizing the data using DoE to plan and analyze the experiment. This approach allowed to identify the best parameters driving the mechanical performance allowing to find optimized printing conditions for the green part manufacturing. The metal filled filaments were also used to print small moulds and various shapes in view of their use for the manufacturing of self-standing tooling or inserts to be implemented in complex composite constructions. Cost and time analysis was run comparing the use of these materials to other more traditional techniques like metal AM or CNC.

The PhD thesis finally reports a conclusion paragraph where all the findings are discussed and some future perspective of the future work that could lead to further exploitation and development of the work presented are discussed.

Chapter 1

State of the Art on AM

1.1 FDM/FFF standards and materials

AM is a layer-by-layer construction technique that allows for the creation of complex objects without the need of molds. AM holds promise for producing components ranging from prototypes to working constructions. Aerospace, automotive, semiconductor, and biomedical industries are just a few of the businesses that use AM. One of the most prevalent AM processes is fused filament fabrication (FFF), also known as fused deposition modeling (FDM). The melting of a thermoplastic filament that is deposited on a platform to build each layer on top of the other is the foundation of FDM. Many parameters control the FDM process, ranging from material type to machine settings including nozzle diameter and temperature, printing speed, feed rate, bed temperature, raster angle, and width [44]. Several extensive investigations on the impact of printing settings on the mechanical properties of 3D-printed objects have been published in the literature. Polymer chain alignment occurs during filament deposition, according to Es-Said et al. [24]. As a result, different raster orientations have varied tensile, flexural, and impact resistance. Ahn et al. [4] obtained similar results. The impact of raster orientation, air gap, bead width, color, and model temperature factors on tensile strength was investigated in their research. The air gap and raster orientation have an impact on tensile strength, while the bead width, model temperature, and color do not. Lee et al. [56] found that layer thickness, raster angle, and air gap all affect the elastic performance of 3D-printed ABS (Acrylonitrile Butadiene Styrene) parts in another investigation. For testing polymeric materials manufactured by injection or compression molding, the ASTM D638 tensile test and the ASTM D790 or ISO 178 flexural test are both frequently used standards. As a result, practitioners may be interested in expanding their application to include the measurement of mechanical properties of FDM produced objects. Unfortunately, these requirements do not take into consideration the occurrence of voids, which are

inevitable in FDM. Furthermore, they were not designed precisely to characterize the interlayer bonding that affects the mesostructures of FDM printed objects. The tensile characteristics of FDM printed items are greatly affected by voids, according to Tronvoll et al. [88]. The chamber temperature and fluctuations in the convection coefficient, according to Sun et al. [59], have a significant impact on the cooling temperature profiles, as well as the mesostructure and overall quality of filament bonding. They did not, however, quantify interlayer strength because the results of the flexural testing were highly variable. Only a few publications in the AM literature have looked into the bonding quality of layers and rasters manufactured with FDM.

The short-beam strength (SBS) test has recently been used to assess interlaminar bonding. For fiber reinforced composites, this test is often employed [11,12,67,102]. Porosity and interlaminar shear strength (ILSS) were shown to be related in a study of the interlaminar bonding performance of continuous fiber reinforced thermoplastics produced by FDM [11]. Working with similar materials, O'Connor [67] verified these findings. SBS testing, compared to tensile or flexural tests, showed greater sensitivity in measuring interlaminar bonding effects for various materials [12].

All of these articles, on the other hand, lacked statistical analysis of the measured data. Some studies used the design of experiment (DoE) toolbox of statistical approaches to try to rationalize the results of mechanical testing [4,48,64,65,93,96]. Because of the various bonding qualities between the layers, Vicente et al. [96] shown that the interlayer cooling time can influence the ultimate tensile strength (UTS). The effect was stronger in the Type V-D638 sample than in the Type I-D638 sample.

However, by assessing interlayer bonding, the effect of sample type on interlayer bonding was not systematically examined. Tensile testing according to ASTM D638 has also been critiqued for dog bone specimens due to the significant stress concentrations induced by the longitudinal road termination [4]. To overcome this issue, ASTM D3039 was proposed.

Given the enormous number of desktop printers on the market, the FFF (Fused Filament Fabrication) process is undoubtedly the most popular of the AM techniques. However, maintaining sufficient internal stress relaxation and effective interlayer bonding inside printed parts remains a major challenge [81,98]. There are limited studies in the literature on AM applications that look into the quality of the interlayer and raster bond of the part produced by FFF [67,86]. FFF filaments containing carbon fibers (CF) are particularly appealing for applications in automotive, robotics, drones, prosthetics, and orthotics [47].

Polyamide 6 is one of the most commonly used matrices, although there are few studies that compare the mechanical qualities and printing parameters of these composite filaments [70].

1.2 Composite Tooling

The use of FDM for composite tooling is one subject that is acquiring significant industrial importance. Several technical articles [5,20] explored the emerging trend of using AM techniques as a viable solution for tooling production in industry. The foundations of this application of FDM were explained in fewer works. Li et al. [57] detailed the analysis of material properties needed and modeled the behavior of Ultem 9085 as tooling materials for vacuum assisted resin transfer molding.

Türk et al [91] presented three case studies in which the application of additive manufacturing techniques can optimize composites part production. In several of these applications, the AM parts were used as tooling for laying down carbon fabric. After cure, the AM pieces were used as permanent tooling in the parts. In other circumstances, soluble polymer compounds and FDM allowed for the production of sacrificial tooling to embed electronics in composite structures, as discussed by Roy and Dickens [75]. The use of soluble FDM materials for sacrificial tooling [90] is of interest for industrial use as a means of producing complex hollow composite parts.

However, the impact of the removal procedure on composite characteristics, as well as the true technoeconomic advantage of this strategy over standard approaches, have not been thoroughly investigated in the literature. As an alternative to FDM, other AM processes could be utilized. Liquid crystal display (LCD), for example, offer various benefits in terms of surface quality, resolution, and temperature tolerance. [31] The latter benefit relates to the ability to print parts with high temperature resistance and toughness utilizing thermoset mixes [14–16, 18, 66, 85].

The AMA project’s research focuses on the use of LCD technology to print removable composite tooling and compares it to traditional FDM tools.

1.3 LCD Printing

The utilization of LCD displays as imaging systems is the basis for LCD (Liquid crystal display) printing. The main feature of LCD printing is that light passes direct through flat LCD screens onto uncured resin. Because light does not extend as much in LCD printing as it does in DLP printing, pixel distortion is less of a concern. Furthermore, unlike SLA, an entire layer can be exposed at the same time, eliminating the requirement to scan the photopolymer point-by-point. This resulted in a quicker 3D printing process. The illumination in many LCD printers comes from a series of UV or LED lamps.

Other photocuring 3D printing technologies work on different principles: digital light processing (DLP) uses a projector to project an image of the cross section of the object to be printed; stereolithography apparatus (SLA) scans and cures the layer of photocuring resins point by point; and multi jet printing (MJP) prints the models

by spraying liquid photosensitive resins from several nozzles and then curing the layer by using an UV lamp [72]. Carbon3D announced the CLIP (Continuous Liquid Interface Production) technique in 2015, which is built on an oxygen permeable membrane that allows for the sequential printing of each layer, speeding up part production. DLS is another term for CLIP technology (Digital Light Synthesis).

The use of oxygen permeation to impede radical polymerization and allow quick continuous printing [89] is one of the most important aspects. Carbon3D technology is based on the availability of several resin chemistries ranging from acrylates to epoxies, cyanates, and polyurethanes, as well as the utilization of oxygen permeation membranes. Some of Carbon3D's best-performing resins are based on a dual-curing technique [42], in which photocuring is followed by thermal curing.

Obst et al. [66] looked at how varying exposure times affected the dual curing response of a polyurethane-based resin utilized in DLS. A mixture of acrylate and polyurethane resin was used in their research. Mechanical properties including tensile strength and elongation at break have been proven to be highly influenced by UV crosslinking. Redmann et al. [73] focused on a carbon3D printer-processable epoxy-based solution. For this technology, the authors tackled the issue of thermal curing optimization. The main goal was to reduce the heat curing time while avoiding a negative impact on the final mechanical qualities.

The initial curing time of 750 minutes was reduced to 200 minutes while the glass temperature transition was improved from 146 to 154 ° C. Shape memory polymers, optical materials, photolithography, protective coatings, structured surface topologies, and holographic materials have all been researched using dual curing for acrylate-based systems [51]. A dual-curing method is characterized by the simultaneous or sequential occurrence of two curing reactions. 3D printing of carbon fiber reinforced composites was possible using epoxies mixed with a photocurable acrylic resin that was cured using a combination of photocuring and thermal curing [41].

For DLP printing, Lantean et al. [55] developed a similar technique based on epoxy/acrylate mixtures. Epoxy was employed in this work, but no thermally activated curing agent was added. For those blends, the maximum Tg was limited to 108.6 C. The majority of photocurable resins cure in the UV area at wavelengths between 325 and 420 nm, while daylight resins cure at 460 nm. The use of longer wave length light demonstrated to enable for a deeper penetration depth into the photopolymer material and hence a more uniform and accurate 3D printing process, according to Photocentric [45, 103].

The use of visible light in conjunction with LCD screens for 3D printing enables a faster, more efficient, and cost-effective production process. This is an important application point. Additive manufacturing is increasingly being used in a variety of industries, including microfluidics [9, 74, 97], composite tooling [57, 84], and injection molding [49].

If complex toughened epoxy blends are utilized, mixing epoxy blends with photocurable resins can open the field to novel formulations [16,18] because this can be a suitable way to get the impact resistance of the printed specimens. All of these applications could benefit from a precise cavity control system [10,78].

1.4 Metal-filled filament for FFF

Additive manufacturing (AM) has grown in popularity not only as a prototype tool, but also as a tool for producing functioning parts, thanks to recent advancements. Metal additive manufacturing is frequently used to make aerospace parts [27], medical prosthetics [58], and automotive parts [43], among other things. Direct metal laser sintering (DMLS), selective laser melting (SLM), laserengineered net shaping (LENS), electron beam melting (EBM), binder jetting (BJ), and other metal AM methods are available. To 3D print items, most of these technologies use metal powders as feedstocks and high-energy sources to melt or sinter the metal powder [21].

To operate securely with metal powders, these approaches necessitate large investments in machine purchases and complicated facilities. Metal AM was limited to select industries where the return on investment justified its use because to the high investment costs of existing techniques. Several manufacturers have recently created lower-cost hybrid metal/polymer feedstocks produced using traditional polymeric AM processes in a bid to democratize metal additive manufacturing. In these circumstances, green printed components were subjected to debinding and sintering cycles in order to remove the polymeric binder and get fully dense metal objects.

Fused filament fabrication and vat photopolymerization are the two AM manufacturing techniques that have been employed so far. To create the green component in the first scenario, metal/polymer filaments or rods are printed with FFF-like printers. This is how Desktop Metal Inc, Markforged Inc, and Nanoe systems work. Pollen AM and AIM3D GmbH, for example, have developed machines that process pellets directly, similar to those used in Metal Injection Molding (MIM). Metal AM is being developed by Admatec, Incus, and Photocentric Ltd. using photopolymerizable polymers that are densely filled with metal particles.

Fused Deposition of Metals (FDMet), a seminal work that established the use of FFF with metal filled filaments, was originally presented in the 1990s [3,60,100]. However, this method has only recently sparked renewed interest, with several publications examining the usage of various metals. Two types of stainless steels were studied: 316L and 174 PH. Kurose et al. [52] used their own filament to test the impacts of different building orientations for 316L printed items. All of the pieces were printed with a rectilinear infill pattern and a 100% infill density, with the layer thicknesses changing.

With a layer thickness of 0.1 mm, the green printed component had the highest

density of 92.9 percent, whereas the sintered parts displayed anisotropic behavior, with shrinkage degrees ranging from 15 to 17 percent and the highest shrinkage along the layer direction. Other investigations revealed shrinkage values ranging from 15 to 23 percent [37]. The lowest values for Ultimate Tensile Strength (i.e., 100 MPa) were displayed by specimens printed upright, while the greatest values (i.e., 453 MPa) were displayed by samples printed flatwise and on the edge. The considerable disparity was explained by the cavities in the upright specimens being perpendicular to the tensile direction.

There was no information on the tensile modulus. Gong et al. [37] used the Ultrafuse 316L filament to print their specimens, which had a residual porosity of roughly 1.5 percent, compared to the totally dense structure obtained by SLM. The sintered specimens have the same equiaxed grains and austenitic microstructure as the annealed specimens. The yield strength was 167 MPa, with a UTS of 465 MPa and a tensile modulus of 152 GPa. All of these values were lower than those obtained from SLM samples and those published with AISI 316 L.

When compared to typical annealed AISI 316 L, the low mechanical qualities were explained as the result of porosity, which also generated a reduced ductility (i.e., 31%). (i.e., 60 percent). Thompson et al. [82] concentrated on determining the flexural behavior of 316L filaments made on their own. To get high green body density samples, they employed overextrusion. The porosity after sintering ranged from 1.9 to 1.4 percent, depending on the sintering temperature. In this research, EDX (Energy Dispersive XRay Spectroscopy) investigation found that the grain boundary phase is Cr₂₃C₆, which is assumed to have no effect on corrosion but does result in sintered part embrittlement due to carbide presence.

When compared to a rolled sheet made of 316L, the mechanical characteristics were reduced by around 20%. The presence of porosity and the large grain size after sintering were attributed for these findings. There have been few research on FDM printing using 174 PH loaded filaments. GonzalesGutierrez et al. [38] investigated 3D printing conditions for filaments made in-house in 2018. The sintered pieces that resulted were also described in the studies that followed. [39] The average Young's modulus was 196 GPa, the average maximum stress was 696 MPa, and the strain at break was 4%.

After sintering, the printed specimens had an average porosity of 4.3 percent, however there was a lot of variance in strain at break between batches. The mechanical qualities of green parts were adjusted by changing the 3D printing parameters in a recent research [35]. Galati and Minetola [29] recently published a study on the density, roughness, and dimensional accuracy of sintered components printed with 174 PH filaments utilizing Markforged's unique ADAM (Atomic Diffusion Additive Manufacturing) technology.

Fiber reinforced filaments

2.1 CF-reinforced filaments production

Fused Filament Fabrication (FFF) printing is easy to manage but it is known that its parts have lower properties than the equivalent parts obtained by conventional methods, such as injection molding, since they are characterized by voids and weak interlaminar bonds. One way to overcome this aspect is to introduce reinforcing fillers into the polymer matrix of the filament, in the form of fibers or nanomaterials. FFF filaments loaded with carbon fibers (CFs) are particularly interesting for their use in the automotive, robots, drones, prosthetics and orthotics fields. One of the most popular polymers in FFF printing is Polylactic Acid (PLA), as it is relatively easy to print and safe to use. Some authors [7, 47, 62] obtained filler percentages up to 20wt% of carbon nano powder (NC) having dimensions of about 500nm, with a modest increase in the observed mechanical properties, as well as in the electrical ones. The present work aims to produce PLA filaments with a high charge of milled carbon fibers (MCF, average length of 1000nm), which can be used as feedstock in FFF printing. The mechanical specimens were printed up to 30wt% of MCF and showed a significant improvement in mechanical properties

Filament Extrusion

The production of filaments with percentages up to 30wt% of CFs took place considering polylactide acid resin (PLA) as thermoplastic matrix (Table 2.1).

ID	PLA content [wt%]	CFs content [wt%]
PLA	100	0
PLA+CF10	90	10
PLA+CF20	80	20
PLA+CF30	70	30

Table 2.1: ID of studied formulations.

The choice of this polymer, in addition to environmental sustainability reasons, consists in the fact that PLA is the most easily printable polymer currently on the market and that it does not present problems related to the safety and toxicity of the volatile compounds generated by the fusion. In the present work, filaments are made of pure PLA, grade 4032D by Natureworks Lcc (Nebraska, USA), filled with recycled carbon fibers from pyrolysis, in particular Milled Carbon Fibers (MCF) provided by Easycomposites (England, UK). The production of the filaments took place using the Compounding KETSE 20/40 twin-screw extruder (Figure 2.1) produced by Brabender GmbH & Co. Initially, the PLA in the form of pellets was dried in a special oven at a temperature of 50-60 °C to avoid the formation of air bubbles in the filament and clogging of the nozzle during extrusion.



Figure 2.1: Extrusion line for filament production. [QR-code link]

Inside the extrusion chamber there are 4 screws at a temperature that depends on the type of polymer being used; in this case, being PLA, the temperature is between 200-220 °C. The maintenance of this temperature is managed through special software that shows the extruder diagram with relative temperatures for each screw,

in the rings and in the pressure switch. The use of rings, just outside the chamber, allows you to work with pressure as an input parameter in order to obtain a more or less uniform diameter.



Figure 2.2: Particular of PLA CF-reinforced filament extrusion.

The pressure in the extruder can vary from a minimum of 4 bar up to 30 bar. Before proceeding with the collection of the actual filament, it is necessary to check that the diameter of the filament is constant in a range of about 0.4mm. For our purpose the final diameter of the filament needs to be equal to 2.85 ± 0.2 mm because one of the open FFF machine present in the laboratory has requires this filament as feedstock. In order to do this, the die was designed with a diameter of 6 mm (Figure 2.2). The mixture of the two components is regulated with the speed: knowing the speed of injection of each component into the mixer, the composite material is obtained. When you begin to extrude the filament, it passes through a series of rollers: the first two rollers present immediately after the nozzle are used only for accompaniment, while the next four are used to define the diameter of the extruded filament. A manual control panel placed above the rollers allows you to adjust the speed of the rollers so that the filament can be collected in a spool for using in a 3D printer.

The production of the various filling degrees was monitored by measuring the diameters at regular intervals of 5 minutes by using a digital calliper, in order to observe any anomalies in the process and intervene. The collected data were analyzed using Minitab statistical software for the elaboration of Frequency and Control charts (Figure 2.3). Using a non-contact laser gauge with feedback and process history storage will improve the production of diameters in an even smaller range than the aforementioned 0.4mm.

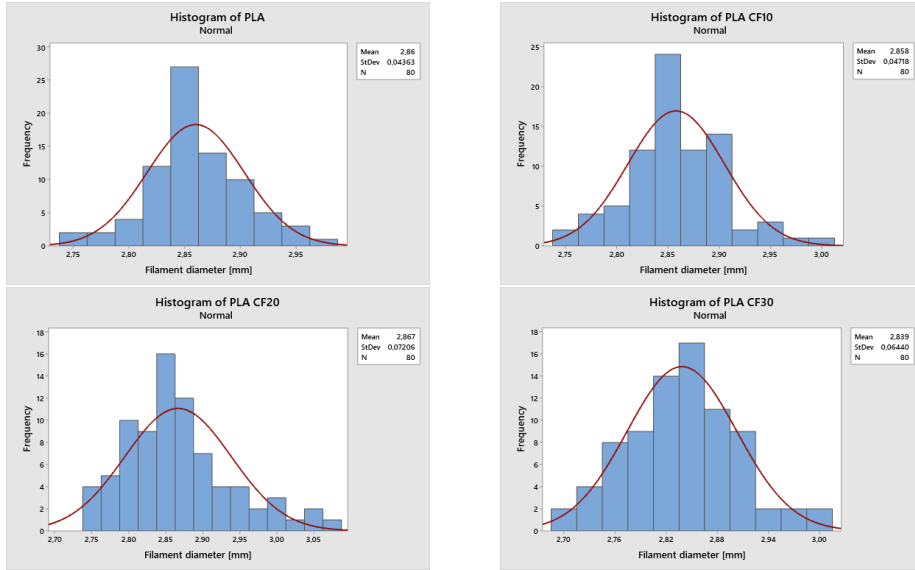


Figure 2.3: Frequency plots of filaments diameter.

Fused Filament Fabrication (FFF) Printing and Testing

After a first phase of printing optimization, the samples for mechanical testing (ASTM D638) were obtained using the Ultimaker S5 printer (Figure 2.4).

The picture of the tests conducted to obtain excellent prints and the printing parameters are visible in the AppendixA, Figures A.2 and A.1.

In order to understand the mechanical behaviour of the samples produced, a general factorial design according to design of experiments (DoE) was considered. In particular, the parameters visible in Figure2.2 have been taken into consideration, with 3 replications, for a total of 36 runs. The observed responses are the following: Young’s Modulus, Tensile Strength and Elongation at Break.

Factors	Levels	Type	Unit
Material	PLA; PLA+CF10; PLA+CF20; PLA+CF30	Categorical	-
Raster Angle	0; 45/135; 0/90	Categorical	[°]

Table 2.2: Factors and levels studied in DoE plan.

All the samples were tensile tested in accordance to ASTM D638, by using an Instron 5985 universal testing machine (Instron, Milan, Italy) equipped with a load cell of 10 kN, in strai control mode at a speed of 2mm/min. Average stress-strain curves are visible in Figure 2.5, while the mechanical properties values are summarized in Table 2.3.

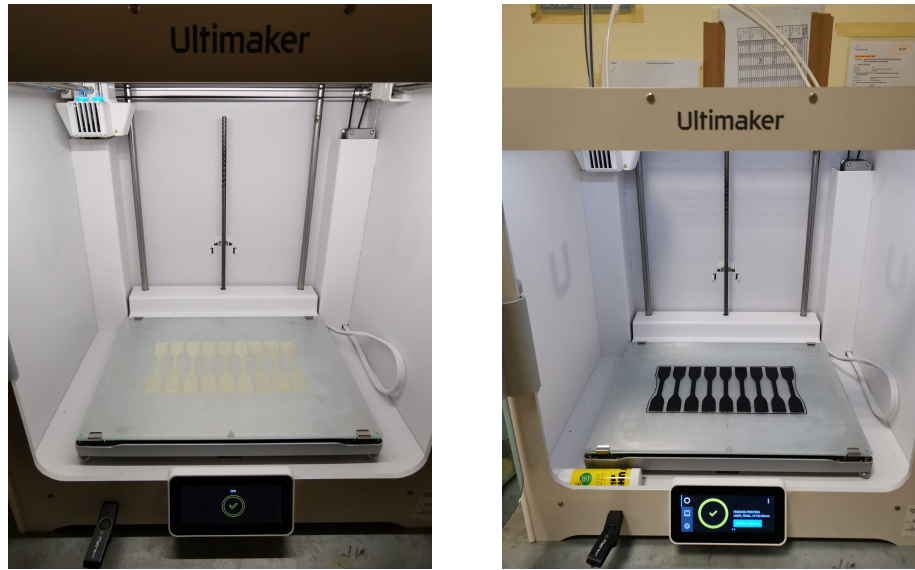


Figure 2.4: 3D printed samples by PLA (left) and PLA CF-reinforced (right) extruded filaments.

ID	RA [°]	E [GPa]	UTS [MPa]	Eb [%]
PLA	0	5.22 (0.02)	90.45 (2.96)	2.31 (0.10)
	45/135	5.21 (0.02)	87.37 (1.22)	2.22 (0.05)
	0/90	5.25 (0.02)	86.36 (0.46)	2.11 (0.07)
PLA+CF10	0	5.39 (0.05)	58.90 (1.34)	1.64 (0.12)
	45/135	4.78 (0.17)	54.51 (2.03)	1.58 (0.02)
	0/90	4.58 (0.08)	49.02 (1.37)	1.55 (0.06)
PLA+CF20	0	7.05 (0.08)	53.16 (1.41)	1.07 (0.09)
	45/135	5.80 (0.09)	48.56 (1.08)	1.17 (0.02)
	0/90	5.62 (0.21)	44.94 (1.59)	1.11 (0.16)
PLA+CF30	0	8.56 (0.11)	64.59 (0.30)	1.00 (0.14)
	45/135	7.32 (0.20)	60.59 (0.35)	1.24 (0.12)
	0/90	7.19 (0.13)	57.85 (0.04)	1.32 (0.07)

Table 2.3: Average tensile properties. Standard deviation is depicted in brackets. RA: raster angles, E: tensile modulus, UTS: ultimate tensile strength, Eb: elongation at break.

ANOVA analysis for each response was performed and the results are reported in Appendix A (Figures A.3, A.4 and A.5), while the effects plots are shown in Figure 2.6.

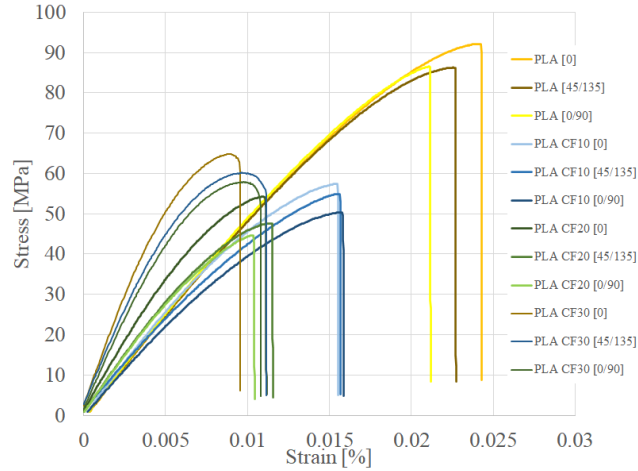


Figure 2.5: Average stress-strain curves.

The tensile modulus response is influenced by the percentage by weight of CFs, in fact the observed values increase of 64%, from 5.22 to 8.56 GPa for samples printed with 0° raster angle. The same trend is recorded for all the other raster angles. In particular, there is a greater influence of this printing parameter towards higher percentages of CFs, in fact for the base PLA no significant difference was noted between the various raster angles. The statistical model (R-squared of 0.99) showed the best printing configuration the one at 0° of raster angle. As for the tensile strength response, however, the model (R-squared of 0.99) showed the influence of the CFs content and raster angle. In particular, an average decrease in the tensile strength values of about 40% is noted. The effect of CF-reinforcement is visible on the samples at 30wt% CFs. As for the raster angle (Figure 2.6c), this factor appears to be influencing the tensile strength response. A similar trend was defined by the model (R-squared of 0.97) regarding the elongation at break response, with substantial decreases in the observed values, from 2.31 to 1%.

The properties of the samples printed with 0° of raster angle were shown to be better for the load condition imposed in the uniaxial tensile testing. In fact, as it is possible to see in an SEM image (Figure 2.7) of a sample printed at 0° and fractured in the center line, the fibers are oriented along the printing direction and are all loaded in the preferential direction to obtain the best performance.

In general, it is not possible to observe an improvement in all mechanical characteristics. However, the values obtained proved to be satisfactory both in terms of mechanical properties and printability of the filaments obtained, without the need to add additives and plasticizers. In Table 2.4 it is possible to observe a comparison of the filaments obtained with those available commercially. In Figure 2.8 some components whose printability is excellent and having a good surface finish are shown.

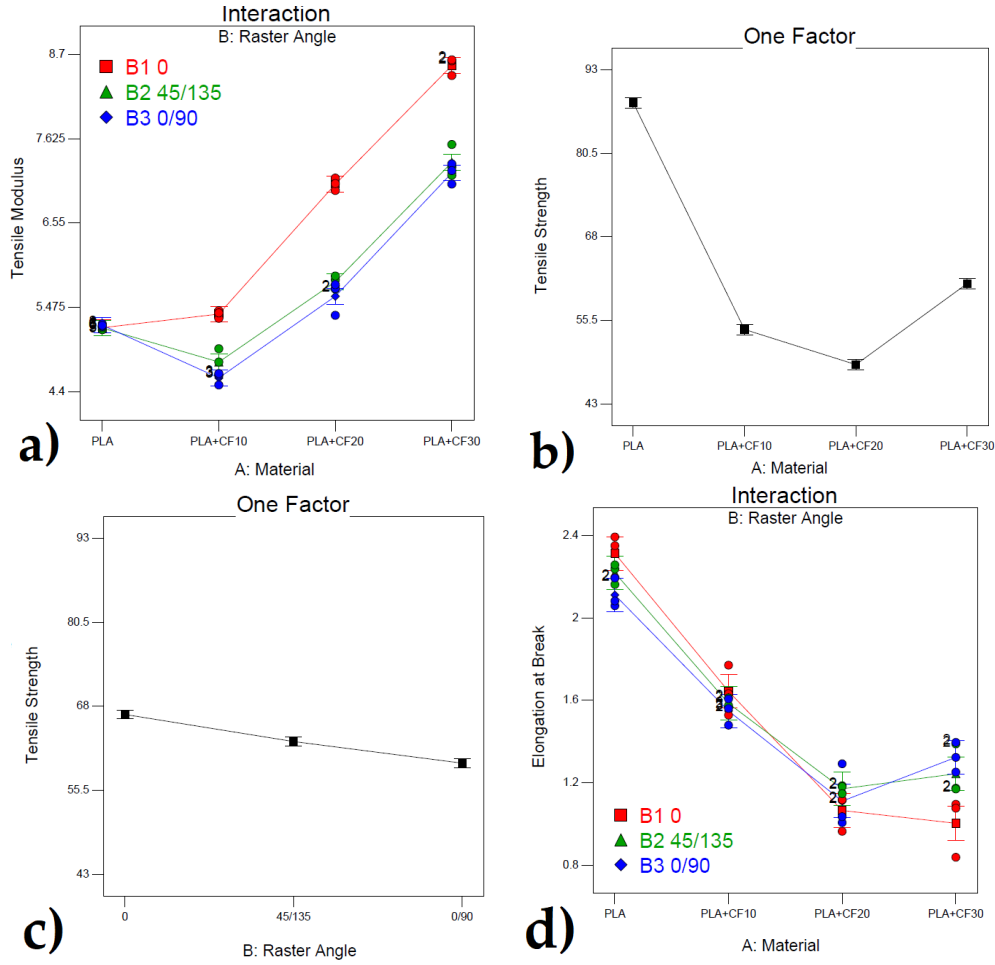


Figure 2.6: Effects plots for the response: a) tensile modulus, b-c) tensile strength, d) elongation at break.

Filaments	E [GPa]	UTS [MPa]	Eb [%]	Manufacturer
PLA	5.22	90.45	2.19	This study
PLA	-	63.00	4.00	Verbatim [95]
PLA	2.35	45.60	5.20	Ultimaker [92]
PLA	2.19	25.40	2.49	FiberForce [26]
PLA+CF10	5.39	58.90	1.64	This study
PLA+CF15	6.56	96.00	-	Proto-Pasta [71]
PLA+CF15	4.23	51.00	2.08	3DXTECH [1]
PLA+CF20	7.05	53.16	1.07	This study
PLA+CF20	4.95	48.00	2.00	3DXTECH [2]
PLA+CF20	4.80	47.90	2.00	SD3D [79]
PLA+CF30	8.56	64.59	1.00	This study

Table 2.4: Comparison of PLA filaments.

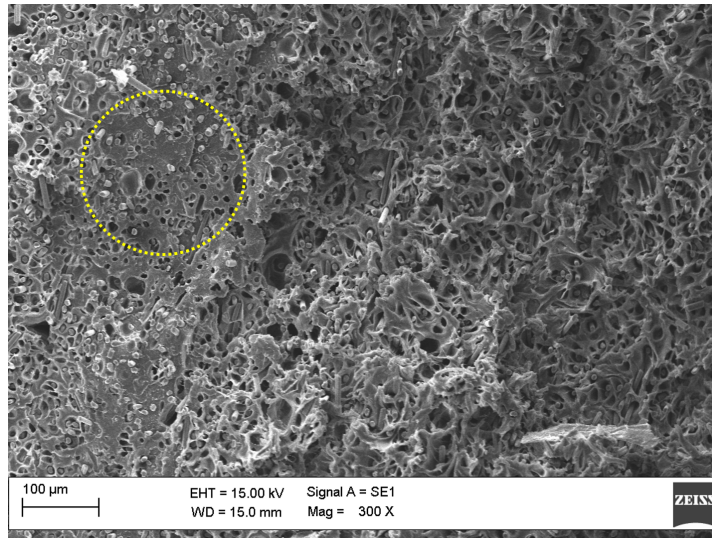


Figure 2.7: SEM image of a cross-section of a 3D printed PLA+CF30 sample with raster angle 0° .



Figure 2.8: 3D printing components by PLA+CF30.

Thermal diffusivity measurements

By exploiting additive manufacturing as an aid to traditional composite processing that we will see later, the benefit of adding carbon fillers does not only concern the improvement of mechanical properties. In fact, the presence of carbon fibers translates into an improvement in performance at temperatures.

Thermal diffusivity of 3d printed specimens, square in size (side of 12.7 mm and thickness of 2 mm), was measured by adopting LFA 467 HT HyperFlash machine (Netzsch, Germany), Figure 2.9. The area of the analyzed sample was equal to 70%, the measurement was repeated 3 times, and the Cowen model was used for fitting



Figure 2.9: Laser Flash test setup.

the signal. The thermal diffusivity was evaluated by adopting the following formula 2.1:

$$\text{Thermal diffusivity} = \frac{1.38d^2}{t_{1/2}} \quad (2.1)$$

where d is the sample's thickness and $t_{1/2}$ is the time required for the signal to reach 50% of its maximum value [28].

The measurements were carried out in the range of interest for use compatible with the manufacturing of composites. Therefore, a heating cycle was set with hold temperatures equal to 70 and 90 ° C, typical curing values for prepreg that will be discussed in the Chapter 3.

ID Samples	Thermal diffusivity (mm ² /sec)	
	@ 70 °C	@ 90 °C
PLA+CF10	0.106±0.001	0.102±0.001
PLA+CF20	0.123±0.001	0.122±0.001
PLA+CF30	0.129±0.001	0.128±0.001

Table 2.5: Thermal diffusivity of 3D printed samples.

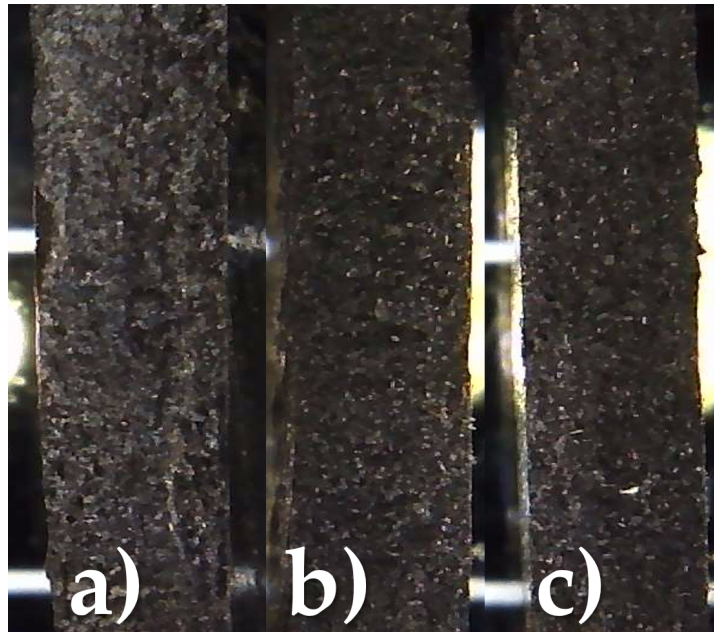


Figure 2.10: Optical image of laser flash 3D printed samples: a) PLA+CF10, b) PLA+CF20, c) PLA+CF30.

The Table 2.5 shows the measured Thermal diffusivity values. The increase in the thermal diffusivity value is associated with the increase of CFs in the 3D printed composite. As Figure 2.10 shows, no macroscopic differences are evidenced in the crosssection of the 3D printed and analyzed samples. This result can be exploited for AM-enabled manufacturing processes where temperatures come into play, such as Composite Tooling which will be discussed in detail below.

2.2 Mechanical Characterization

The mechanical characterisation of the materials under investigation necessitates the execution of a proper test. Unfortunately, there is currently no acknowledged worldwide standard specially designed for assessing the mechanical qualities of FDM printed items. As a result, we looked at and compared the results of three well-known mechanical tests that have been used in various sectors of application. By assessing numerous experimental plans, the goal was to establish a good test for characterizing the two 3D-printed ULTEMTM material kinds.

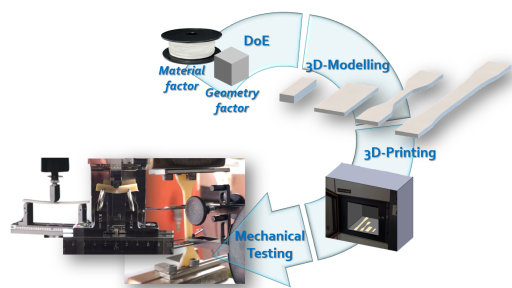


Figure 2.11: Graphical abstract of the cited work.

Proposed standards for testing FDM/FFF printed samples will be shown in this section. Finally, 3D printed components will be evaluated for use as end-use parts in robotics, tooling, and automotive applications.

2.2.1 Mechanical testing for FDM/FFF materials

Preliminary study

To determine the differences in viscoelastic and thermocalorimetric behavior between tan and black ULTEM 9085 materials, a preliminary investigation was conducted. ULTEM 9085 is a PEI modified polymer with a copolymer for enhanced flow, according to previous testing [19]. Figure 2.12 shows the $\tan\delta$ versus temperature plot for both polymers. The tan sample showed a large peak at 185 °C and a shoulder at 140 °C. The peak and shoulder of the black sample changed to 195 °C and 148 °C, respectively.

The glass transition was detected at roughly 180 °C in both tan and black materials, according to DSC measurements (Figure 2.13). The tan sample had two separate thermal transitions, but the black resin had only one. In the past, similar results for PEI blends were obtained [6]. Despite the fact that the behavior is also different for the two grades for this study, the DSC test appears unable to properly resolve the thermal transitions as found in the DMA test.

Despite their similar compositions, the two materials behave differently according to the thermal assessments shown here. The finish and mechanical behavior of PLA-based filaments have been found to be affected by pigmentation [17,80,94,99]. Similar data on PEI-based filaments, on the other hand, has never been published. As a result, the research was carried on by analyzing the mechanical behavior of the

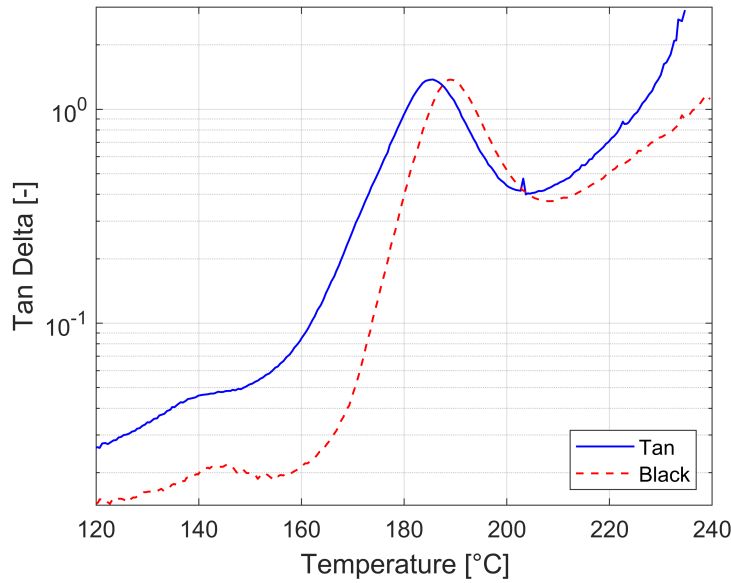


Figure 2.12: DMA analysis on Ultem9085.

printed pieces made of the two materials.

Testing

An ANOVA analysis was performed using the Design-Expert software after establishing the experimental plan and collecting the response observations (Table A.2) of the tensile test according to the ASTM D638 standard (UTS and Young's modulus). The testing sequence was randomized, as shown in Table A.2 in the Supplementary Material. Figure 2.14 shows the average tensile stress of the five tested samples vs displacement curves. All of the specimens that were evaluated showed brittle failure with no yielding. For the two materials, the UTS varied between 48.99 MPa and 61.98 MPa.

Young's modulus was found to be between 2.05 and 2.34 GPa. The tensile properties observed were similar to those published in earlier ULTEM 9085 studies [8, 19, 34, 101]. Tensile strength values for flat samples ranged from 46.83 MPa to 71.03 MPa for on-edge samples, according to Zaldivar et al. [101]. The young's modulus ranged from 1.77 to 2.48 GPa. The raster orientation in this investigation ranged from 90° to 0°. Byberg et al. [8] found tensile strength values ranging from 31.30 MPa to 70.60 MPa. FDM samples have inferior mechanical characteristics, with UTS reductions ranging from 20% to 40% and a strain of roughly 2% [22].

When compared to injection molded specimens, these results are dependent on the existence of voids and the temperature history of the printed samples.

Table 2.6 shows the Analysis of Variance (ANOVA) table for Young's modulus response. The residuals from the analysis were checked for model adequacy and found

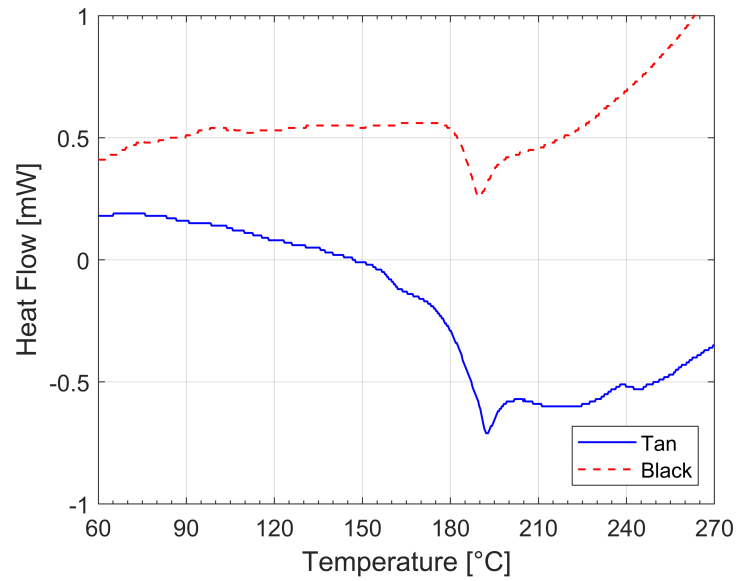


Figure 2.13: DSC analysis on Ultem9085.

to be normal. The material type (factor A) has a substantial interaction AB (p-value 0.001) with the geometry (factor B) on Young's modulus (Figure 2.16, Table 2.6) and is an influencing factor (p-value 0.001) on Young's modulus (Table [tab:ANOVA tab3]) (Figure 2.17). With a high R-squared value of 0.8368, the model appears to have good robustness in defining the observed response.

When the UTS response is regarded the response variable, however, the ANOVA analysis reveals that the material and geometry factors have no bearing on it (Table 2.7). As evidenced by the very low R-squared value of 0.0764, the tensile test is unable to characterize the ultimate tensile strength (UTS) for the two materials. We explain this finding by assuming that the tensile test for flatwise printed specimens is not as sensitive to interlayer bonding as it is for upright orientation cases where interlayers are directly loaded. In fact, the longitudinally oriented rasters can withstand applied loads for flatwise samples.

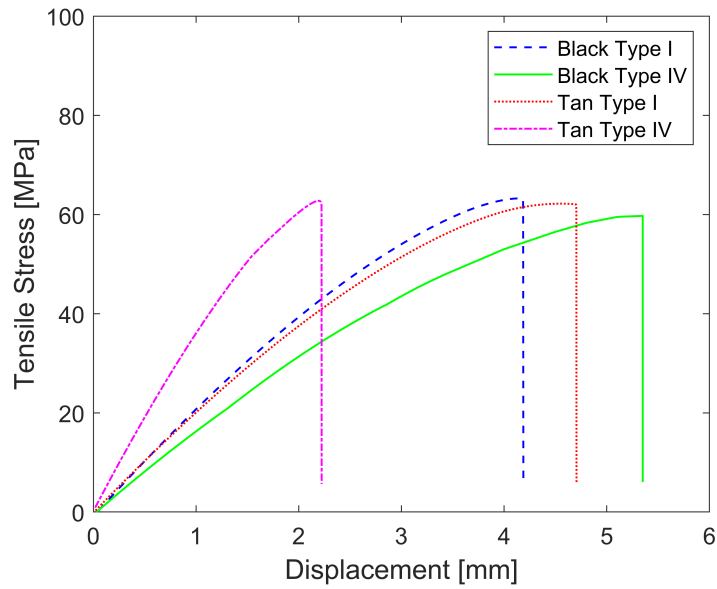


Figure 2.14: Average stress-strain curve for tensile test.

Source	Sum of Squares	df	Mean Square	F Value	<i>p</i> -Value
Model	0.1109	3	0.0370	25.6417	<0.0001
A-Material	0.0575	1	0.0575	39.8659	<0.0001
B-Geometry	0.0056	1	0.0056	3.8861	0.0674
AB	0.0575	1	0.0575	39.8659	<0.0001
Pure Error	0.0216	15	0.0014		
Cor. Total	0.1325	18			
Std. Dev.	0.038	R-squared	0.8368		
Mean	2.19	Adj. R-squared	0.8042		
C.V. %	1.73	Pred. R-squared	0.7442		

Table 2.6: ANOVA table for tensile test (response is Young's modulus).

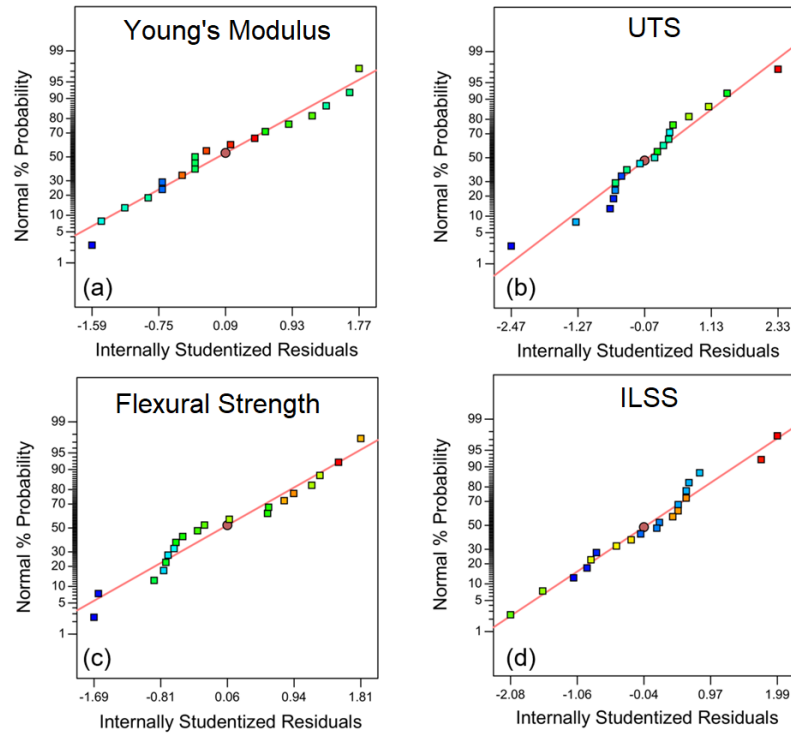


Figure 2.15: Normal probability plot for: (a) Young's modulus; (b) ultimate tensile strength; (c) flexural strength; and (d) interlaminar shear strength.

Source	Sum of Squares	df	Mean Square	F Value	<i>p</i> -Value
Model	12.4925	3	4.1642	0.4413	0.7266
A–Material	1.7387	1	1.7387	0.1843	0.6735
B–Geometry	2.0563	1	2.0563	0.2179	0.6469
AB	8.6975	1	8.6975	0.9218	0.3513
Pure Error	150.9726	16	9.4358		
Cor. Total	163.4652	19			
Std. Dev.	3.0718	R-squared	0.0764		
Mean	59.1469	Adj. R-squared	–0.0967		
C.V. %	5.1935	Pred. R-squared	–0.4430		

Table 2.7: ANOVA table for tensile test (response: UTS).

The structure of ULTEM 9085 showed a clear contrast between the deposited filaments that are not totally bound and melted together (Figure 2.18). To properly define the mechanical behavior of the material, testing procedures that account for interlayer bonding resistance should be applied. Other characteristics of the fragmented specimen are revealed through morphological investigation. The longitudinal rasters aligned along the tensile load reveal a distorted cross section with some yielding before failure (see green arrows), while the transverse rasters were not deformed

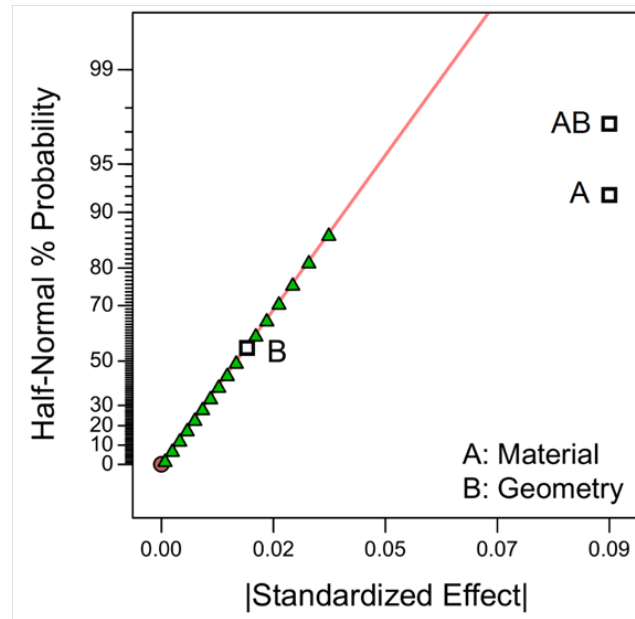


Figure 2.16: Normal probability plot for tensile test (Young's modulus response).

and had some adhesive failure zones (see red ellipses).

It's worth noting that the yielding happens just locally and for the longitudinal raster. The macroscopic behavior of the samples, as illustrated in Figure 2.15, does not represent this. In comparison to other research, the level of fiber-to-fiber fusion for the studied specimen appears to be lower [101]. The raster orientation appears to affect crack propagation as well [83]. This study emphasizes the significance of determining the interlayer bonding for these samples.

Because there are no significant constraints due to the clamping of the samples, the ISO 178 flexural test is regarded a testing method that allows some of the limitations of tensile testing to be overcome [54]. The flexural test used in this study was not performed on a tubular geometry like the one used by Kuznetson et al. [54], but rather according to ISO 178. The tubular geometry limits the ability to modify raster orientation in the printed sample, which is why this option was chosen.

As a result, we adopted the standard ISO 178 geometry, as shown in Figure 1, which allowed us to use the same raster orientation as the tensile load samples. The flexural test experimental curves reveal no major variations between specimens derived from bars printed with varying lengths (Figure 2.19). The maximum flexural stress measurements for the two materials ranged between 77.48 MPa and 108.02 MPa (Table A.3). In their investigation, Gebisa et al. [34] found flexural stresses ranging from 52.89 MPa to 126.30 MPa.

Despite the fact that the material type appears to be the only relevant factor (p -value = 0.0379) in this experimental study (Table 2.8), the small R -squared = 0.22 and adjusted R -squared = 0.17 values obtained from the ANOVA analysis show

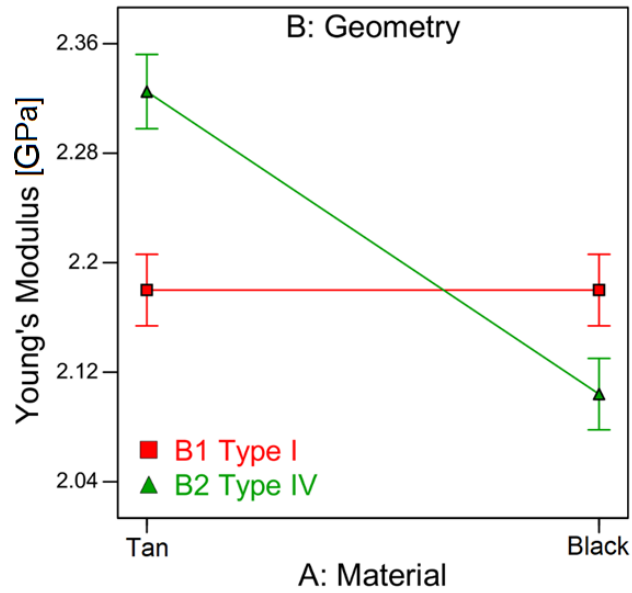


Figure 2.17: Effects plot for tensile test (Young's modulus response).

that the investigated factors account for only a small fraction of total flexural stress variability. When applied to FDM printed specimens, this exposes a high amount of noise impacting the flexural stress, which dramatically affects the test sensitivity, similar to the tensile test.

This result can be explained by the fact that the shear stresses developing within the specimen during a flexural test can influence its results. As a result, the ISO 178 standard minimizes its influence by setting the ratio (r) of support length (LS) to specimen height (h) to 16 [40]. Clearly, this situation is unfavorable for mechanical evaluation of FDM samples, since interlaminar bonding—whose resistance can be assessed by the presence of shear stress—plays a significant role in the specimens' mechanical properties.

Source	Sum of Squares	df	Mean Square	F Value	p -Value
Model	385.27	1	385.27	5.02	0.379
A-Material	385.27	1	385.27	5.02	0.379
Residual	1381.04	18	76.72		
Lack of Fit	72.47	2	36.24	0.44	0.6497
Pure Error	1308.56	16	81.79		
Cor. Total	1766.30	19			
Std. Dev.	8.76	R-squared	0.2181		
Mean	95.89	Adj. R-squared	0.1747		
C.V. %	9.13	Pred. R-squared	0.0347		

Table 2.8: ANOVA table for flexural test (response: flexural strength).

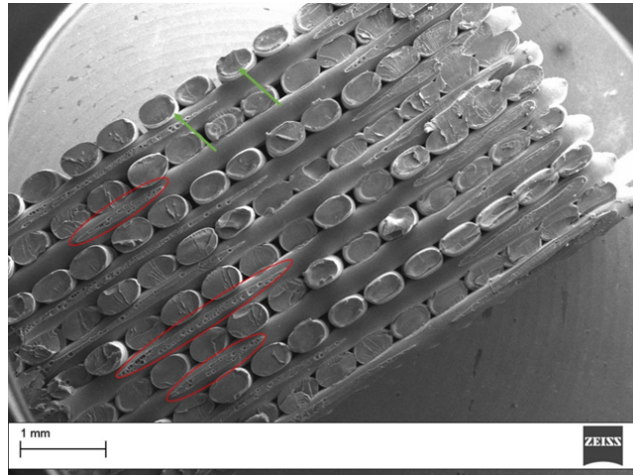


Figure 2.18: Fracture surface morphology for a tensile sample (tan resin). Red ellipse highlights the adhesive failure on the transverse rasters. The green arrow highlights the yielded longitudinal rasters.

The SBS test is a viable alternative for quickly determining the ILSS among the various test techniques commonly used to describe fiber-reinforced polymers. The span-to-thickness ratio is set for this test to ensure that the shear stresses within the specimen are high in comparison to the normal stresses caused by the bending moment [40]. Figure 2.20 shows the average ILSS vs displacement curves for the ULTEM 9085 samples (also see Table A.4). The effect of the material type is instantly apparent from these curves, with the black resin having a higher SBS than the tan resin.

The SBS readings for all of the specimens examined ranged from 11.82 MPa to 16.74 MPa. Table 2.9 and Figure 2.21 exhibit the results of the ANOVA analysis for the experimental design and the normal probability map of the effects, respectively. The residuals from the analysis were checked for model adequacy and found to be normal. The material type is definitely the influent factor (p-value 0.0001) on the ILSS, as expected. Neither the geometry nor the material type-geometry second-order interaction were important. However, the material type with R-squared = 0.92 and adjusted R-squared = 0.92 has a very high portion of variability (more than 90%).

The material type factor's influence is clearly displayed in the main effects diagram in Figure 2.22. The average of the ILSS observations and the 95 percent confidence intervals for the mean ILSS for tan and black, respectively, are shown by the two black square points and the intervals on the diagram. When plotting the main effects diagram at level 165 mm, the same result was obtained (not shown here).

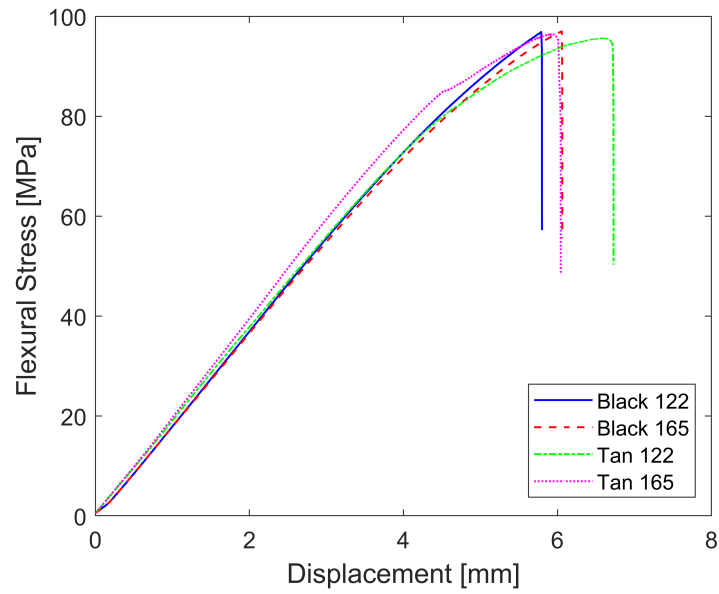


Figure 2.19: Average flexural stress versus displacement curves.

Source	Sum of Squares	df	Mean Square	F Value	<i>p</i> -Value
Model	57.83	1	57.83	217.84	<0.0001
A-Material	57.83	1	57.83	217.84	<0.0001
Residual	4.78	18	0.27		
Lack of Fit	0.75	2	0.37	1.48	0.2569
Pure Error	4.03	16	0.25		
Cor. Total	62.61	19			
Std. Dev.	0.52	R-squared	0.9237		
Mean	14.07	Adj. R-squared	0.9194		
C.V. %	3.66	Pred. R-squared	0.9058		

Table 2.9: ANOVA table for ILSS test (response: short-beam strength).

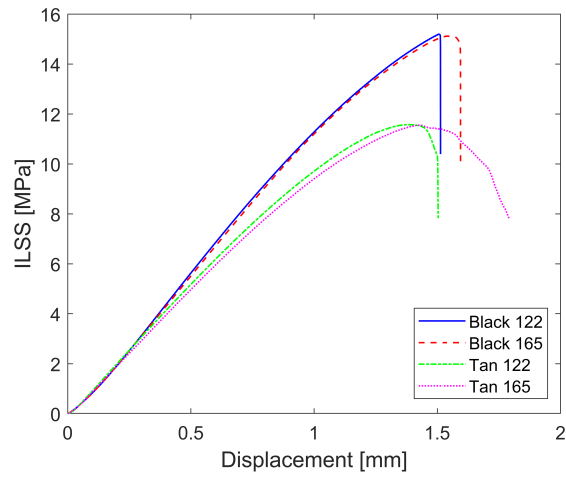


Figure 2.20: Average ILSS versus displacement curves.

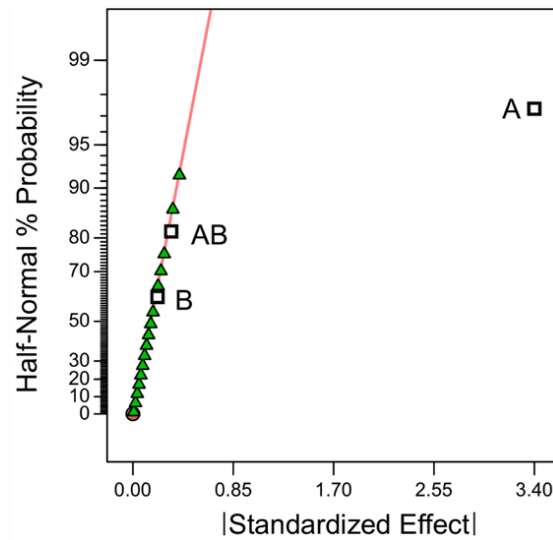


Figure 2.21: Normal probability plot for SBS test. A: material; B: geometry; AB: interaction.

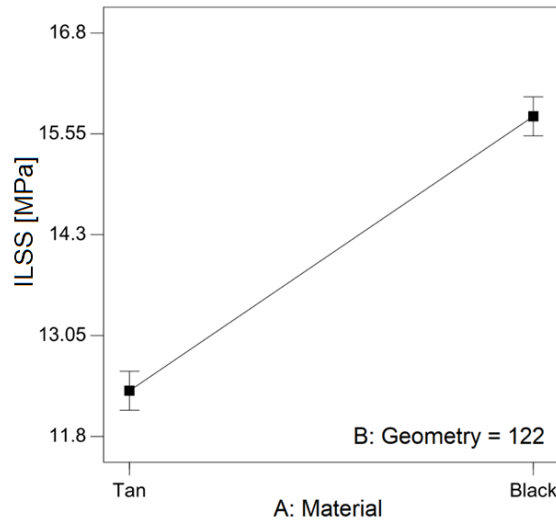


Figure 2.22: Effects diagram for SBS test.

Further investigations

By designing a replicated 2^3 screening plan, the combined influence of the material, specimen geometry, and testing tensile side (Figure 2.23a) on the response of the SBS test (Interlaminar shear strength, ILSS) was further explored. The study looked at three independent variables (factors): material (factor A), printed bar geometry (factor B), and tensile testing (factor C) (factor C). For each scenario under investigation, the number of replications has been set to $n = 5$. As a result, 40 experimental runs have been completed.

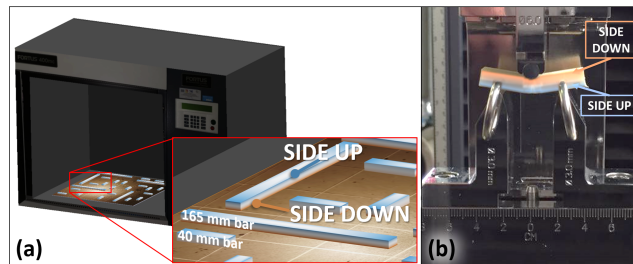


Figure 2.23: SBS specimens: (a) side down is the face on the build platform during printing, side up is the opposite one; (b) TUP testing configuration is shown and it means that the fibers stretched belong to the side up.

Figure 2.24 shows the average ILSS vs. displacement curves obtained for the ULTEM 9085 and PC samples. The ILSS values for the specimens examined range from 11.64 MPa to 14.65 MPa. The curve morphologies are similar to those seen in previous tests on similar samples [86] and PLA reinforced samples [12]. As the interlaminar cracks travel across the sample, the curve diminishes once a maximum ILSS value is attained.

The ILSS values of samples acquired using the shorter bar geometry (40 mm) were greater than those of samples produced using the 165 mm longer printed bars. Finally, the ULTEM 9085 has greater ILSS values than the PC due to the tensile testing side (i.e. TUP setup).

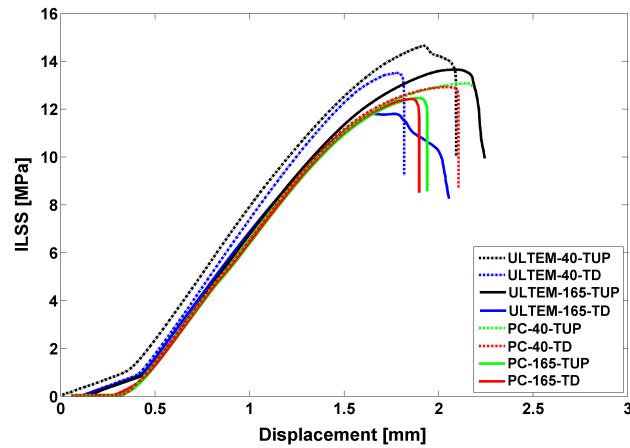


Figure 2.24: SAverage ILSS vs. displacement curves.

In a half normal plot, the statistical significance of the effects of material, geometry, and tensile side on the ILSS is displayed (Figure 2.25). The main effects diagram (Figure 2.26) depicts how all factors interact. All of the variables (material type (A), geometry (B), and tensile side testing (C)) are significant (Figure 2). This is to be expected when the material type changes, but the influence of the other two factors is worth noting.

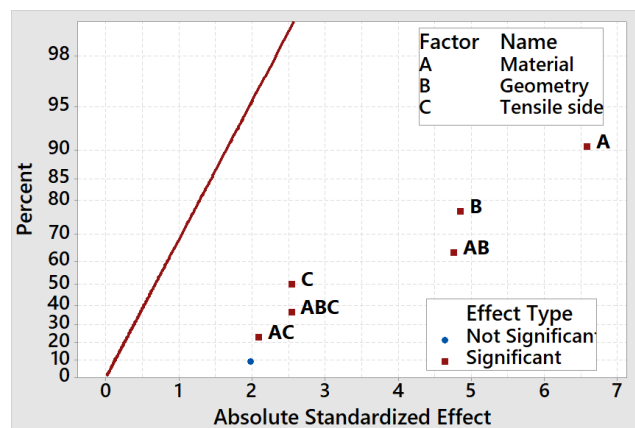


Figure 2.25: Half normal effects plot for ILSS.

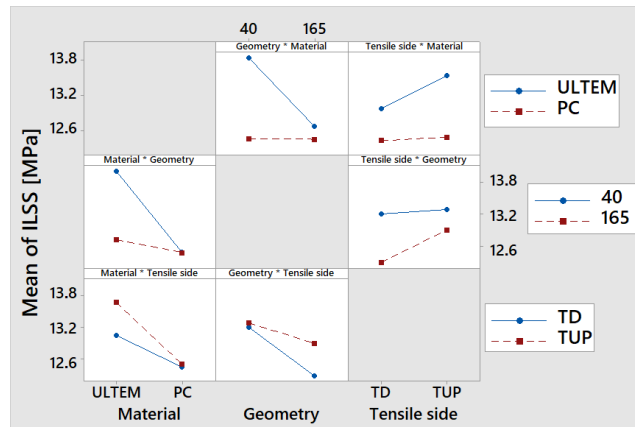


Figure 2.26: Interactions plot for ILSS.

The interaction plot (Figure 2.26) reveals a new feature: ULTEM 9085 is more sensitive to testing orientation (TD, TUP) relative to printing side and printed bar shape (40, 165) than PC samples. As a result, while testing sophisticated engineering polymers, extreme caution should be exercised in selecting the testing orientation in relation to the printing side, as this may have an impact on the results.

2.2.2 Mechanical characterization of CF-reinforced FFF components

FFF filaments loaded with carbon fibers (CF) are particularly interesting for their use in the automotive, robots, drones, prosthetics and orthotics fields [47]. Among the most used materials as matrices there is polyamide 6, however there are not many studies correlating the mechanical properties and printing parameters of these composite filaments [6].

Two different commercial carbon fiber reinforced filaments were selected for this work: XT-CF20 by ColorFabb® and ID1030-CF10 by Novamid®. XT-CF20 is a copolyester, filled with 20 wt% of milled carbon fiber reinforcement and proprietary additives. ID1030-CF10 (later indicated with PA66-CF10) is a copolyamide PA6/66 reinforced with 10 wt% of short carbon fibers.

All the specimens were printed on the Zortrax M200 (Zortrax, Olsztyn, Poland). Samples were modeled according to the dimensions of the different mechanical testing standards used in this work (ASTM D638, D2344M and D5420).

To characterize the mechanical behavior of the two CF reinforced filaments and to understand which mechanical test can be properly used for this kind of FFF printed material, the combined effect of the material and specimen geometry on the results of different mechanical tests was investigated in our experimental study. For each test, a factorial design was studied. The categorical factors were considered: material and raster angle, varied at 2 and 3 levels, respectively (Table 2.10). The statistical analysis of the experimental plans was performed by using Design-Expert software (Stat-Ease, Minneapolis, US). The experimental setups for the three mechanical tests are shown in Figure 2.27. The tensile tests were performed on a universal testing machine Instron 5985 (Instron, Milan, Italy) equipped with an extensometer of 25 mm gauge length, with a load cell of 10 kN, in strain control at speed of 2 mm/min. For the SBS tests, the same machine for tensile tests was utilized, with the 3PB tool required by ASTM D2344M, setting a span length of 24 mm and controlling the speed of the crosshead at 1 mm/min. The short beam specimens measured $40 \times 12 \times 6$ mm³. The low velocity impact tests were performed in accordance with ASTM D5420. The specimens were printed in squares measuring $80 \times 80 \times 4$ mm³ and tested on an Instron/CEAST 9340 drop tower equipped with a hemispherical tip (diameter of 12.7 mm). The target kinetic impact energy was fixed at 2 J by setting the height of the weight (equal to 3.055 kg) at 67 mm.

Test	ASTM	Factors	Unit	Levels
Tensile	D638	Material	-	XT-CF20, PA66-CF10
		Raster angle	[deg]	0, 45/135, 0/90
SBS	D2344M	Material	-	XT-CF20, PA66-CF10
		Raster angle	[deg]	0, 45/135, 0/90
Impact	D5420	Material	-	XT-CF20, PA66-CF10
		Raster angle	[deg]	0, 45/135, 0/90

Table 2.10: Factors and levels of the designed plan.

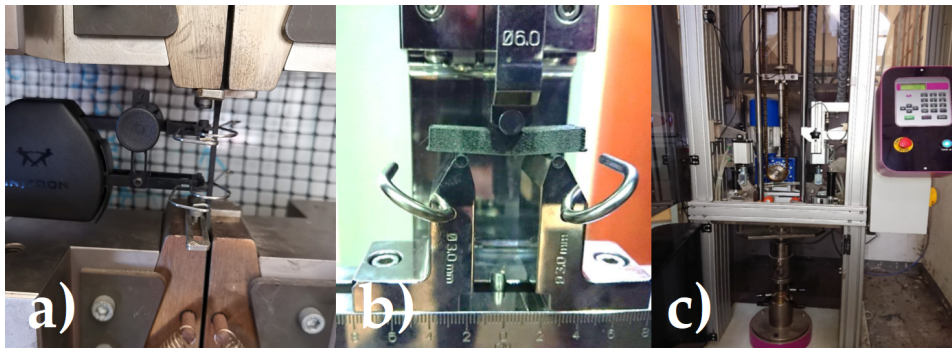


Figure 2.27: Experimental setups for: a) tensile, b) SBS, b) impact test.

Tensile test

In addition to the factors visible in Table 2.10, the factor Drying was considered for tensile test. The collected data visible in A (Figure A.6), were analyzed by statistical software and the results were reported in the digagrams of the effects in Figure 2.28 for the Young's Modulus response and in Figure 2.29 for the responses Yield Stress and Elongation at Break.

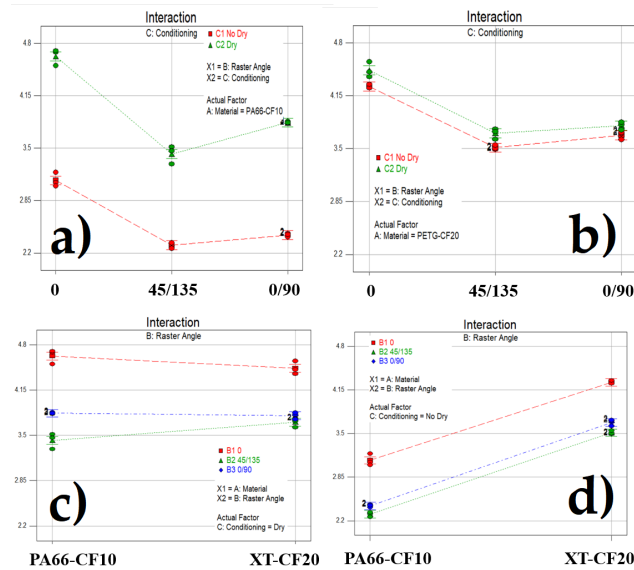


Figure 2.28: Effects plot for tensile test, response Young's Modulus (GPa): a) PA66-CF10, b) XT-CF20, c) Drying, d) Not Drying.

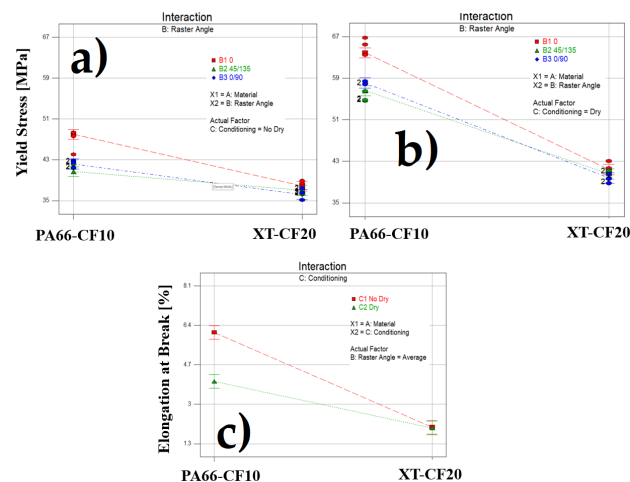


Figure 2.29: Effects plot for tensile test, responses Yield Stress a) and b), Elongation at Break c): a) Not Drying, b) Drying, c) Average raster angle.

Figure 2.28a shows the beneficial effect that Drying has on the PA66-CF10 molded yarn (improvement of Young's Modulus of about 65%). This effect is less marked, on the other hand, in the XT-CF20 filament (Figure 2.28b), whose matrix is less sensitive to moisture absorption than the other filament. As for the raster angle, however, this factor is very influential. Figure 2.28c shows almost similar values between the two materials, but in both cases greater for 0°, intermediate for 0/90° and worse for 45/135°. Same trend, but with lower values for PA66-CF10 is noted in samples not subject to drying (Figure 2.28d). In Figures 2.29 a and b the effects plots for the Yield Stress response are shown. The highest values are shown for the 0° level of

the raster angle factor. Further improvements are appreciated when applying drying to the PA66-CF10 material. As regards the Elongation at Break response (Figure 2.29 c) the effects of the raster angle factor are not appreciated, but the differences between the two materials are confirmed and the effect that the drying process has only on one of the two.

Regarding the ability of the fibers to bear the load, it must be considered that the FFF printing process involves modifications to the fibers themselves. The lengths of the fibers with which the filament matrices are loaded were observed by SEM. The samples of filaments and 3D printed pieces were placed in a furnace until the polymer matrices were thermally degraded, finally the residue was observed for the SEM surveys (Figure 2.30).

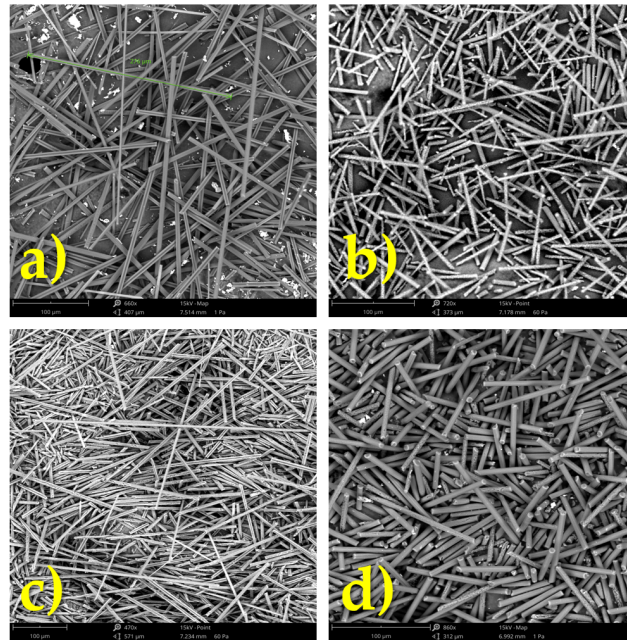


Figure 2.30: SEM images for: a) XT-CF20 filament, b) XT-CF20 printed, c) PA66-CF10 filament, d) PA66-CF10 printed.

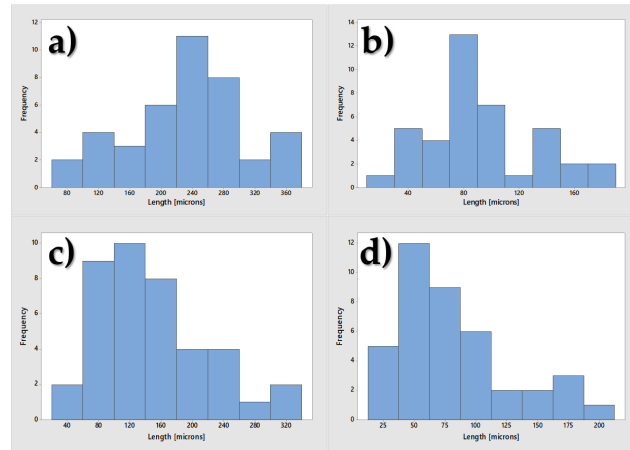


Figure 2.31: Frequency plots for the CF length of: XT-CF20 filament (a) and 3D printed parts (b); PA66-CF10 filament (c) and 3D printed parts (d).

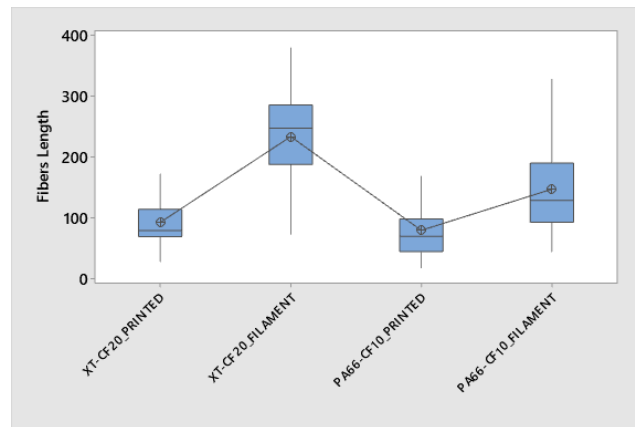


Figure 2.32: Box plot of CF length for printed and filament materials.

The surveys using ImageJ software showed the trends visible in the Figures 2.31 and 2.32. The XT-CF20 filament is characterized by fairly long fibers, with average values of about 232 microns. The same 3D printed material shows average length values around 92 microns (43% reduction). The unprinted filament of PA66-CF10, on the other hand, is characterized by 146 microns long fibers, which collapse to values of about 79 microns (reduction of about 60%).

SBS test

The SBS test showed that the material and the raster angle are influential factors (p -value < 0.001) on ILSS and involved in a significant interaction (p -value < 0.001). The model appears to have an excellent robustness to define the observed response with a high R-squared value of 0.98. The effects plot (Figure 2.33) shows the influence of the factor raster angle on the response observed. Higher values are observed for samples printed at 0° , but this time lower values are observed for $0/90^\circ$ raster angles

values. The explanation for this behavior lies in the fact that interlayer bonding will be better in the case at 45/135 ° probably due to issues related to faster printing times. In fact, it is known that by default, for reasons of print head movements, the best combination of raster angles is 45/135. Therefore, since this test, unlike the traction test, measures the quality of the interlayer bonding, the orientation that gives a worse performance is precisely 0/90 ° as it involves slightly longer printing times and, therefore, a worse promotion of the bond between layers influenced by temperature dependent diffusion mechanisms.

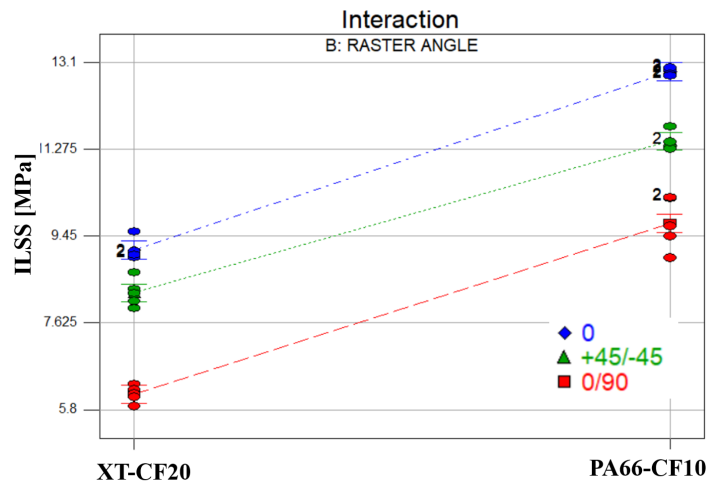


Figure 2.33: Effect plot for SBS test (response ILSS).

Impact test

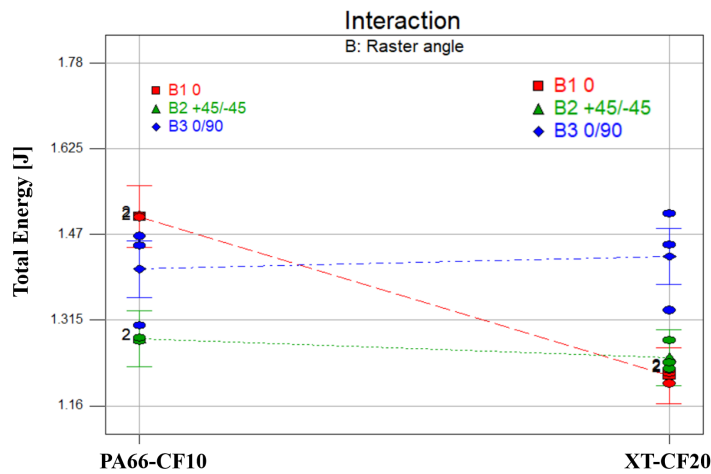


Figure 2.34: Effect plot for impact test (response Total Energy).

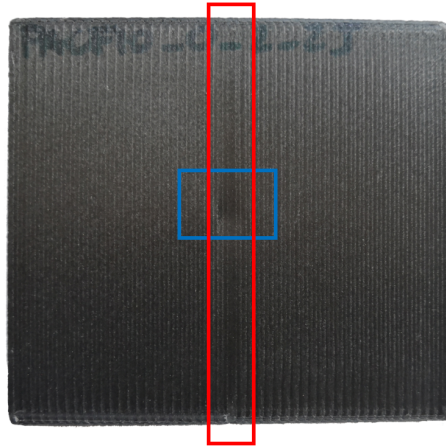


Figure 2.35: Impact tested sample (PA66CF10).

The impact test also confirmed the influence of the two factors studied, with a model having an R-squared of 0.84. In this case, both materials show similar properties for raster angles $45/135^\circ$ and $0/90^\circ$ (Figure 2.34). Significant differences between the two materials are observed only for the 0° raster angle, in terms of a greater capacity to absorb energy by the PA66-CF10 compared to the XT-CF20. The tensile tests confirmed what was observed for the ILSS tests.

The mechanical tests conducted on the FFF printed samples with two different commercial carbon fiber reinforced filaments PA66-CF10 and XT-CF20 while varying the raster angles, showed significant influences of these factors on the mechanical properties of the samples. It was observed that the PA66-CF10 has a better interlayer bonding and a greater capacity to absorb energy where the type of infill is done with a raster angle equal to 0° .

AM materials and techniques for Composite Tooling

The outcomes of research conducted in the field of Additive Manufacturing (AM) will be described in this chapter. By dissolving or breaking the AM model, this approach has permitted the creation of composites using removable mandrels, as shown. Other application examples will be presented in addition to the typical FDM (Fused Deposition Modeling) technique. Aside from composites production, research has been done on the formulation of materials for additive manufacturing, especially photocurable resins for LCD (Liquid Crystal Display) printing.



Figure 3.1: One of the application of industrial interest for the company involved in the AMA PhD (handlebar bike).

3.1 AM mandrels

3.1.1 FDM mandrels

All of the tools were produced on a Stratasys Fortus 400mc printer using the proprietary support filament SR100 for the soluble tooling and Polycarbonate (PC) for the matching mold, as shown in Figure 3.2. Using the proprietary software Insight, the printing process was modeled (Stratasys, Los Angeles, USA). The settings used to print all of the tooling are listed in Table 3.1.

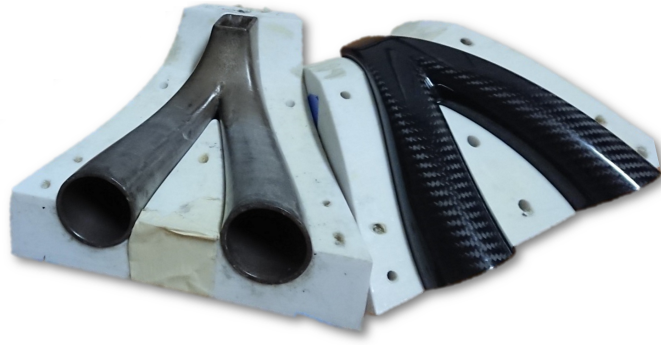


Figure 3.2: Mandrel, mold and composite part.

Specimen	Start speed [mm/s]	Infill type	Fill cell size [mm]	Raster angle [°]	Layer height [mm]	Contour width [mm]	Raster width [mm]
Hollow Intake	20-30	Solid	-	0/90	0.254	0.5080	0.5080
Honeycomb	20-30	Hexagonal	7.5	0/90	0.254	0.5080	0.5080
Intake Mold	20-30	Hexagonal	4.5	0/90	0.254	0.5080	0.5080

Table 3.1: FDM settings for prining tooling.

In the studies, Torayca’s GG200T DT121R carbon fiber prepreg was used. The following cure cycle is recommended by the prepreg manufacturer: • Increase temperature to 135 °C with a 2 °C/min heating ramp; • Hold temperature and pressure for 120 minutes; • Reduce temperature to 35 °C with a 3 °C/min cooling ramp. Positive pressure was applied to the intake’s inside surface using inflatable bladders. The inflatable bladders were created using Mates Italiana’s (Segrate, MI) MINI-TUBE 70 vacuum bag tubular release film, which was then employed to make the intakes when hollow tooling geometries were used, as mentioned in the discussion section.

In conventional autoclave processing, inflatable bladders are commonly employed in the manufacture of hollow composite parts [77]. For the generation of the composite intake, two processing procedures were investigated and compared. The typical method requires for the uncured prepreg to be set out inside a matching mold. For our trials, we used FDM printing to create a PC-matched mold. We also examined using a stainless steel mold in the manufacturing simulation.

By using an FDM created replica of the intake as a mandrel, the new solution avoids the necessity of a matching mold. This mandrel is used to wrap the prepreg and cover it with a vacuum bag. For the experiments, two types of mandrels were used: the hollow intake (Figure 3.3a) is hollow with a 3 mm wall thickness; the honeycomb intake (Figure 3.3b) is filled with a honeycomb structure (cell 7.5 mm

wide) and two running channels printed inside to improve the solvent wet out for the mandrel dissolution process. The inflatable bladder was only used inside the hollow intake to prevent it from collapsing when the autoclave’s curing pressure was applied.

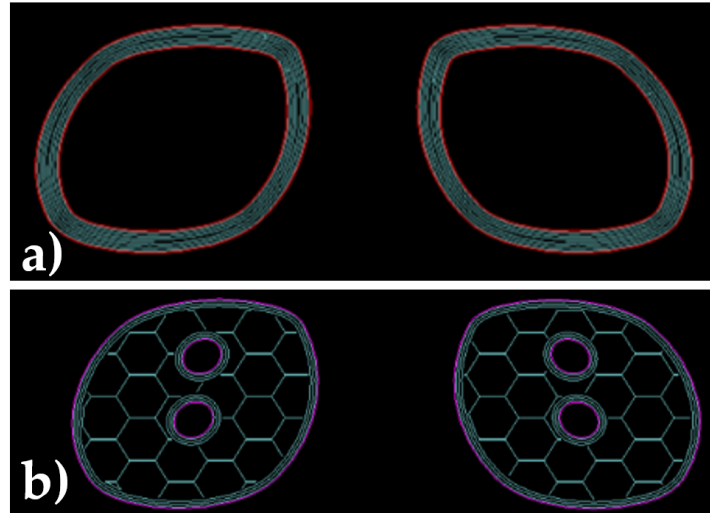


Figure 3.3: Intake mandrel geometry: a) Hollow intake; b) Honeycomb intake. Mandrel cross section.

Hollow composite pieces with complex forms might be difficult to manufacture. Because the change in cross-section from cylindrical to square, as well as the curved V shape, the intake geometry chosen for this investigation (Figure 3.2) is a good example, extracting any mandrel from the cured component is challenging. In these situations, ACS’s typical procedure is to employ a matching mold with an inflated mandrel within. The inflatable mandrel allowed the prepreg to be compacted throughout the curing process, resulting in high-quality composite products.

The typical layup procedure necessitated high technical lamination abilities, and this method produced a consistent flash that needed to be eliminated at the mold joint. This wastes prepreg and causes finishing processes to take longer. Furthermore, this method only allows for the production of one part per mold every cure cycle. This is a limiting constraint since autoclave curing has a high running cost (50 €/h according to ACS internal modeling), which forces numerous parts to be cured in a single cure cycle. This challenge can be solved by using soluble mandrels, which can cure several mandrels with carbon fiber wrapped on them in a single cure cycle.

We used a regular industrial order for 40 intakes to be built in one week to measure the cost and manufacturing time differences in a real-world setting. We modeled the production costs using these assumptions, and the simulation is reported as a cost breakdown in Table 3.2. The manufacturing time for each step is based on the actual manufacturing time measured during the experiments, taking into account

3. AM materials and techniques for Composite Tooling

the autoclave capabilities available at ACS. The cost breakdown solely applies to the hollow mandrel.¹

		FDM-PC		Stainless	FDM		
		Mold		Mold	Mandrel1		
Material	Description	Q.ty	Cost [€]	Cost [€]	Description	Q.ty	Cost [€]
		Mold	8	3,880.08	5,600.00	SR100	40
	GG200 TDT121R	1.44	34.56	34.56	GG200 TDT121R	1.44	34.56
Steps	Description	Time [h]	Cost [€]	Cost [€]	Description	Time [h]	Cost [€]
	Nesting	4	100.00	100.00	Nesting	4	100.00
	Lay-Up	20	505.76	505.76	Lay-Up	20	505.76
	Autoclave	16.5	825.00	825.00	Autoclave	9.9	495.00
	Part demolding	20	500.00	500.00	Dissolution	20	265.00
	Finishing	12.8	320.00	320.00	Finishing	0.8	€ 20.00
	Total	73.3	6,165.40	7,885.32	Total	54.7	5,546.12

Table 3.2: Cost breakdown for the different manufacturing strategies. The unit for the prepreg GG200TDT121R is square meter.

The cost analysis cannot be restricted to the cost of the mold and mandrel alone, as shown in Table 3.2. It must include all processing steps. When it comes to tooling costs, the FDM mold is the most cost-effective option, costing 3,880.08 € for 8 molds against 4,216.00 € for 40 mandrels. When all manufacturing processing stages were taken into account, however, sacrificial mandrels were less expensive and faster than FDM molds (5,546.12 € against 6,165,40 €; 58.0 h compared 73.3 h). When compared to stainless steel, the savings were much greater.

Additional time and expense reductions occurred from the dissolution operation (0.8 h vs 12.8 h) and the reduced finishing (0.8 h vs 12.8 h) when compared to demolding. Using an oven instead of an autoclave (at a cost of 20 €/h) and increasing the number of intakes processed per cure cycle can further minimize manufacturing costs and time. In terms of cost and time savings, the usage of soluble intakes proved effective. The mandrel dissolution process, on the other hand, takes place in an aqueous acid solution at a rather high temperature (85 °C). To achieve significant mandrel removal while using the hexagonal infill, at least 3 hours of solvent treatment were necessary (Figure 3.4).

¹The cost breakdown refers to the hollow mandrel only.

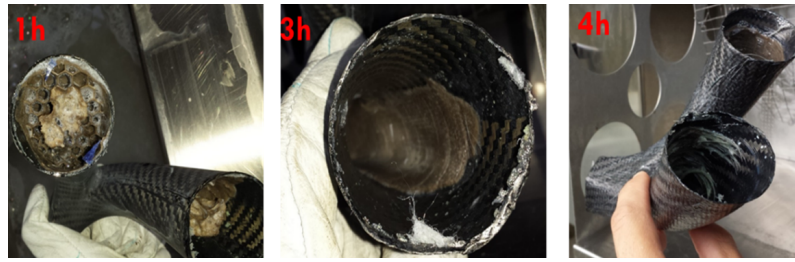


Figure 3.4: Stages of the dissolution process for the honeycomb intake.

If no mechanical removal was used, the mandrel needed to be completely washed out after 6 hours of treatment. This process may have a negative impact on the final qualities of the composite. After 6 hours of treatment, the T_g of the treated samples dropped from 122 °C to 106 °C, compared to 122 °C for the untreated sample. The decrease in T_g can be attributed to matrix plasticization (Figure 3.5).

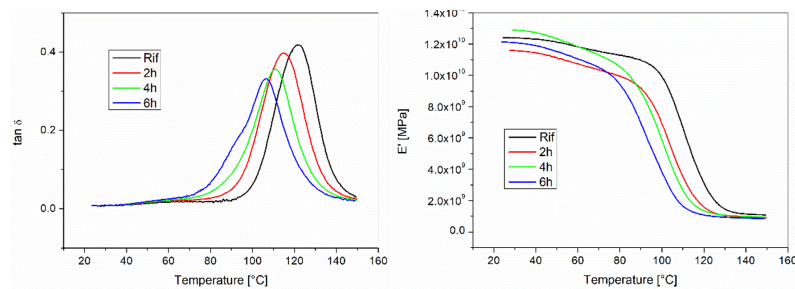


Figure 3.5: $\text{Tan}\delta$ and E' versus temperature diagrams for the composite specimens treated for different time in the ultrasonic bath. The sample Rif refers to the untreated sample.

3.1.2 FDM/LCD comparison

Further investigations were conducted on AM technique, in particular on the use of LCD technology to print removable composite's tooling and to compare its use with standard FDM tools.

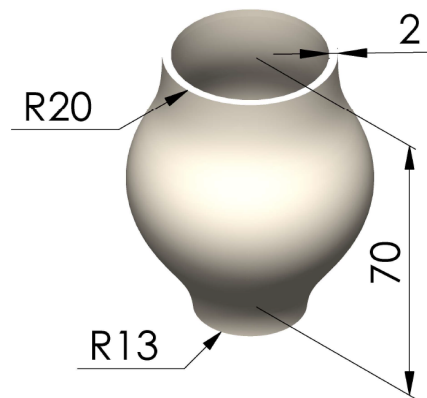


Figure 3.6: Model of the designed amphora to be manufactured in composites (all dimensions in mm).

Figure 3.6 shows the geometry that was chosen for the investigation. The geometry was in the form of an amphora. FDM tooling was manufactured using the proprietary support filament SR100 on a Fortus 400mc printer (Stratasys, Los Angeles, USA). LCD tooling was printed with the daylight resin Cream Hard on a Photocentric LC-HR2. The same prepreg and cure cycle were used as in the previous trial.

Hollow composite parts are difficult to create because the forms make it difficult, if not impossible, to extract the mandrel used to lay out the pre-preg or dry materials. Inflatable bladders are a technical answer, but they necessitate the use of matched molds that hold the bladder, which raises manufacturing costs. In order to optimize the utilization of removable mandrels, two options for mandrel manufacture were considered: soluble mandrel printed by FDM and break-away mandrel printed by LCD.

The break-away LCD mandrels are explained after the design and use of the soluble FDM mandrel is presented. Finally, the cost modeling of the two solutions is compared.



Figure 3.7: AM mandrels: a) FDM - shell 1 mm, b) FDM - shell 2 mm c) FDM - collapsed sparse design after applying the autoclave pressure (5 bar), d) LCD - breakable 2 mm mandrel with particular on the good internal surface quality.

The initial stage was to create the FDM mandrels by changing the shell thickness and infill design parameters. The design that was tested is shown in Figure 3.7a. The design option has an impact on the printing labor, with one empty mandrel printing in 1 h and one sparse mandrel requiring 3 h of printing time due to the additional material to be laid down. The empty mandrel with a 1 mm shell was too brittle to handle during lay up, and the infill sparse design could not withstand the autoclave pressure (Figure 3.7c).

Although the design with a 2 mm thick shell is a suitable compromise, it necessitated the use of an inflatable mandrel to maintain autoclave pressure. The surface of the FDM mandrel is rough because of layer markings. As a result, the mandrel was sanded by hand using increasingly finer abrasive sandpaper, ranging from 120 to 800 grit, to ensure a flat surface. The mandrel was removed after curing in an ultrasonic bath at 85 °C for 3 hours, using Stratasys' proprietary solution Waterworks™ to wash away the soluble mandrel. This method, as demonstrated in a prior article [84] may have an impact on the composite's characteristics.

Surface preparation and washing techniques were necessary for FDM. These are process limitations that LCD mandrels can help to solve. Photocurable thermoset resins are used to print the second type of mandrel in an LCD printer. The printed LCD mandrel was smooth and easy to work with throughout the layup. The mandrel was simply hammered when the autoclave was removed, relying on the brittleness of the thermoset resins (Figure 3.7d). In a matter of seconds, the mandrel was dismantled into little bits and removed from the part. The process has several advantages over FDM, including being substantially faster and avoiding the use of

strong solvents on the composites.

Cost modeling

The manufacturing cost is an important criterion for demonstrating the viability of a method. FDM showed to be cheaper and faster than the traditional way of employing stainless steel molds and inflatable bladders in a prior study on the fabrication of hollow intakes. The choice of AM approach has a clear effect on the removal time using LCD in the current investigation. The cost of mandrel fabrication, on the other hand, should be considered.

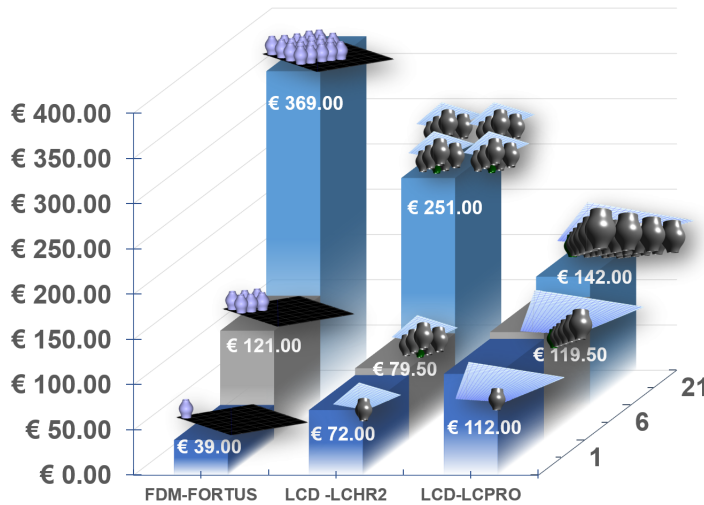


Figure 3.8: Cost modeling for different printers and number of amphoras to be produced (varied from 1 to 21).

We used Hopkinson and Dicknes' cost model to calculate the cost of mandrel production [46]. The modeling was done with the assumption of printing 1, 6, or 21 mandrels. Only six amphorae can be printed at a time with the LC-HR2 printer. As a result, a larger LCD printer (i.e., LC-PRO) was used to replicate the manufacture of 21 mandrels in one step. When a large number of ormandrels are printed, the graph clearly indicates that LCD outperforms FDM in terms of cost, with costs falling from 369 € to 142 €. The distinction stems from the fact that many pieces are printed in the LCD with a single layer projection, whereas FDM requires several extrusion head movements.

Further investigations

In addition to the exposed materials and techniques, a recent commercialized material was taken into account: Aquasys180 (Infinite Material Solutions, Wisconsin, USA), a filament used as support for printing PEEK by FFF (Fused Filament Fabrication) printing.

Three AM techniques were studied for producing mandrels: FDM, FFF, and LCD. Once the box-shape mandrels were obtained, male lamination and out-of-autoclave curing followed. Subsequently, the samples were obtained according to ASTM 7264 standard for flexural testing. Finally, the observed mechanical characteristics were compared. Further considerations were made about the quality of the internal surfaces of the hollow composites by SEM/AFM microscopic observations.



Figure 3.9: Box-shape mandrels.

In order to obtain useful geometries in providing both mandrel removal and mechanical comparisons, box-shaped geometries ($25 \cdot 25 \cdot 80 \text{ mm}^3$ and 2 mm of thickness) were selected. Figure 3.9 shows the production process that led to testing.

The box-shape mandrels were printed by three different techniques. As for the FDM printing, a Fortus 400 mc printer (Stratasys, Los Angeles, USA) was used. The FDM mandrels were printed in SR-100 soluble support material (Figure 3.10a). The FFF printed mandrels were obtained using an outsourced desktop printer and built in Aquasys180 material (Infinite Material Solutions, Wisconsin, USA), a filament used as support for printing PEEK, Figure 3.10b. The LCD mandrels were printed on the LC-Precision Ceramic printer from Photocentric (Peterborough, UK) using daylight Cream Hard resin (Figure 3.10c).

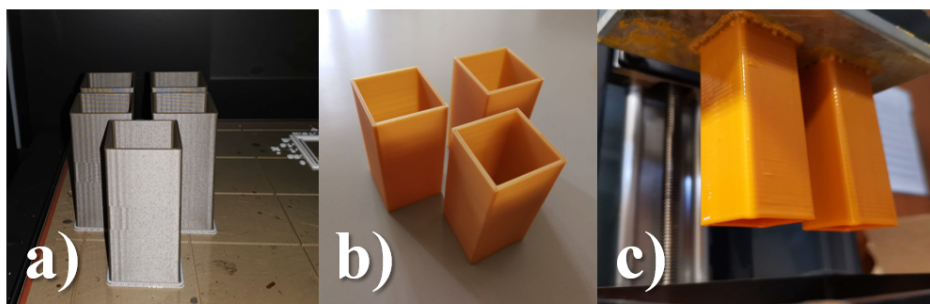


Figure 3.10: 3D printed mandrels, a) FDM; b) FFF; c) LCD.

Male lamination was carried out using carbon fiber prepreg named M79 by Hexcel. The curing took place out-of-autoclave, in an industrial oven at $90 \text{ }^\circ\text{C}$ for 240 minutes under vacuum bag pressure of 0.9 bar. The obtained FDM parts were dissolved in the proprietary Stratasys Waterworks™ solution, while the FFF mandrels were dissolved in water at $60 \text{ }^\circ\text{C}$. The LCD mandrel were removed by mechanical

breakage with a hammer. The composites thus obtained were cut by Dremel in the dimensions determined by the ASTM 7264 standard for the flexural testing of laminated samples (77.13.2 mm³). Mechanical tests were performed using an Instron 5985 universal testing machine (Instron, Milan, Italy) equipped with a load cell of 10 kN. The tests were carried out in strain control at the speed of 1.0 mm/min and a span length of 64 mm.

The removal of the mandrels (Figure 3.11) was monitored by measuring the times and the quantity of material removed. For the FDM mandrels, the complete dissolution of the soluble support SR100 took place in 3 h. As for the FFF mandrels, the removal took place in water at 60 °C in 30 minutes. Monitoring of the amount of dissolved mandrel in this case could not take place as the sacrificial material is removed not by total dissolution, but by absorbing water and becoming soft. Therefore, the gaps between composite and spindle were observed and mapped over time. Removal of the LCD mandrels took place in 2 minutes as the simple geometry allowed it. Once the composite parts were obtained, they were cut into bar samples (Figure 3.11) and tested. From the statistical analysis conducted on the data collected, it is clear that the FFF and LCD samples are the ones showing more similarities in terms of observed responses. In fact, as shown in the bar charts in Figure 3.12, the FFF and LCD samples show average Flexural modulus of 6.59 and 6.56 GPa respectively, while the FDM samples show average values of 5.07 GPa. Regarding the Flexural strength, no significant differences were observed, the average values of this response were 142.09, 140.90 and 145.07 MPa for FDM, FFF and LCD samples respectively. Another significant difference, however, was observed on the Elongation at break response, in fact the FDM samples showed the highest values of all, i.e. 4.12% vs 2.50 and 2.58% respectively for the FFF and LCD samples. This result was predictable following what was observed in the previous study [84], which showed that the matrix of the composite obtained by dissolving the FDM mandrel was affected by the sodium hydroxide solution and showed lower T_g values than the composite untreated, indicating a plasticization of the matrix.

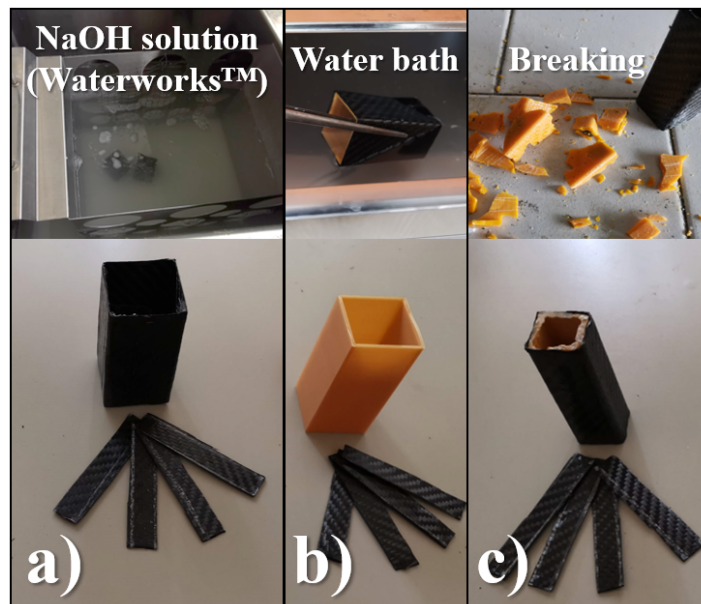


Figure 3.11: Mandrels removal and composite parts: a) FDM; b) FFF; c) LCD.

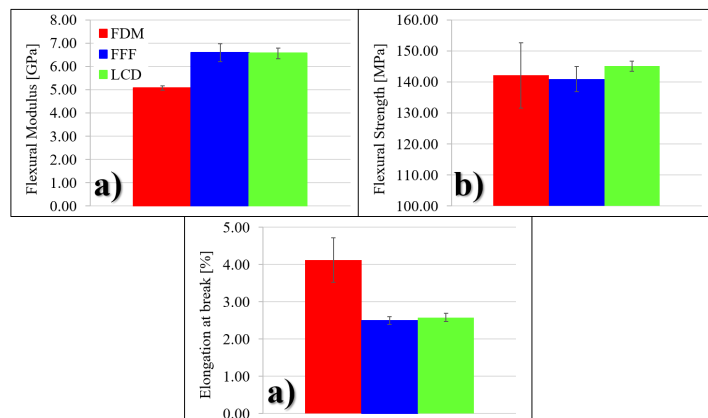


Figure 3.12: Bar charts of mechanical properties: a) Flexural modulus; b) Flexural strength; c) Elongation at break.

3.2 LCD resin Formulation

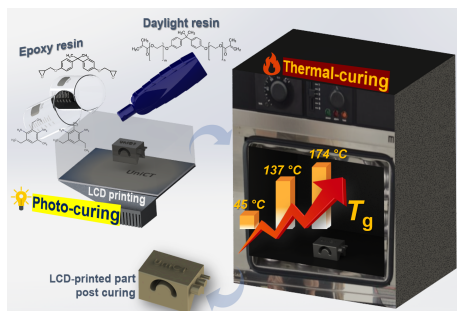


Figure 3.13: Graphical abstract of the cited work.

blending and dual curing as a means of improving resin thermal characteristics was investigated.

The improvement of the thermal properties of daylight resins by blending with epoxy thermally curable resins without changing the operating principle of the printer was one of the topics of research carried out during the PhD course. To accomplish this, a commercial daylight curing resin was chosen, and the thermal curing parameters of the resin following LCD printing were investigated. The impact of epoxy

The thermally curable epoxy resin was made by mixing diglycidyl ether of bisphenol A (DGEBA) and diethyltoluene diamine (DETDA) with the commercial daylight resin (Cream Hard) acquired from Photocentric Ltd. (Peterborough, UK). The Cream Hard resin is referred to as cream or C throughout the following, while the DGEBA/DETDA mixture is referred to as E. Huntsman (Basel, Switzerland) generously supplied the diglycidyl ether of bisphenol A, Araldite GY 240. Lonza (Basel, Switzerland) generously contributed the diethyltoluene diamine (DETDA). DGEBA and DETDA were combined in a 1:1 stoichiometric ratio at room temperature.

LonzaCure DETDA is a liquid aromatic amine that can be combined with liquid epoxy at room temperature. The resulting liquid epoxy formulation is miscible with daylight resins and does not react in direct sunlight. In a centrifugal planetary mixer, the uncured epoxy formulation was created by combining the two monomers (DGEBA and DETDA) (ARV-310 by Thinky, Laguna Hills, CA, USA). The following circumstances were employed for mixing: a speed of 2000 rpm, a vacuum pressure of 0.3 kPa, and a 5 minute mixing duration.

The epoxy-based blends were made by mixing the uncured epoxy formulation with the cream resin in various weight ratios at room temperature (Table 3.3). The blends were combined in the centrifugal planetary mixer in the same way as the uncured epoxy formulation was. Until employed, the created blends were kept in opaque glass containers to avoid light exposure. The samples held at room temperature for three months showed no signs of demixing or incompatibility. The centrifugal mixer allowed the two resins to be mixed in about 5 minutes while also applying deaeration to prevent air spaces in the cured systems.

ID Sample	Cream [wt%]	Epoxy [wt%]
C	100	0
CE7030	70	30
CE5050	50	50
E	0	100

Table 3.3: Resin formulations studied.

The LCD printing was carried out on a Photocentric LC-HR2 LCD printer (Peterborough, UK). The LC-HR2 is an LCD printing machine that displays resin photocuring on an iPad screen. Photocentric recommended the initial conditions for printing the cream resin. Following the printing trials on the epoxy-based mixes, the printing conditions were fine-tuned to ensure good printing quality (Table 3.4). In the findings and discussion section, the methods utilized to define the optimum printing parameters for the epoxy blends will be explained.

The printed samples were initially printed using LCD printing before being thermally post-cured in a standard ventilated oven using two different cure cycles: isothermal cure for a 3 hour hold time; and isothermal cure at 140 °C for 2 hours followed by a 2 °C/min ramp to 180 °C and a 2 hour hold time. Three temperatures were examined for isothermal curing of the cream resin: 100, 140, and 150 °C.

ID Sample	Exposure Time [s]	Z Lift Distance [mm]	Z Lift Speed [mm/min]	Z Retract Speed [mm/min]	Top Time [s]
C	25	3	15	50	5
CE7030	30	10	10	10	10
CE5050	30	10	10	10	10

Table 3.4: LCD printing conditions used for specimens manufacturing..

DSC results

A dynamic temperature scan employing differential calorimetry was used to assess the uncured cream resin before LCD printing. Figure 3.14 depicts the outcome. Starting at 150 °C, the graph indicates the presence of an exothermic peak centered at 180 C. (black curve). The total amount of exothermic heat released was 168.35 J/g. The exothermic peak in the daylight formulation suggests the existence of some thermally reactive groups. [61] The cream resin is a (meth)acrylate-based resin that can be cured by photopolymerization and heat.

After the initial scan, the cream resin was tested again, and no exothermic peak was found (Figure 3.14, red curve). This result demonstrates that the first scan interacted with all reactive moieties. In the second scan (red curve), the thermogram

clearly shows a glass transition temperature of 135.6 °C, which is greater than the T_g reported for the cream resin during LCD curing only (60 °C).

The enhanced crosslink density induced by the heat curing that occurred in the first scan can explain this improvement. DSC was used to describe the unreacted epoxy-based blends in their uncured form. Figure 3.15 summarizes the findings. Because of the existence of a larger concentration of thermally curable monomers, the addition of the thermally curable resin led in an increase in the released heat during the heating ramp (Figure B.1).

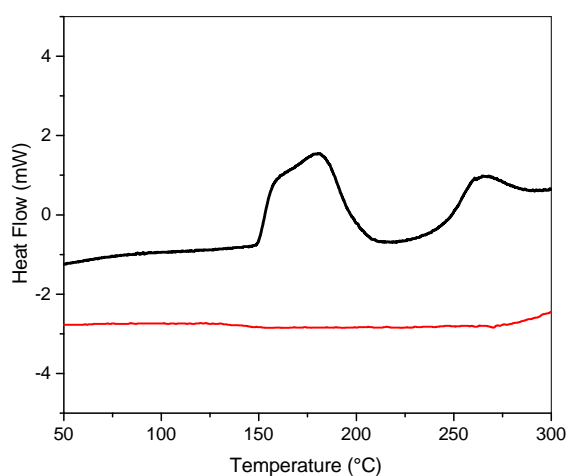


Figure 3.14: DSC analysis on the hard cream resin: first scan (black); second scan (red).

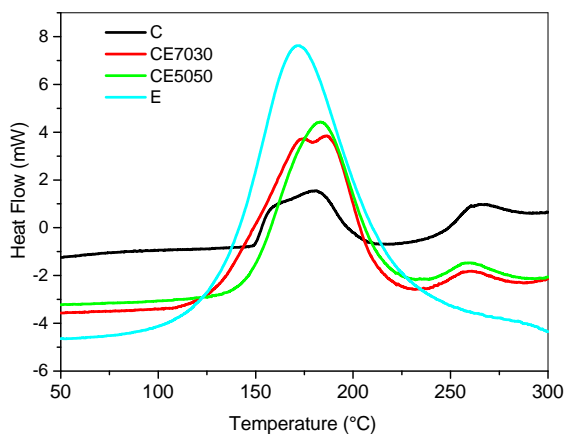


Figure 3.15: DSC analysis on the epoxy-based blends in their uncured state.

Rheology testing

The viscosity of the resin is a critical characteristic in LCD printing. To establish a homogeneous uncured resin layer between the bottom of the vat and the printing component, the resin must flow as the platform moves up and down. To enable resin printing on the LC-HR2 printer, Photocentric recommends a maximum viscosity (η^*) of 100 Poise. The commercial cream resin utilized in this study had a viscosity of roughly 1.8 Poise at room temperature. When the epoxy formulation was added, the viscosity increased as the epoxy content increased. CE5050, the blend with the highest epoxy concentration, has a viscosity of 12 Poise at room temperature (Figure 3.16).

The viscosity of the blend is mostly determined by the molecular weight of the epoxy prepolymer and may thus be modified with reactive diluents. At the same time, we increased the Tg values while keeping the blend's viscosity within printer standards. Notably, the Tg values obtained are higher than those produced by most current commercially available Photocentric systems, and they are also better than those acquired by other commercial systems (Table in B).

The resins that performed similarly were those sold by Carbon3D and based on a dual curing method. We can see that the proposed approach is fast and leads to comparable Tg performance when we compare the Tg results and full processing times we achieved with the results given on Carbon3D technology in the open literature [51, 66, 89]. The viscosity of the mixes investigated in this research is higher than that of commercially available systems. The mixes were all recognized as processable because the values were substantially below the prescribed limit of 100 Poise, which was validated by our printing test described in the following section.

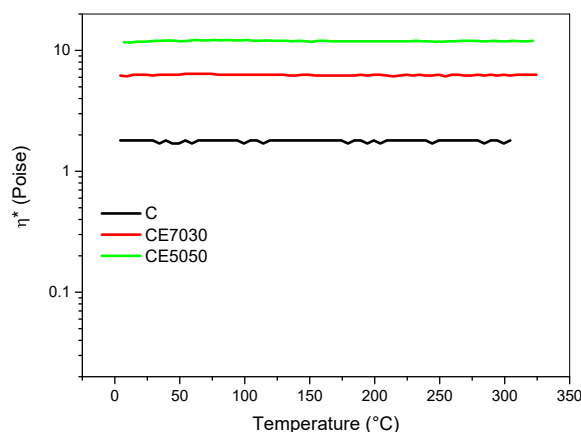


Figure 3.16: Complex viscosity of the uncured epoxy-based blends: C (blue); CE7030 (red); CE5050 (green).

Printing test

After the viscosity of the blend was determined, printing trials were conducted to acquire specimens for thermomechanical testing. The first printing trials with the CE7030 blend resulted in failure (Figure 3.17). The printing failed totally since no shape was generated and only a few cured layers were found placed on the vat films. In these tests, the same printing parameters utilized for the cream resin were used (see Table 3.4). The short exposure intervals did not appear to be long enough to allow for proper curing of the resin layers.

This is the result of two factors: the inclusion in the blends of an epoxy resin designated for thermal curing exclusively, which reduces the amount of photocurable moieties; and the photoinitiator's stoichiometric unbalance due to the epoxy resin addition in the blend formulation.



Figure 3.17: Printing trials for the CE7030 blend with the same printing conditions used for the cream resin (see Table 3.4).

The photocuring of one single layer was explored in greater depth utilizing the following approach to improve the exposure periods of the prepared blends. The printer was programmed to create a single-layer prism with a 10 mm square base. When using the cream resin, one single layer for the LC-HR2 printer results in a layer thickness of 100 microns. The uncured blend was dropped on a plastic foil and subjected to the LCD light with various exposure times, with the display configured to only project one layer for the prism.

Because the LC-HR2 printer uses a preset light intensity, this parameter was not looked into. After light irradiation, the uncured resin was gently washed away with a cloth soaked in isopropyl alcohol (IPA). A caliper was used to measure the thickness of the printed prism as a result of the process. A caliper was used to measure the side of the produced square prism, and the deviation from the prescribed side (i.e.

10 mm) was reported as width overcure (Figure B.3). See Table 3.5 for a summary of the findings. The results in the table reveal that when the epoxy resin is mixed with the photocurable resin, the blend's photo-reactivity is lowered marginally.

To accommodate for this effect, the exposure times for the CE7030 and CE5050 were increased from 25 seconds for the cream resin to 30 seconds for the CE7030 and CE5050 (Table 3.4). The resin flow during the platform's up and down movement, however, has an impact on the printing outcomes. The platform's controlled movement was changed to account for the blends' increased viscosity (Figure 3.16), as reported in Table 3.4 for the blends. The platform was raised to a distance of 10 mm instead of the 3 mm used for the cream, and the Z lift and retract were slower (i.e., 10 mm/min) than the cream resin printing to guarantee proper resin flow timing.

Exposure Time [s]	Thickness [μm]						Width Overcure [%]					
	C		CE7030		CE5050		C		CE7030		CE5050	
	Mean	Std Dev	Mean	Std Dev	Mean	Std Dev	Mean	Std Dev	Mean	Std Dev	Mean	Std Dev
5	-	-	-	-	-	-	-	-	-	-	-	-
10	32	1.0	-	-	-	-	-9.4%	0.14%	-	-	-	-
15	46	0.7	41	1.0	-	-	-8.1%	0.15%	-9.0%	0.17%	-	-
20	82	1.0	73	1.2	-	-	-4.7%	0.19%	-5.3%	0.20%	-	-
25	105	0.9	95	1.3	88	0.8	0.0%	0.14%	-2.0%	0.15%	-4.0%	0.13%
30	117	1.0	108	1.2	102	1.0	1.1%	0.20%	1.5%	0.12%	1.0%	0.19%
35	137	0.7	125	1.2	118	0.9	1.1%	0.16%	1.6%	0.16%	1.5%	0.12%

Table 3.5: Average mean values and standard deviations (Std Dev) of the printing trials on the square prism for the LCD printing optimization with the epoxy-based blends.



Figure 3.18: Printing trials for the CE7030 blend with the optimized printing conditions after photocuring optimization (see Table 3.4).

DMA testing

The results of the DSC testing revealed an exothermic peak for the uncured cream resin, indicating the existence of reactive moieties that lead to the system's thermal curing (see Figure 3.14). DMA [63] is a good approach for studying the thermal cure

of solid systems after vitrification. Isothermal DMA testing was used to examine LCD photo-cured samples at three different temperatures (i.e., 100, 140 and 150 °C). This test enables researchers to track changes in viscoelastic characteristics during isothermal curing. The storage modulus (E') was closely monitored over time.

The storage modulus of the cream resin tested at 100 °C for 3 h showed just a minor fluctuation, whereas the storage modulus of the isothermal test at 140 or 150 °C increased by one order of magnitude within the testing duration (Figure 3.19). The rise in storage modulus is due to crosslinking reactions that begin at 150 °C, as evidenced by DSC experiments (Figure 3.14).

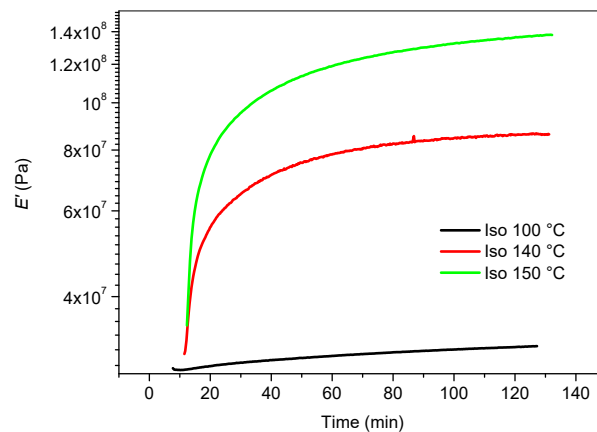


Figure 3.19: Isothermal DMA curing test on LCD printed Hard Cream specimens: Storage modulus versus time.

Following isothermal testing, the same samples were subjected to a ramp rate DMA test (Figure 3.20). At 65 and 126 °C, the system cured at 140 °C showed two Tan peaks. At 150 °C, the resin dried with one peak at 134 °C and a shoulder about 67 °C. The Tan peak of the specimen cured at 100 °C shifted slightly from 45 °C, as recorded for the LCD printed sample, to 50 °C.

The increasing crosslink density caused by the crosslinking events that occur during the heat curing of the cream resin results in a shift of Tg peaks, which corresponds to the glass transition temperature (Tg). An exothermic peak centered at 172 °C was observed in the epoxy DGEBA/DETDA system (Figure 3.15). As a result, the following post-cure cycle for epoxy modified blends was utilized to assure complete conversion of the epoxy moieties after LCD printing: isothermal cure at 140 °C for 2 h, ramp at 2 °C/min up to 180 °C, and hold at 180 °C for 2 h. A ramp test was used to examine the post-cured samples (Figure 3.21).

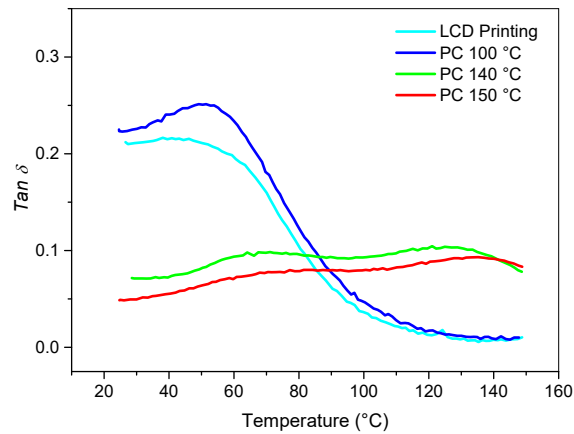


Figure 3.20: Ramp rate DMA test on isothermally cured Hard Cream resin.

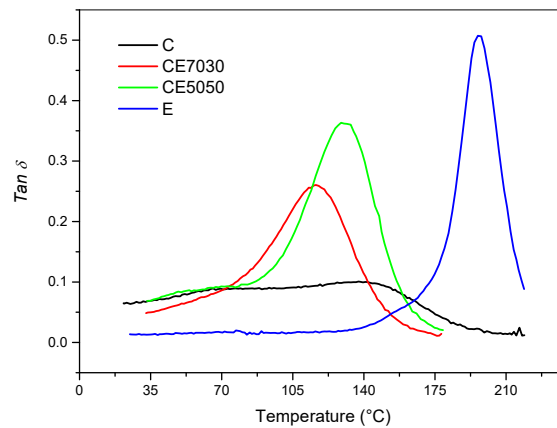


Figure 3.21: DMA analysis for the LCD printed sample after the post-curing cycle (isothermal cure at 140 C for 2 h, ramp at 2C/min to 180 C and hold at 180 C for 2 h).

If we evaluate commercial similar systems (Figure B.4), it can be concluded that dual curing resulted in resin with greater T_g . The glass transition temperatures (T_g) of the cream unmodified resin (C) were 70 and 137 °C, respectively, whereas the pure epoxy formulation (E) had a T_g of 197 °C. Epoxy mixing produced a single broad Tan peak with a T_g value of 174 °C for the 50:50 blend. When the two formulations were mixed together, the T_g increased as the epoxy content increased (Figure 3.22).

When only the high T_g for the cream resin is considered, the T_g versus epoxy content graph indicates a quasi linear relationship. This pattern is most common in blends that constitute the so-called interpenetrated network [13].

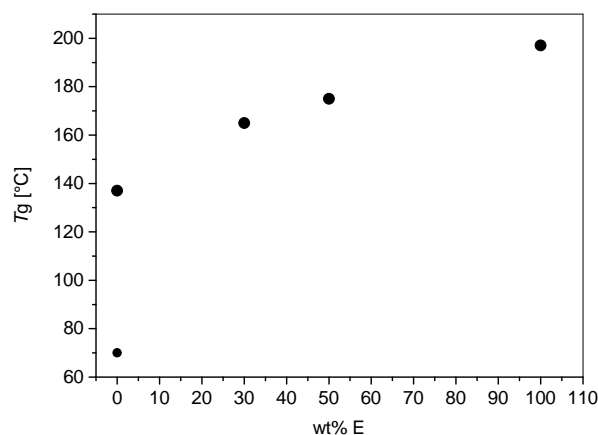


Figure 3.22: Glass transition temperatures (T_g) obtained as T_{\tan} peaks measured by DMA plotted versus the epoxy content.

Conclusions

The use of daylight curable (meth)acrylate-epoxy mixes was investigated. Calorimetric examination of the daylight resin revealed the presence of thermally reactive moieties. With the information gathered from DSC analysis, dynamic mechanical analysis revealed that LCD printed parts do not build fully crosslinked networks coherently. The glass transition temperature of LCD printed daylight resins was enhanced from 45 to 137 °C with thermal postcuring. This T_g enhancement was achieved using a post-treatment that took around 4 hours and 20 minutes of extra heat curing time. When DGEBA/DETDA resin was added to the formulation, the benefits of thermal post-curing were amplified even more. For blends containing 30 and 50 wt% DEGBA/DETDA, the T_g increased to 165 and 174 °C, respectively. However, due to the longer photocuring durations required to achieve acceptable quality LCD printing, these significant T_g gains have several disadvantages. To allow resin flow, the exposure period was changed from 25 seconds for hard cream resin to 30 seconds for epoxy-based mixes, and the platform was relocated higher and slower.

Metal AM for Tooling and Inserts

The need for a deconstructed supply chain also implies the presence of a hybrid manufacturing. In fact, during the AMA PhD project, some metal inserts (especially those relating to the use of innovative solutions such as LCD mandrels) were designed and printed using desktop FFF printers. Further applications (i.e. molds for injection molding) will be shown both in terms of material, time and costs incurred. However, this technology, known as Metal FFF or Metal Extrusion, has several disadvantages and, above all, being a recent application, it does not have much data at the basis for a systematic and predictable design (see shrinkages prediction).

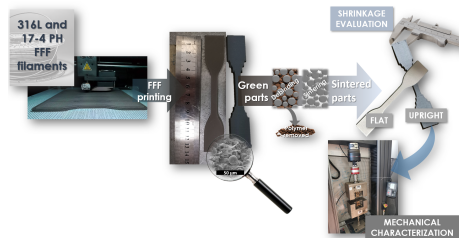


Figure 4.1: Graphical abstract of the cited work. [87]

In this chapter, a comparison of two hybrid metal/polymer systems is presented: BASF’s Ultrafuse 316L and Markforged’s 174 PH system. The tensile characteristics of the sintered parts were determined by examining the mesostructure of the green and sintered parts using Scanning Electron Microscopy and Energy Dispersive Xray spectroscopy. Analogous metals created using common 3D printing metal processes were compared to the results.

The rising use of such materials on widely used printers necessitated this research. As a result, we planned to extend the study by printing Ultrafuse 316L on a low-cost printer that had never been reported before, as the standard specifications provided by BASF had only been obtained on Ultimaker series machines. A detailed investigation of the mesostructure and the influence of the real load bearing region is also presented. The findings of this study were published in a scientific publication as a paper [87].

4.1 Stainless steel 316L particles filled filament

The supplies were purchased from a commercial source. Markforged’s technology was employed for the 17-4 PH system, while BASF’s Ultrafuse 316L was used for the 316L filaments. The Ultrafuse 316L filament is a nonslip metal–polymer combination that may be used in any Bowden or direct-drive extruder. We used a desktop-size Zortrax (Zortrax S.A., Olsztyn, Poland) 3D printer with a 0.4 mm bronze nozzle for this study. The Ultrafuse 316L printing settings were derived from those stated by BASF in their technical data sheet tested on a calibration cube. The printing options are listed in Table 4.1.

As recommended by BASF, the postprocessing of the 3D-printed samples was outsourced to a debinding and sintering service.

Printing Parameters	Lightweight
Nozzle size [mm]	0.4
Retraction distance [mm]	2
Retraction speed [mm/s]	40
Layer height [mm]	0.14
Infill [%]	6100
Nozzle temperature [°C]	240
Bed temperature [°C]	90
Oversizing factor [%]	19.98
Oversizing factor [%]	26.03

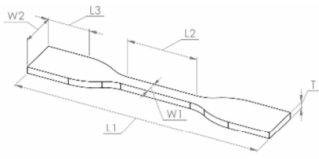
Table 4.1: Printing settings for the Ultrafuse 316L.

The 17-4 PH samples were printed and sintered at an outsourcing facility utilizing a Metal X printer and Markforged’s printing settings. Eiger, a proprietary software, designs the part size and the entire ADAM process parameters, including the support structure, automatically. Eiger is a CAM (Computer Aided Manufacturing) program that controls the entire manufacturing process, from design through sintering. The user’s access to the software has been disabled. As a result, except for the layer thickness and building direction, the process parameters are unknown and cannot be changed by the user.

Samples were examined in both a flat and upright configuration. According to Galati and Minetola [30], Markforged’s deposition approach contains one outside contour and three inside contours (Appendix C). The bottom and top layers are printed with full density, just like in normal FFF systems, while the technique for the other layers is determined by the layer thickness. A full-density technique is employed for layer thicknesses of 0.050 mm, while a closed triangular cell path is

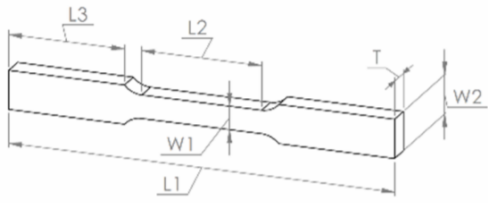
used to infill the section for layer thicknesses of 0.125 mm.

Scanning Electron Microscopy (SEM) was used to examine the Ultrafuse 316L filament and all of the printed green pieces using a Zeiss SEM EVO. Tescan used a MIRA3 to evaluate the sintered pieces. Before SEM analysis, all polymer-containing samples were gold sputtered. To evaluate the sintered parts' mesostructure, the software Image J was utilized to analyze SEM images. To accommodate for sintering shrinkage, the green sections were oversized according to ASTM D638 and E8 (Tables 4.2 and 4.3). All tensile tests were performed at 1 mm/min with a load cell of 100 kN on an Instron 5982 by Instron (Instron, Milan, Italy) (Appendix C).



Symbols	Standard Dimensions (mm)	Green Part Dimensions (mm)
L1	115.00	137.98
L2	33.00	39.59
L3	19.44	23.32
W1	6.00	7.20
W2	19.00	22.80
T	3.00	3.78

Table 4.2: Standard (ASTM D638) and Green part dimensions for Ultrafuse 316L samples.



Symbols	Standard Dimensions (mm)
L1	100.00
L2	32.00
L3	30.00
W1	6.00
W2	10.00
T	6.00

Table 4.3: Standard (ASTM D638) and Green part dimensions for Ultrafuse 316L samples.

First, a detailed examination of the filament and green produced components is provided. The sintered pieces are next examined, with an emphasis on the mesostructure formed during sintering and a relationship between the mechanical characteristics and the structure.

Filament

Under the microscope, the Ultrafuse 316L filament was broken and studied. The filament had a layered structure with an exterior polymeric covering layer (Figure 4.2a) that allowed it to be knotted without breaking (Figure 4.3). Metal particles with diameters ranging from 10 to 1 μm are entirely incorporated in polymeric strands to form the interior structure (Figure 4.2b). A thick coating appeared to be applied on the metal particles.

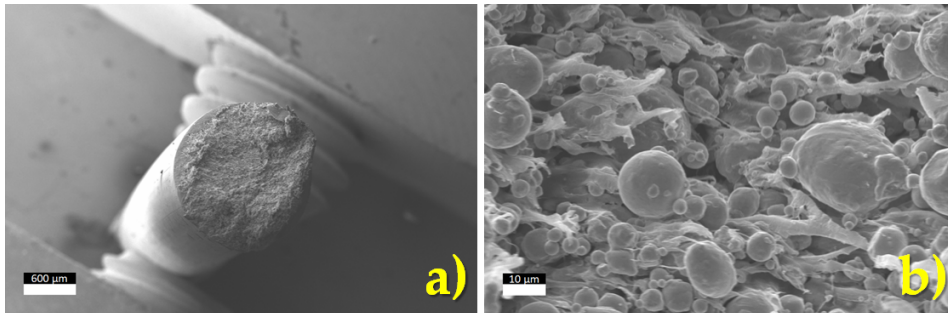


Figure 4.2: Cross section SEM analysis of the Ultrafuse 316L filament: (a) magnification 50; (b) magnification 2500.

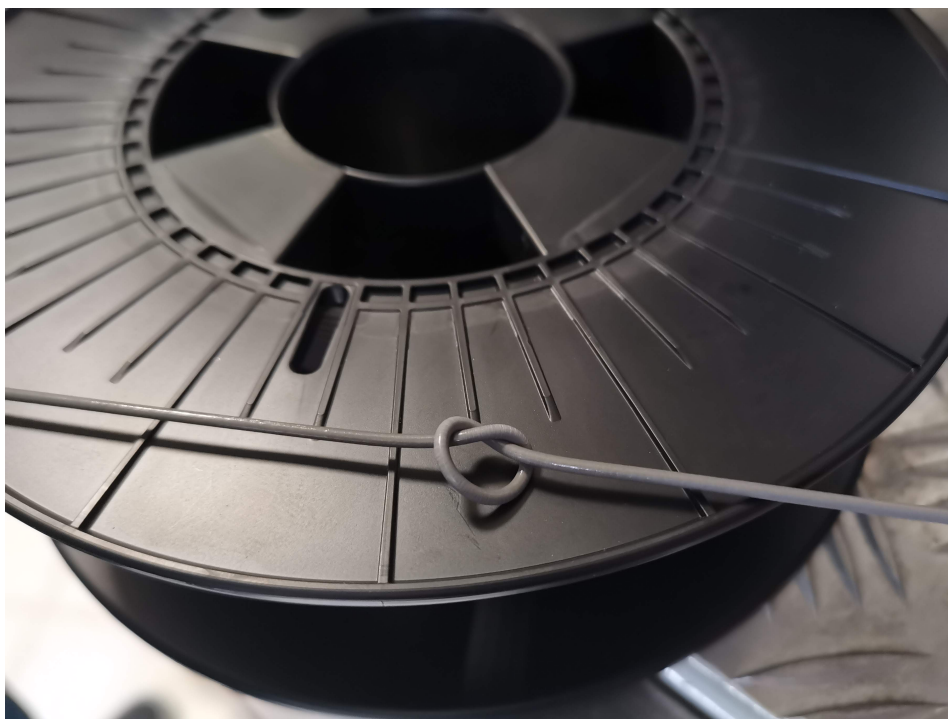


Figure 4.3: Knotted filament of Ultrafuse 316L.

Green parts

The 316L green components were printed with a density of 100 percent infill. However, due to imperfect fusing, certain gaps remained between the deposited rasters (Figure 4.4a). As a result of the polymer matrix melting and diffusion during the printing stage, the polymeric strands clearly visible in the neat filament (Figure 4.2b) were not evident in the printed specimens (Figure 4.4b). However, as can be seen when looking at the contour side of the green samples, the coated layer was still there (Figure 4.4c,d).

The resulting mesostructure is similar to that seen in normal FFF samples, and the part's consistency is based on the bonding between each raster caused by the

melting of the exterior coating and inside polymeric strands. The same investigations were done on the 17-4 PH green printed sample utilizing Markforged's ADAM process for comparison purposes. The rasters appeared more compressed and had a larger interdiffusion in this example (Figure 4.5a). The rasters, on the other hand, were dry, with no visible signs of a polymeric matrix between the particles, and had lower diameters (5–0.5 μm) than the Ultrafuse 316L system (Figure 4.5)

The 17-4 PH green samples were too brittle to carry out any reliable mechanical characterization or even handling as a result of this mesostructure. The Ultrafuse 316L green parts, on the other hand, were simple to work with.

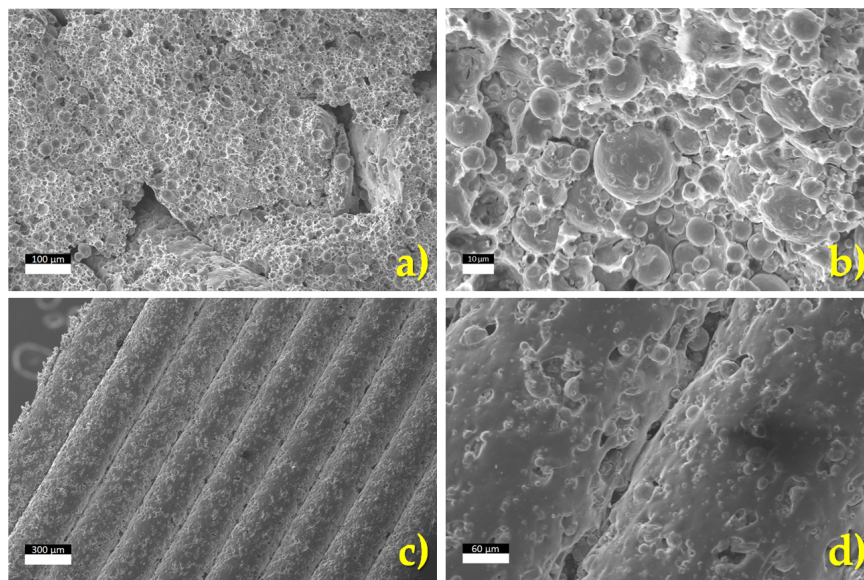


Figure 4.4: SEM images of the mesostructure for the green printed parts using Ultrafuse 316L: (a) cross section (magnification 300); (b) cross section (magnification 2000); (c) contour (magnification 500); (d) contour (magnification 100).

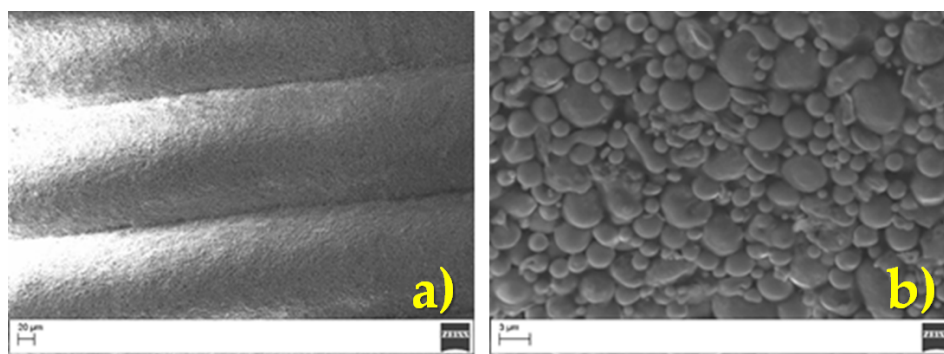


Figure 4.5: SEM Images of the mesostructure for the green printed parts using the 17-4 PH system by Markforged: (a) contour (magnification 500); (b) contour (magnification 6000).

Sintered parts

The removal of the polymeric binder during the debinding/sintering cycles for the MIM technology is required for the usage of hybrid polymer/metal for 3D printing metal. The shrinking of the portion was caused by the loss of the polymer and the sintering of the particles. Figure 4.6 shows some examples of sintered parts.



Figure 4.6: Optical image of the sintered 316L samples.

The 3D printed items must be oversized to account for the dimensional fluctuations that occur throughout the process. As a result, comparing the dimensions of the component before and after sintering is critical for determining the optimal part design. The measured values for the green and sintered parts for the build orientations utilized are reported in Table 4.4. In the XY plane, the flatwise specimens revealed a linear shrinkage of about 20%, whereas higher values (i.e. 25.20%) were measured in the Z direction perpendicular to the layer direction. Anisotropic behavior was higher in the upright samples, with values ranging from 8.57 percent to 20.70 percent.

During the sintering process, the effect of gravity on the metal component controls the anisotropic behavior. Kurose et al. [52] found that linear shrinkage varied between 14 and 23 percent depending on the building orientation. Gong et al. [36] reported similar shrinkage values, although they also noted that lower-height features decreased less than higher-height features. When compared to the shrinkage parameters announced by BASF in their guidelines, the values measured in this work deviate. The green components' mesostructure, as illustrated in Figure 4.4, was not totally dense, which could explain the difference.

The 17-4 PH samples could not be tested in the same way since they were printed

with proprietary settings and delivered sintered..

Build Orientation	Printing Axis	Measure	Green Part (mm)	Sintering Axis	Sintered Part (mm)	Shrinkage (%)
Flatwise	Y	L	22.80	Y	19.04	19.73
	Z	W	3.78	Z	3.02	25.20
	X	T	137.98	X	115.25	19.72
Upright	X	L	22.80	Y	19.35	17.81
	Y	W	3.78	Z	3.48	8.57
	Z	T	137.98	X	114.31	20.70

Table 4.4: Standard (ASTM D638) and Green part dimensions for Ultrafuse 316L samples.

Tensile testing was performed on the sintered samples. Figure 4.7 shows exemplary curves for samples printed with the Ultrafuse 316L and the Markforged 17-4 PH. The stress is measured by dividing the load by the nominal area Width*Thickness (Tables 4.2 and 4.3). When compared to the 17-4 PH samples, the 316 L samples had higher strain at break values (43%) than the 17-4 PH samples (below 1 percent). Table [tab:316l tab5] summarizes the tensile characteristics measured for sintered 316L and 17-4 PH. For comparison, the characteristics declared by the filaments' producers are also reported.

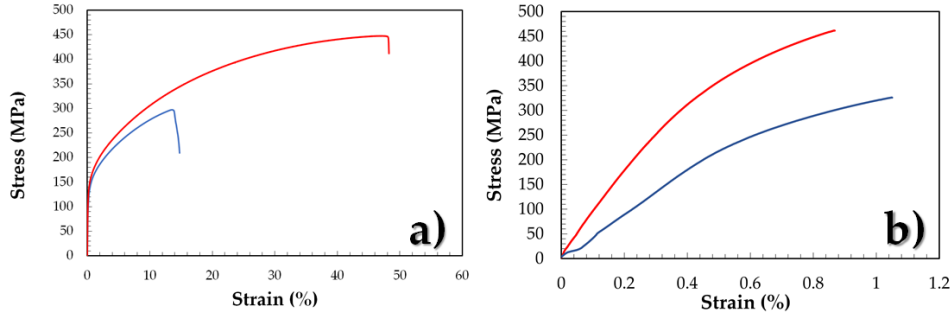


Figure 4.7: Tensile stress–strain curves for the sintered parts: (a) Ultrafuse 316L and (b) Markforged 17-4 PH. (Flat: red; upright: blue).

Material	Building Orientation	Yield Strength MPa	Tensile Strength MPa	Tensile Modulus GPa	Strain at Break %
316L	Flatwise	148.01 ± 4.50	443.90 ± 5.87	157.24 ± 4.50	43.33 ± 2.53
	Upright	113.75 ± 13.42	206.27 ± 80.11	117.31 ± 1.94	13.35 ± 6.59
17-4 PH	Flatwise	443.00 ± 6.90	497.40 ± 9.90	108.00 ± 6.90	0.79 ± 0.05
	Upright	412.00 ± 31.60	494.70 ± 29.70	102.8 ± 1.20	0.95 ± 0.14
316L *	Flatwise	251	561	-	53
	Upright	234	521	-	36
17-4 PH *	Flatwise	1100	1250	170	6
17-4 PH **	-	660	1042	195	8.5

Table 4.5: Tensile properties for the sintered parts produced in this paper. The properties reported in the technical data sheet of the producer are reported for comparison. *The data were extracted from the technical data sheet (TDS) released by the producer (BASF for the 316L and Markforged for the 17-4 PH). **The data were extracted from the technical data sheet released by Desktop Metal with their Studio System™.

The measured characteristics for the 17-4 PH samples are lower than those provided by Markforged, as shown in Table 4.5. These specimens, on the other hand, had a closed triangular cell infill [30], resulting in a smaller load bearing surface (Figure 4.8). The cross-section area was determined to be 20.89 mm² using Image J, rather than the 36 mm² calculated using the external sides of the cross section. The tensile characteristics were greater and closer to those stated by Markforged when the true load bearing area (20.89 mm²) was taken into account (Table 4.6).

Desktop Metal has also released some values for its 17-4 PH system (Table 4.5) that are in the middle of the values found in this article and Markforged's declarations. Gonzales-Gutierrez et al. [39] reported a tensile modulus between 174 GPa and 208 GPa for their lab-made filament filled with 55 v% of 17-4 PH metal particles and printed with a 100 percent infill density in the open literature, while the maximum stress ranged from 660 MPa to 729 MPa. The presence of imperfections in the specimens' structure was interpreted as the cause of the wide range of mechanical properties found.

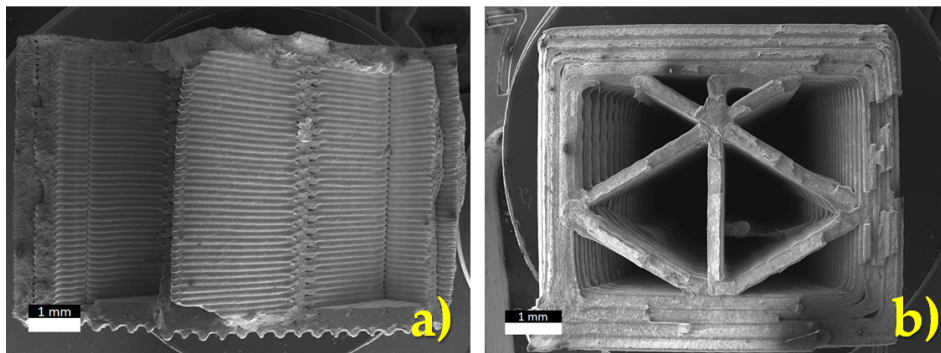


Figure 4.8: Morphology of the fracture surface of the fractured specimens manufactured using 17-4 PH: (a) flatwise; (b) upright.

The cracked surface of the 17-4 PH samples studied in this work revealed two types of defects: pores between the raster (Figure 4.9a) and inclusions (Figure 4.9b). The inclusions may also be seen on the raster's surface (Figure 4.10). The presence of a greater carbon concentration on the raster's surface was revealed by EDX analysis (Figure 4.11), leading to the conclusion that the surface may be rich in carbon-based polymeric binder residues. The lower mechanical characteristics reported in our samples could be due to the presence of these flaws and greater carbon concentrations.

It's also worth noting that the upright samples had a higher level of variability in the test data, as evidenced by the large standard deviation. When comparing flat versus upright printed samples, similar trends were observed for standard FFF [69], which was explained as the result of the interlayer bonding strength's influence. The existence of an interlayer fracture in the 17-4 PH upright-printed samples confirmed that this building orientation is the worst in terms of mechanical resistance.

Property	Units	Calculated Value
Yield Strength	[MPa]	839.47
Tensile Strength	[MPa]	942.56
Tensile Modulus	[GPa]	204.66

Table 4.6: Tensile properties for the 17-4 PH upright sample corrected to account for the real load bearing area.

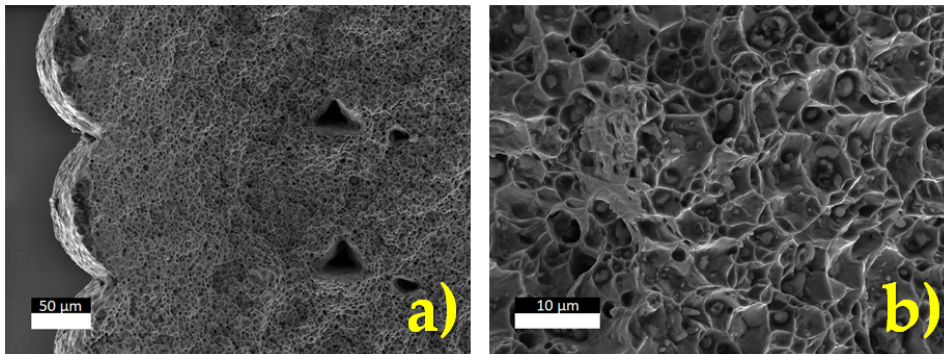


Figure 4.9: Defects observed in the cross section of a flatwise sample of 17-4 PH: (a) porosity between the raster; (b) details of particle inclusions.

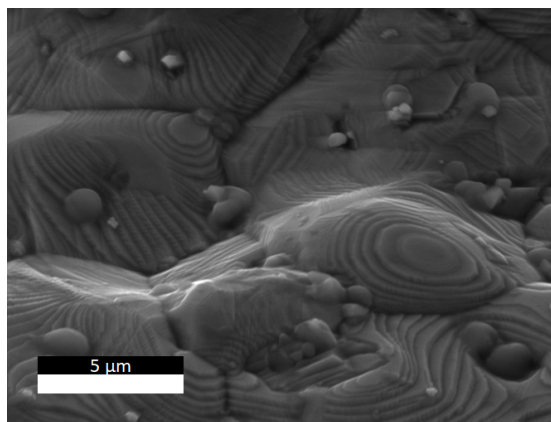


Figure 4.10: Inclusions observed on the raster's surface of an upright sample printed with 17-4 PH.

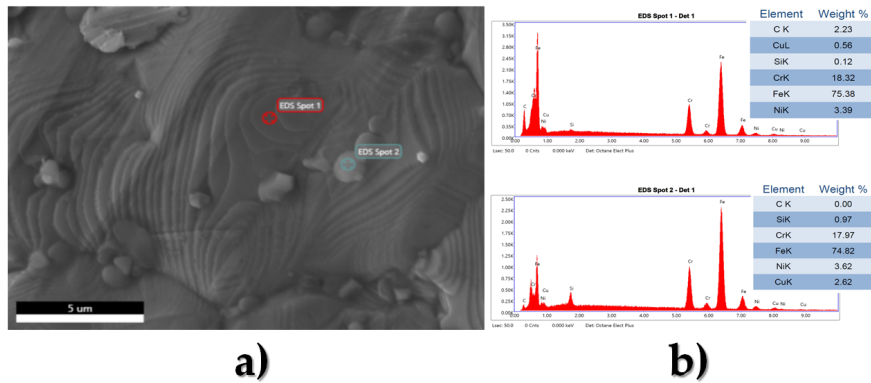


Figure 4.11: EDX spectra for the raster's surface and an inclusion observed for the 17-4 PH samples.

The tensile characteristics of the 316L samples were similar to those reported by BASF, however they were lower. These samples' cross sections were described. Despite the whole sintering cycle, the mesostructure of the flatwise sample revealed the presence of micro porosity between the rasters (Figure 4.12a). This porosity appears to be the outcome of the imperfect raster fusion seen in the green area (Figure 4.4). The upright sample revealed much larger pores and, similar to the 17-4 PH, an interlayer fracture (Figure 4.12b).

The flatwise sample's porosity was determined to be 9.76 percent using Image J, resulting in an estimated true load bearing area of 17.07 mm² rather than the observed 18.91 mm². The tensile modulus, yield strength, and tensile strength were estimated with the true load bearing area to be 174.15 GPa, 163.93 MPa, and 491.65 MPa, respectively. Despite the area correction, the measured values were still lower than BASF's estimates. This is due to the porosity, which may function as a stress intensifier, causing premature failure. When comparing FFF to injection molded counterparts, similar mechanical performance decreases were seen [19, 86, 88]. In comparison to the flatwise samples, the upright samples had poorer mechanical resistance due to increased porosity and a building orientation that resulted in excessive loading of the interlayer region. Higher standard deviations were seen for the upright building orientation in the 17-4 PH samples.

Comparison with Standard Metal AM Technologies

FFF has been created as a simple, safe, and low-cost alternative to typical AM metal processes for printing metal samples. Mechanical performance, on the other hand, is crucial. The mechanical characteristics of 316 L and 17-4 PH treated by ordinary metal AM and without thermal post-processing are summarized in Table 4.7. The mechanical properties obtained with MIM were also presented for comparison. In comparison to equivalent components made by normal metal AM, the specimens produced by FFF (Table 4.5) had overall worse mechanical characteristics. The FFF

made specimens for the 316L showed attributes in the same MIM range as the MIM manufactured specimens.

When the real cross section areas (Table 4.6) were used instead of the nominal areas, a similar result was achieved for 17-4 PH. As a result, when compared to MIM parts, FFF parts made with hybrid metal/polymer filaments are superior. To achieve the optimum results, however, intrinsic processing flaws such as voids and weak interlayer bonding (Figure 4.12) must be avoided. This can be accomplished by adjusting the print settings [35]. As a result, more research into printing optimization is needed to fully realize the promise of FFF applied to hybrid metal/polymer.

In addition to conventional tensile testing, it will be essential to describe the effect of pre-crack on printed specimens in future study because this could have a significant impact on applications [50].

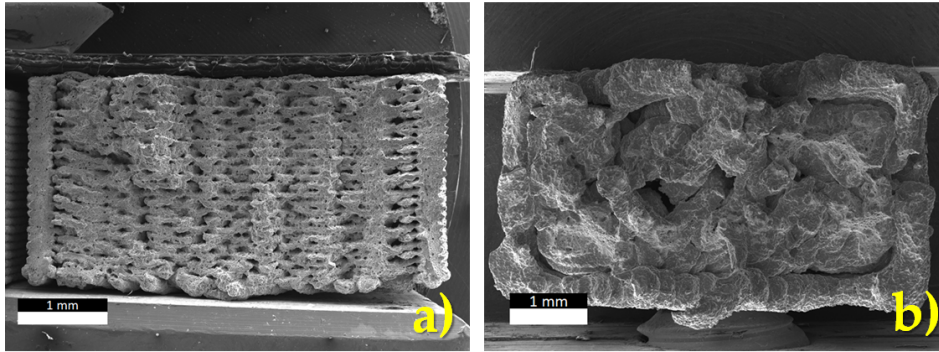


Figure 4.12: Morphology of the fracture surface of the fractured specimen manufactured using Ultrafuse 316L: (a) flatwise; (b) upright.

When comparing FFF of hybrid metal/polymer AM to regular metal AM, economic aspects must be considered in addition to mechanical performance. The manufacture of an injection molding mold (Figure 4.13 and 4.14) was used as a comparison part to compare the Ultrafuse 316L with the production of SSL316L utilizing an SLM EOS400m printer. Ruffo et al. [76] provided a cost model, which was applied in this study. Table 4.8 shows the results of cost simulations. For the Ultrafuse 316L and the SSL316L, the material costs were considered to be 129 EUR/kg and 30 EUR/kg, respectively.

Because the recycling proportion (95%) for SLM operating only to print this mold creates a large waste of unused and non-recyclable powder, the cost simulation returned a higher value for SLM (EUR 330.13) than FFF (EUR 100.62). The other cost that had a major impact on the final part price was machine utilization (18.3 percent) as a result of the EOS M400's high investment cost (about 1.7 million). The final estimated cost of printing the mold with FFF and the Ultrafuse 316L was EUR 246.13, compared to EUR 1147.88 for SLM.

This was the expense of the green component in the instance of the FFF. To

this, the cost of sintering must be added, which is currently charged at roughly 60 EUR/kg by Elnik, BASF’s chosen partner. Furthermore, when the cost of sintering is factored in, the ultimate cost is still significantly lower than the predicted cost of SLM.

Material	Technique	YS [MPa]	TS [MPa]	TM [GPa]	Sb [%]	Ref.
316L	DMLS (flat)	535	650	-	35	[23]
	DMLS (upright)	490	590	-	45	
	SLM	319.8	574.3	179.65	49.6	[25]
	SLM	517	687	169-212	25-32	[53]
	MIM	175	517	190	50	[68]
	EBM (flat)	545	655	182	44	[33]
	EBM (upright)	480	595	150	50	
17-4 PH	DMLS (flat)	860	886	-	19.9	[23]
	DMLS (upright)	861	924	-	20.1	
	EBM (flat)	850	1020	180	16.6	[32]
	EBM (upright)	835	975	178	15.2	
	MIM	896	730	190	6	

Table 4.7: Mechanical properties for 316L and 17-4 PH processed by different technologies. DMLS: Direct Metal Laser Melting; SLM: Selective Laser Melting; MIM: Metal Injection Molding, EBM: Electron Beam Melting. YS: Yield Strength; TS: Tensile Strength; TM: Tensile Modulus; Sb: Strain at Break.

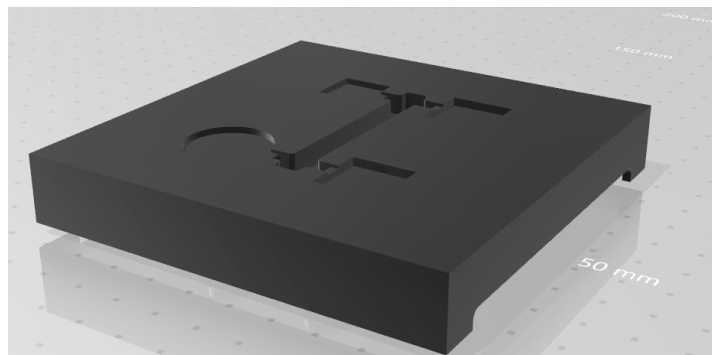


Figure 4.13: Mold geometry used for cost comparison.

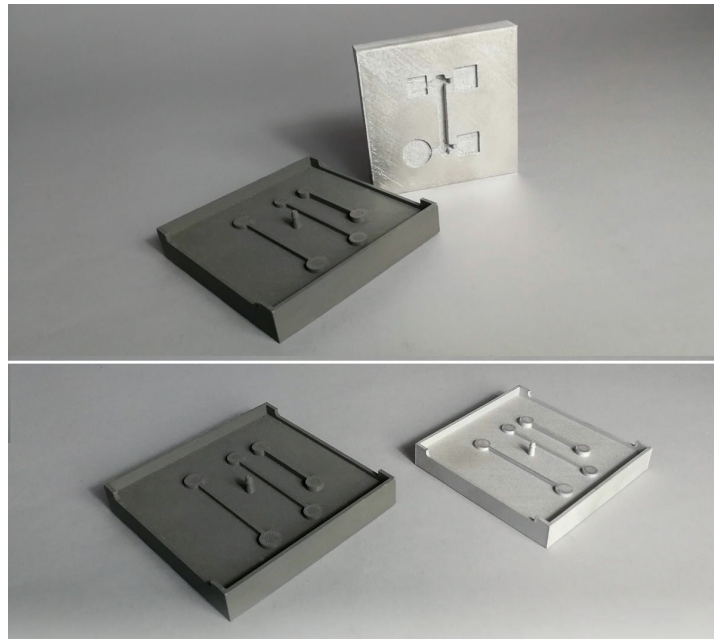


Figure 4.14: Green and sintered molds.

	Ultrafuse 316L		SLM 316L	
	%	EUR	%	EUR
Material	40.9	100.62	28.8	330.13
Build prep	28.4	70.00	18.3	210.00
Machine usage	0.5	1.25	37.3	428.47
Build consumables	0.2	0.58	5.1	59.02
Labor	23.8	58.68	6.6	75.26
Post-process	6.1	15.00	3.9	45.00
Total cost		246.13		1147.88

Table 4.8: Cost modelling comparison for the sample mold produced by 316L: Fused Filament Fabrication (FFF) vs. SLM.

4.2 Stainless steel 17-4 PH

The work of analyzing and comparing the filaments loaded with metal particles has continued and is continuing towards other loaded filaments. In fact, there may be different fillers with which to fill the FFF thermoplastic filaments (i.e. 17-4 PH, H13, Alumina and Zirconia). The briefly exposed works refer to BASF's Ultrafuse 17-4 PH filament.

The influence of printing settings on producing good green parts and improving the mechanical properties of final 17-4 PH metallic parts were investigated in this study. The tensile test ASTM E8 was used to determine the mechanical characteristics of the final metal parts. Density data were also taken into consideration while

measuring the influence on shrinkage.

BASF’s Ultrafuse 17-4 PH filament was used in this work. This filament is made up of a metal–polymer combination with a nonslip surface that may be used in any Bowden or direct drive extruder. In this study, we employed an Ultimaker S5 desktop 3D printer with a printcore CC red 0.6 and an artificial ruby at the nozzle tip, which was specially designed to print with composite and abrasive filaments (Figure 4.15). BASF set the printing conditions in their Cura plugin for the slicing software. The printing profiles, according to the manufacturer, were created to give quality, flexibility, and reliability for the wide range of parts and applications made feasible by Ultrafuse 17-4PH. These ready-to-use profiles are a good starting point for beginning users, but they don’t include explicit references to the mechanical properties of the final metal pieces. The printing parameters are listed in the table. As recommended by BASF, the postprocessing of the 3D printed samples was outsourced to a debinding and sintering service.

Parameters	Printing profiles			
	Fast	Quality	Strong	Lightweight
Layer height [mm]	0.2	0.1	0.15	0.15
Infill line width [mm]	0.6	0.6	0.6	0.72
Wall line count [-]	2	3	2	3
Top/bottom layers [-]	1	1	1	10
Infill density [%]	105	105	105	60
Printing temperature [°C]	240	240	245	245
Wall flow [%]	95	100	100	100
Top/bottom flow [%]	95	105	105	105
Infill flow [%]	95	100	100	100
Print speed [mm/s]	30	25	25	25

Table 4.9: Printing parameters for Ultrafuse 17-4 PH.

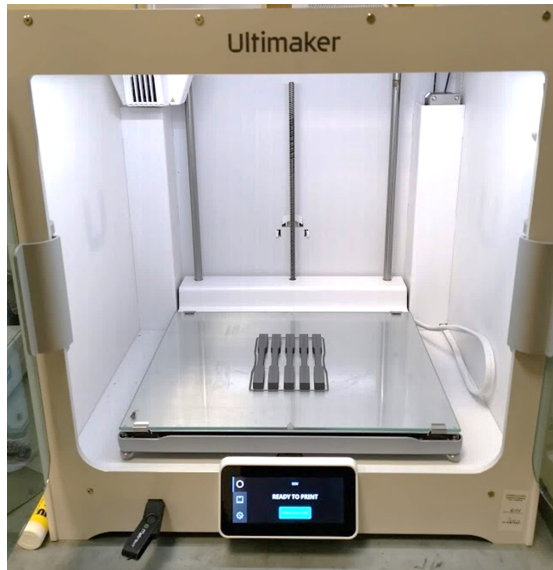


Figure 4.15: Tensile test samples printed on Ultimaker S5.

The actual shrinkages after D&S were calculated according to Equation 4.1:

$$S = 1 - \frac{L_s}{L_g} \quad (4.1)$$

where S is the shrinkage suffered by the specimen, L_s and L_g are the dimension of the sintered and green parts under consideration (Figure 4.16), respectively. All printing configurations display a shrinkage between 17 % and 20%. The shrinkage observed does not differ much from the theoretical shrinkages expected in the slicing step at the time of choosing the oversizing factor (OFS) which can be calculated according to Equation 4.2:

$$OFS = \frac{1}{1 - S} = \frac{L_g}{L_s} \quad (4.2)$$

Indeed, the OFS values of the present work were set equal to 20 % on the xy plane and to 26% on the z axis, and they correspond to an expected theoretical shrinkages values of 17 % on the xy plane and of 20 % on the z axis.

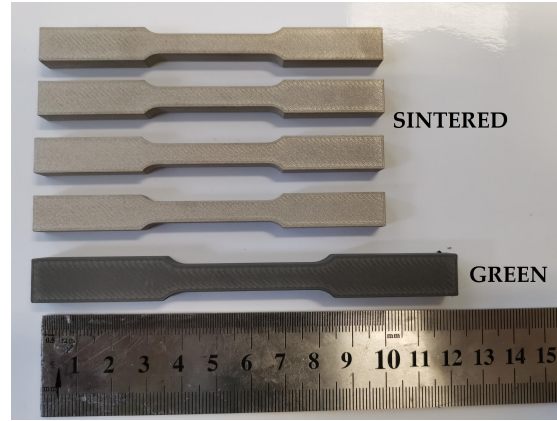


Figure 4.16: Green and sintered parts of one printing profile (printing profile strong).

Considering that the metal FFF sintered specimens are characterized by the presence of porosity into the internal structure, the bulk densities, ρ_b , of cube shaped samples printed by the investigated printing profiles were compared with the density of monolithic stainless steel 17-4 PH ($\rho_{17-4PH}=7750 \text{ kg/m}^3$) to evaluate samples porosity, p , according to Equation 4.3:

$$p = \left(1 - \frac{\rho_b}{\rho_{17-4PH}}\right) \cdot 100 \quad (4.3)$$

The samples were weighed in air and then again in the auxiliary liquid (water, in our study) with a known density. The bulk density of the sintered parts, ρ_b , was calculated according to Equation 4.4 after weighting the cube samples in air and in an auxiliary liquid, i.e. water, with a known density:

$$\rho_b = \frac{w_{air}}{w_{air} - w_{liq}}(\rho_0 - \rho_L) + \rho_L \quad (4.4)$$

where ρ_b is the density of the sample, w_{air} is the weight of the sample in air, w_{liq} is the weight of the sample in the auxiliary liquid, ρ_L is the density of the auxiliary liquid and ρ_0 is the density of air. The average densities and the average porosity of the sintered samples for each printing configuration are reported in Table 4.10.

Printing profiles	Density [kg/m^3]	Porosity [%]
Fast	7128	8.03
Quality	7465	3.68
Strong	7395	4.58
Lightweight	6375	17.74

Table 4.10: Density and porosity of sintered parts.

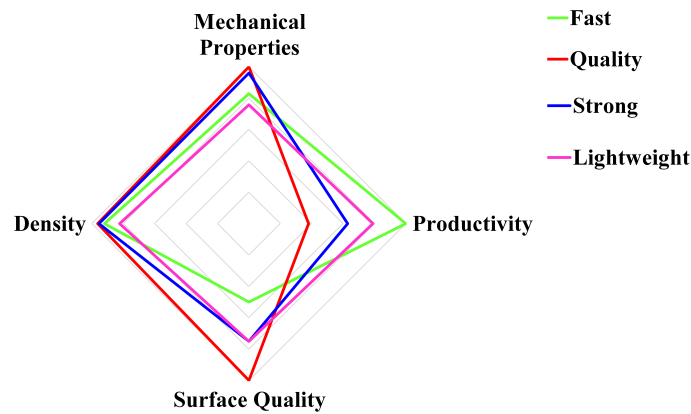


Figure 4.17: Radar chart for 17-4 PH sintered tensile samples.

The mechanical tests conducted, the values of which will be published in a scientific journal, confirmed the influence of the printing parameters on the observed mechanical properties (tensile strength and elongation at break). In summary, to help the user of slicing software such as Cura by Ultimaker, supplied with the BASF plugin for FFF metal printing, a radar chart has been developed summarizing the characteristics of each printing profile (Figure 4.17).

Therefore, it was possible to deduce that for high mechanical performance the most suitable profiles are Quality and Strong. The latter profile can be preferred to the first if we want to increase productivity by about 50%, at the expense of surface quality. On the other hand, if we want to increase productivity without sacrificing too much the mechanical performance, the most suitable profile is Fast.

Furthermore, this study was extended with measurements of thermal conductivity associated with the degree of internal porosity of the printed samples. The findings of this study will be published in a scientific journal soon.

Conclusions

The present PhD thesis addressed several topics ranging from material development to its characterization and to the development of AM technology for its use in composite manufacturing. To support the full understanding of the mechanical behavior of the materials developed the testing methodologies were analyzed using design of experiments (DoE). The mechanical testing was not limited to the simple use of ASTM standards used for tensile and flexural testing of plastics processed by injection molding. To measure the interlaminar bonding resistance the ASTM standard D2344M, typically used for FRP, was analyzed, and compared to standard flexural testing. This approach allowed to highlight some rules helpful to understand how materials behave when printed. These findings were useful when testing the carbon fiber reinforced filaments analyzed during the thesis as described in chapter 1. In the same chapter 1 filaments containing 30wt% of short recycled carbon fibers were presented. The production of this type of filaments is relevant as the commercial filaments available on the market are usually limited to a fiber content of 20wt%. The effects of the higher fiber content are clearly observed in terms of the mechanical properties which are higher of 47% and 7% for the tensile modulus and stress than those observed for similar commercial filaments. In the same chapter a full characterization of interlaminar and impact properties for commercial CF reinforced filaments was reported. The findings revealed that proper slicing design is critical for enhanced delamination and impact performance of the printed part. In fact, it was observed that the raster angle is a significant printing parameter, exhibiting increases in the reported response of 30-40% and 14-25% for ILSS and absorbed energy, respectively.

These findings are particularly helpful to drive the innovation in the field of the fiber reinforced FDM materials and to get a better picture of the potential applications envisaged for these materials. Some examples of applications could range from load-bearing structures for drones to self-standing molds for fiber reinforced polymers manufacturing. The future challenge will be to find strategies to increase further the fiber content to reach a value of fiber volume content of about 50-65v%.

In chapter 2, three types of tests were performed: tensile, bending and short beam strength in line with the approach followed in the first chapter. Of the three investigated tests, only the short beam shear test was able to sufficiently discriminate between the types of material confirming that using SBS can unveil the bonding strength helping to drive printing optimization. This result strictly depends on the test configuration that favors the effect of the internal shear stress in the specimen under load conditions, and on the key role played by the interlaminar bond in the mechanical properties of the FDM molded parts. More research is needed to address the correlation between printing parameters and the mechanical properties of printed materials. Such research is essential, given the increasing need for FDM parts not only prototype but also structural (fiber-reinforced materials) which are all characterized by a strong anisotropy. For this reason, other types of mechanical tests such as the Double Cantilever Beam Test (DCB) or End Notch Bending Test (ENF) may also be useful in order to design specific standards. A fundamental aspect is the construction procedure (orientation of the part, orientation of the rasters, the various infill parameters, etc.). In terms of future applications, properly developed test methods would allow for useful data sets for simple design of available parts. In addition, standardized testing is required to have robust techniques for validating materials for FDM under development.

In chapter 3 different manufacturing approaches for producing composite hollow parts have been discussed. Starting from the industrial need of ACS, the industrial partner of the AMA PhD industrial project, to produce a certain number of hollow composite components, two types of approaches were compared, one based on the use of standard CNC machined mold and one based on AM-based tooling. The development of AM tooling was deeply investigated using and comparing the use of FDM printed mandrels and LCD printed mandrels. Time and cost analysis revealed that the additional cost of printing 40 mandrels was balanced by the time savings for autoclave processing, finishing and mandrel dissolution. For some shapes studied (e.g. a handlebar bike) differences were observed for the lay-up time. The latter, i.e. lay-up time, impacted more on this kind of shapes and less on the small components. In fact, AM mandrels simplify the lamination procedure allowing the operator to have a defined and stiff shape, which is close to the final one, onto which lay down the prepreg also applying the needed compaction pressure to obtain a the near to net shape ready for bagging and autoclaving. The same easy of lay-up is not achieved with a metal mold resulting in time processing increases that, in turn, lead to higher production costs for traditional approach with CNC moulds.

In the same chapter, the novel solution based on the use of LCD to print easy break away mandrel it has been demonstrated. LCD can be advantageous both in terms of removal time and of the final cost for the mandrel itself. The materials used for the LCD printing are photo-curable resins that can be tailored, as it was demonstrated

in the thesis, to improve the thermal resistance of these resins to allow their use with high-temperature prepregs or to match the coefficient of thermal expansion of composites. In terms of recycling, it is necessary to conduct further research to exploit the use of a new recyclable epoxy resin as vitrimers or to use cleavable amines that can be recycled at the end of their life.

In Chapter 3 also daylight curable (meth)acrylate-epoxy blends were studied. It was observed that by thermally treating daylight resins printed with LCD their glass transition temperature rose from 45 to 137 °C. The thermal cycle carried out to obtain this increase in T_g is about 4 h and 20 min. This additional processing time does not have a dramatic impact on the overall production time because the LC-HR2 printer can print 100 microns every 25s thus leading to a print time of 7h for a complex part with a volume of 78 cm³ (B). With regards to the productivity level, LCD printing is favored over other AM techniques by the fact that only up and down platform movements is present while, with other AM approaches, printing head and platform movements are present resulting in a different printing time scale. The differences are particularly stressed when more than one part is to be printed for serial production of many mandrels on the platform. In the chapter it was shown that printing time can be reduced by considering printers with larger screens (e.g. the LC-Magna or the LC-Maximus, having screens of 24 "and 40" respectively). Printing multiple mandrels at the same time heat post-treatment can be performed simultaneously on several parts, making this further step little influence in terms of processing time compared to the number of parts made. The advantage of thermal post-curing was also investigated on further improved systems when DGEBA/DETDA resin was added to the base formulation. In particular, an increase in T_g was noted up to 165 and 174 °C for mixtures with 30 and 50% by weight of DGEBA/DETDA, respectively. However, these notable increases in T_g have shown some drawbacks due to the increasing photopolymerization times to obtain a good quality LCD print. The exposure time had to be adjusted from 25s for the cream resin to 30s for epoxy-based blends and the platform had to be moved higher and slower to allow for resin flow. The changes in these printing parameters lead to longer printing time. For example, the part (B) with a volume of 78 cm³ would be of 16 h of printing time.

The results shown on epoxy-blends offer some important insights for the further development of such systems. Addition of photoinitiators could be considered to counteract the reduced photo-curing reactivity of the modified blends, while the viscosity of the blend could be adapted by using reactive diluents. As has been shown in the chapter 3, such developments may be interesting for future applications in the field of tools for polymers and composites or for specific applications in harsh environments. The high processing temperatures in the field of composites, in fact, require resistant materials for these processes. Other fields that could benefit from the use of high T_g resins and the high resolution offered by LCD printing are valves

that work with hot fluids. Similar applications for dual-cure epoxies have been presented by Carbon3D but, according to the results obtained from the research shown, LCD printing can also be used if the epoxy mixing approach is pursued.

Finally, in the Chapter 4 the results of printing and characterization of metal parts by FFF were shown. The technique used did not require the use of expensive machines and equipment for traditional metal handling and printing. The morphological analysis by SEM and EDX was carried out on both the green and the sintered parts and showed the presence of air gaps and a weak interlayer bonding characteristic of the FFF materials. The presence of these defects is the cause of the reduction of the mechanical properties observed in the sintered parts compared to those declared by the manufacturer. That said, the metal parts obtained show the same mechanical behaviour as those obtained by MIM.

These results show that there is still a gap between the standard metal AM and the one presented there. In fact, research is continuing on the optimizing printing parameters, also in agreement with BASF, in order to rationalize the use of these materials within a shared database (i.e. plugin in Cura slicing software). In the next published works will be shown, in particular, the printing optimization works of metal parts in 316L on the FFF desktop printer and the mechanical characterization of printing profiles to obtain metal parts in 17-4 PH. Therefore, after careful work of choosing the most influential printing parameters and optimization by means of statistical techniques (DoE), it is possible to increase the mechanical properties of the sintered parts.

In addition, the economic advantages of the metal FFF technique were also analyzed, taking into consideration a printed demonstrator, i.e. a mould for injection moulding. The cost-effectiveness of the metal FFF technique compared to the traditional SLM was demonstrated through the application of cost modelling. In the comparison made, the environmental impact of the two processes was not taken into consideration. In fact, based on which AM process is chosen, the environmental impact changes accordingly. In this sense, the SLM process compared to the FFF process that uses small desktop printers, has higher energy consumption. The FFF process, therefore, is proving to be a valid support for processes that do not require excessive mechanical efforts compared to traditional metals (i.e. moulds, metal inserts, various tools), precisely because of its cost-effectiveness, simplicity and safety in use.

However, much research still needs to be done on the limitation and prediction of shrinkages to optimize the dimensional control of the manufactured parts. The technology analyzed is promising if we consider that the investment cost are very limited making this approach accessible to the users which can find in simple machines like the Ultimaker S5 used in our thesis the perfect companion for supporting composites processing both in terms of tooling and inserts making. Once the technology is

further optimized the same approach could be expanded using large area printers.

Dissemination activity results

Awards

1. Winning PhD project at the SAMPE Students Selection 2021 for participating and represent SAMPE Italy at the SAMPE Europe Conference in Zurich on 29-30 September 2021.
2. Participation Grant at XLII National Conference on Calorimetry, Thermal Analysis and Applied Thermodynamics, January 27 - 28 2021 Online, Udine.
3. Best Poster Award at V International Congress Central and Eastern European Conference on Thermal Analysis and Calorimetry jointly with the 14th Mediterranean Conference on Thermal Analysis and Calorimetry - 2019 Rome.

Indexed papers

1. C. Tosto, F. Miani, G. Cicala. Study of several printing profiles in Fused Filament Fabrication printing of polymeric filaments loaded with 17-4 PH metal particles. *(to be submitted)*
2. G. Cicala, C. Tosto, E. Pegolizzi, L. Vitiello, G. Filippone. Production of PLA-Milled Carbon Fibers (MCF) filled filaments for Fused Filament Fabrication (FFF) printing. *(submitted)*
3. C. Tosto, E. Pegolizzi, G. Cicala. Comparison of three Additive Manufacturing (AM) techniques for manufacturing complex hollow composite parts. *(submitted)*
4. C. Tosto, G. Cicala, J. Tirillò, F. Sarasini, C. Sergi. Optimization of fused deposition modeling process parameters for cost-effective printing of metal parts. *(submitted)*
5. N. Cennamo, L. Saitta, C. Tosto, F. Arcadio, L. Zeni, M.E. Fragalà, G. Cicala. Microstructured Surface Plasmon Resonance Sensor Based on Inkjet 3D

- Printing Using Photocurable Resins with Tailored Refractive Index. *Polymers*, MDPI. *Polymers* 2021, 13, 2518. DOI:10.3390/polym13152518.
6. A. Patti, G. Cicala, C. Tosto, L. Saitta, D. Acierno. Characterization of 3D Printed Highly Filled Composite: Structure, Thermal Diffusivity and Dynamic-mechanical Analysis. *Chemical Engineering Transactions*, 86, 1537-1542. DOI:10.3303/CET2186257.
 7. La Rosa, A.; Greco, S.; Tosto, C.; Cicala, G. LCA and LCC of a chemical recycling process of waste CF-thermoset composites for the production of novel CF-thermoplastic composites. Open loop and closed loop scenarios, *Journal of Cleaner Production*. 2021, 304, 127158. DOI: 10.1016/j.jclepro.2021.127158.
 8. Tosto, C.; Tirillò, J.; Sarasini, F.; Cicala, G. Hybrid Metal/Polymer Filaments for Fused Filament Fabrication (FFF) to Print Metal Parts. *Appl. Sci.* 2021, 11, 1444. DOI: 10.3390/app11041444.
 9. Blanco, I.; Cicala, G.; Tosto, C.; Bottino, F.A. Kinetic Study of the Thermal and Thermo-Oxidative Degradations of Polystyrene Reinforced with Multiple-Cages POSS. *Polymers* 2020, 12, 2742. DOI: 10.3390/polym12112742.
 10. C. Tosto, L. Saitta, E. Pergolizzi, A. Patti, G. Celano, G. Cicala. Fused Deposition Modelling: New Standards for mechanical characterization. Special Issue of *Macromolecular Symposia Wiley-VCH*. 2021, 395, 2000253. DOI:10.1002/masy.202000253.
 11. G. Cicala, C.Tosto, G. Recca, A. Patti. Additive Manufacturing processing of plastics for mass production of composites tooling: technical and economic analysis. Special Issue of *Macromolecular Symposia Wiley-VCH*. 2021, 395, 2000256. DOI:10.1002/masy.202000256.
 12. L. Saitta, C. Tosto, E. Pergolizzi, A. Patti, G. Cicala. Liquid Crystal Display (LCD) Printing: A Novel System for Polymer Hybrids Printing. Special Issue of *Macromolecular Symposia Wiley-VCH*. 2021, 395, 2000254. DOI:10.1002/masy.202000254.
 13. Blanco, G. Cicala, C. Tosto, G. Recca, G. Dal Poggetto, M. Catauro. Kinetic study of the thermal dehydration of fly ash filled Geopolymers. Special Issue of *Macromolecular Symposia Wiley-VCH*. 2021, 395, 2000225. DOI:10.1002/masy.202000225.
 14. Patti, A.; Acierno, D.; Latteri, A.; Tosto, C.; Pergolizzi, E.; Recca, G.; Cristaudo, M.; Cicala, G. Influence of the Processing Conditions on the Mechanical Performance of Sustainable Bio-Based PLA Compounds. *Polymers* 2020, 12, 2197. DOI: 10.3390/polym12102197.
 15. C. Tosto, E. Pergolizzi, I. Blanco, A. Patti, P. Holt, S. Karmel, G. Cicala. Epoxy based blends for additive manufacturing by Liquid Crystal Display

(LCD) printing: the effect of blending and dual curing on daylight curable resins. *Polymers* 2020. DOI: 10.3390/polym12071594.

16. I. Blanco, F. Bottino, G. Cicala, G. Ognibene, C. Tosto. Design, preparation and thermal characterization of Polystyrene composites reinforced with novel three cages POSS molecules. *Molecules* 2020. DOI: 10.3390/molecules25132967.
17. C. Tosto, L. Saitta, E. Pergolizzi, I. Blanco, G. Celano, G. Cicala. Methods for the Characterization of Polyetherimide Based Materials Processed by Fused Deposition Modelling. *Appl. Sci.* 2020, 10, 3195. DOI: 10.3390/app10093195.
18. C. Tosto, A. Latteri, E. Pergolizzi, D. Giordano, G. Abramo, R. Catenaro, N. Pignotti, G. Cicala (2020) Additive Manufacturing of Plastics: an efficient approach for composites tooling - Macromolecular Symposia - Macromolecular Symposia Wiley-VCH. DOI: 10.1002/masy.201900069.

National and international conferences¹

1. G. Cicala, C. Tosto, E. Pegolizzi, L. Vitiello, G. Filippone. Production of PLA-Milled Carbon Fibers (MCF) filled filaments for Fused Filament Fabrication (FFF) printing. 5th International Conference POLCOM 24-27 November 2020, Bucharest.
2. **C. Tosto**, E. Pegolizzi, G. Cicala. Comparison of three Additive Manufacturing (AM) techniques for manufacturing complex hollow composite parts. 5th International Conference POLCOM 24-27 November 2020, Bucharest.
3. N. Cennamo, G. Cicala, L. Saitta, C. Tosto, F. Arcadio, L. Zeni, M.E. Fragalà. Surface Plasmon Resonance Sensor based on inkjet 3D printing. 2nd International Electronic Conference on Applied Sciences. *Applied Sciences*, MDPI. 15-31 October 2021, Online.
4. **C. Tosto**, G. Cicala. Composites tooling manufacturing from different AM techniques. SAMPE Europe Conference 2021. 29-30 September 2021, Baden/Zurich, Switzerland.
5. **C. Tosto**, L. Saitta, A. Latteri, F. Miani, G. Cicala. Fused Filament Fabrication of Polymeric Filaments filled with 17-4 PH metal particles: The effect of different printing profiles on Green and Sintered parts. XVI Convegno Nazionale AIMAT 2021, 15-18 September 2021, Cagliari, Italy.
6. C. Tosto, L. Saitta, E. Pergolizzi, G. Cicala. Composites tooling manufactured by additive manufacturing (AM): The effects of the selected AM technology. XVI Convegno Nazionale AIMAT 2021, 15-18 September 2021, Cagliari, Italy.

¹In bold the name of the author who presented the work.

7. L. Saitta, C. Tosto, S. Dattilo, C. Puglisi, G. Cicala. Chemical Recycling of Bioepoxy matrices for Composites: Novel processing route and reuse strategies to obtain new matrices. XVI Convegno Nazionale AIMAT 2021, 15-18 September 2021, Cagliari, Italy..
8. C. Sergi, G. Cicala, F. Sarasini, C. Tosto, J. Tirillò. Combination of Fused Deposition Modeling (FDM) 3D-Printing and Sintering to Produce dense Metal parts. XVI Convegno Nazionale AIMAT 2021, 15-18 September 2021, Cagliari, Italy.
9. **C. Tosto**, A.D. La Rosa, S. Greco, G. Cicala. CF- thermoplastic composites: LCA and LCC analysis of a chemical recycling process. *Polymers and Sustainability*, 1-3 September 2021, Lampedusa, Italy.
10. A. Latteri, C. Tosto, L. Saitta, G. Cicala. The use of additive manufacturing as a viable tool for easy composites processing: LCA evaluation and cost analysis. *Polymers and Sustainability*, 1-3 September 2021, Lampedusa, Italy.
11. L. Saitta, C. Tosto, S. Dattilo, C. Puglisi, G. Cicala. Bio-epoxy matrices for composites: from recycling to possible re-uses. *Polymers and Sustainability*, 1-3 September 2021, Lampedusa, Italy.
12. **C. Tosto**, G. Cicala, I. Blanco, A. Patti, L. Saitta. Effect of Porosity on the Thermal Conductivity of 3D Printed Parts by Fused Filament Fabrication (FFF). XLII National Conference on Calorimetry, Thermal Analysis and Applied Thermodynamics, 27-28 January 2021, Udine, Italy (online).
13. **C. Tosto**, I. Blanco, G. Cicala. Epoxy Resin Formulation for 3D Printing by Liquid Crystal Display (LCD). XLII National Conference on Calorimetry, Thermal Analysis and Applied Thermodynamics, 27-28 January 2021, Udine, Italy (online).
14. **C. Tosto**, L. Saitta, E. Pergolizzi, A. Patti, G. Celano, G. Cicala. Fused Deposition Modelling: New Standards for mechanical characterization. POLCOM 26-28 November 2020, Bucharest, Romania.
15. G. Cicala, C. Tosto, G. Recca, A. Patti. Additive Manufacturing processing of plastics for mass production of composites tooling: technical and economic analysis. POLCOM 26-28 November 2020, Bucharest, Romania.
16. L. Saitta, C. Tosto, E. Pergolizzi, A. Patti, G. Cicala. Liquid Crystal Display (LCD) printing: a novel system for polymer hybrids printing. POLCOM 26-28 November 2020, Bucharest, Romania.

17. Blanco, G. Cicala, C. Tosto, G. Recca, G. Dal Poggetto, M. Catauro. Kinetic study of the thermal dehydration of fly ash filled Geopolymers. POLCOM 26-28 November 2020, Bucharest, Romania.
18. **C. Tosto**, A. Latteri, E. Pergolizzi, D. Giordano, G. Abramo, R. Catenaro, N. Pignotti, G. Cicala (2019) Additive Manufacturing of Plastics: an efficient approach for composites tooling - Macromolecular Symposia - POLCOM 10-13 October 2019, Bucharest, Romania.
19. G. Ognibene, **C. Tosto**, L. Saitta, G. Cicala, M.E. Fragalà, G. Li Volti (2019) Coatings with antibacterial properties for electrospun materials and additive manufacturing - Materials in the next decade 2019, 18-20 September 2019, Favignana, Italy.
20. G. Ognibene, I. Blanco, L. Saitta, C. Tosto, G. Cicala (2019) The use of thermo-mechanical technique to support the development of novel materials for additive manufacturing - CEEC-TAC5 & Medicta2019 - 27-30 August 2019, Roma, Italy.
21. **C. Tosto**, E. Pergolizzi, I. Blanco, G. Cicala (2019) Thermomechanical properties of mandrels manufactured by 3D printing for the production of hollow FRP parts - CEEC-TAC5 & Medicta2019 - 27-30 August 2019, Roma, Italy.
22. **C. Tosto**, G. Ognibene, L. Saitta, G. Recca, G. Cicala (2019) Epoxy blending for resins used in advanced manufacturing by DLP printing - XII INSTM CONFERENCE-XV AIMAT CONFERENCE, 21-24 July 2019, Ischia, Italy.
23. **C. Tosto**, G. Ognibene, L. Saitta, R. Catenaro, G. Cicala (2019) Additive manufacturing for tooling of plastics and fiber reinforced composites - XII INSTM CONFERENCE-XV AIMAT CONFERENCE, 21-24 July 2019, Ischia, Italy.
24. G. Ognibene, C. Tosto, G. Li Volti, M.E. Fragalà, L. Saitta, G. Cicala (2019) Functional electrospun veils: application from wound healing to frp composites - XII INSTM CONFERENCE-XV AIMAT CONFERENCE, 21-24 July 2019, Ischia, Italy.
25. S. Oliva, C. Tosto, A. Latteri, I. Blanco, G. Recca, G.Cicala (2019) Polymer Blends for Day-Light curing: application to DLP 3D printing - Eurofillers Polymer Blends 2019, 23-26 April 2019, Palermo, Italy.
26. G. Ognibene, M.E. Fragalà, C.Tosto, A. Di Stefano, G. Li Volti, G.Cicala (2019) Electrospun Polyethersulfone nanofibers as cells scaffold - Eurofillers Polymer Blends 2019, 23-26 April 2019, Palermo, Italy.

Bibliography

- [1] 3dxtech. 3dxtech - PLA CF15. <https://www.3dxtech.com/products/carbon-fiber-fila>. pages <https://www.3dxtech.com/products/carbon-fiber-fila>.
- [2] 3dxtech. 3dxtech - PLACF20. <https://www.3dxtech.com/product/carbonx-pla-cf/~>. pages <https://www.3dxtech.com/product/carbonx-pla-cf/~>.
- [3] M K Agarwala, R Van Weeren, A Bandyopadhyay, A Safari, S C Danforth, and W R Priedeman. Filament Feed Materials for Fused Deposition Processing of Ceramics and Metals. *Proceedings of the Solid Freeform Fabrication Symposium*, pages 451–458, 1996.
- [4] Sung Hoon Ahn, Michael Montero, Dan Odell, Shad Roundy, and Paul K. Wright. Anisotropic material properties of fused deposition modeling ABS. *Rapid Prototyping Journal*, 8(4):248–257, 2002.
- [5] Sara Black. 3D Printing Moves Into Tooling Components : CompositesWorld. <https://www.compositesworld.com/articles/3d-printing-moves-into-tooling-components>. pages <https://www.compositesworld.com/articles/3d-printi>.
- [6] Ignazio Blanco, Gianluca Cicala, Giulia Ognibene, Mario Rapisarda, and Antonino Recca. Thermal properties of polyetherimide/polycarbonate blends for advanced applications. *Polymer Degradation and Stability*, 154:234–238, aug 2018.
- [7] L. G. Blok, M. L. Longana, H. Yu, and B. K.S. Woods. An investigation into 3D printing of fibre reinforced thermoplastic composites. *Additive Manufacturing*, 22:176–186, aug 2018.
- [8] Kate Iren Byberg, Aboma Wagari Gebisa, and Hirpa G. Lemu. Mechanical properties of ULTEM 9085 material processed by fused deposition modeling. *Polymer Testing*, 72:335–347, dec 2018.

- [9] Fabiana Cairone, Santi Davi, Giovanna Stella, Francesca Guarino, Giuseppe Recca, Gianluca Cicala, and Maide Bucolo. 3D-Printed micro-optofluidic device for chemical fluids and cells detection. *Biomedical Microdevices*, 22(2), jun 2020.
- [10] Fabiana Cairone, Salvina Gagliano, and Maide Bucolo. Experimental study on the slug flow in a serpentine microchannel. *Experimental Thermal and Fluid Science*, 76:34–44, sep 2016.
- [11] M. A. Caminero, J. M. Chacón, I. García-Moreno, and J. M. Reverte. Interlaminar bonding performance of 3D printed continuous fibre reinforced thermoplastic composites using fused deposition modelling. *Polymer Testing*, 68:415–423, jul 2018.
- [12] Miguel Ángel Caminero, Jesús Miguel Chacón, Eustaquio García-Plaza, Pedro José Núñez, José María Reverte, and Jean Paul Becar. Additive manufacturing of PLA-based composites using fused filament fabrication: Effect of graphene nanoplatelet reinforcement on mechanical properties, dimensional accuracy and texture. *Polymers*, 11(5), may 2019.
- [13] Jonathan A. Campbell, Harrison Inglis, Elson Ng WeiLong, Cheylan McKinley, and David A. Lewis. Morphology control in a dual-cure system for potential applications in additive manufacturing. *Polymers*, 11(3), mar 2019.
- [14] G. Cicala, R. La Spina, A. Recca, and S. Sturiale. Influence of copolymer’s end groups and molecular weights on the rheological and thermomechanical properties of blends of novel thermoplastic copolymers and epoxy resins. *Journal of Applied Polymer Science*, 101(1):250–257, jul 2006.
- [15] G. Cicala and G. Recca. Studies on epoxy blends modified with a hyperbranched polyester. *Polymer Engineering Science*, 48(12):2382–2388, dec 2008.
- [16] G. Cicala, G. Recca, S. Carciotto, and C.L. Restuccia. Development of epoxy/hyperbranched blends for resin transfer molding and vacuum assisted resin transfer molding applications: Effect of a reactive diluent. *Polymer Engineering Science*, 49(3):577–584, mar 2009.
- [17] Gianluca Cicala, Davide Giordano, Claudio Tosto, Giovanni Filippone, Antonino Recca, and Ignazio Blanco. Polylactide (PLA) filaments a biobased solution for additive manufacturing: Correlating rheology and thermomechanical properties with printing quality. *Materials*, 11(7), jul 2018.
- [18] Gianluca Cicala, Antonino Mamo, Giuseppe Recca, and Carmelo Luca Restuccia. Study on epoxy/thermoplastic blends based on the addition of a novel aro-

- matic block copolymer. *Polymer Engineering and Science*, 47(12):2027–2033, dec 2007.
- [19] Gianluca Cicala, Giulia Ognibene, Salvatore Portuesi, Ignazio Blanco, Mario Rapisarda, Eugenio Pergolizzi, and Giuseppe Recca. Comparison of Ultem 9085 Used in Fused Deposition Modelling (FDM) with Polytherimide Blends. *Materials 2018, Vol. 11, Page 285*, 11(2):285, feb 2018.
- [20] N. McCrae D. Dahl. D. Dahl, N. McCrae, presented at CAMX 2018 à Composites. Google Scholar.
- [21] T. DebRoy, H. L. Wei, J. S. Zuback, T. Mukherjee, J. W. Elmer, J. O. Milewski, A. M. Beese, A. Wilson-Heid, A. De, and W. Zhang. Additive manufacturing of metallic components à Process, structure and properties. *Progress in Materials Science*, 92:112–224, mar 2018.
- [22] A.S. El-Gizawy. Process-induced properties of FDM products. *ICMET*, 2011.
- [23] EOS. Material data sheet-FlexLine. page www.eos.info.
- [24] O. S. Es-Said, J. Foyos, R. Noorani, M. Mendelson, R. Marloth, and B. A. Pregger. Effect of layer orientation on mechanical properties of rapid prototyped samples. *Materials and Manufacturing Processes*, 15(1):107–122, 2000.
- [25] Sulaymon Eshkabilov, Ismat Ara, Igor Sevostianov, Fardad Azarmi, and Xi-angping Tangpong. Mechanical and thermal properties of stainless steel parts, manufactured by various technologies, in relation to their microstructure. *International Journal of Engineering Science*, 159:103398, feb 2021.
- [26] Fiberforce. Fiberforce - PLA. www.fiberforce.it. page www.fiberforce.it.
- [27] William E. Frazier. Metal additive manufacturing: A review. *Journal of Materials Engineering and Performance*, 23(6):1917–1928, 2014.
- [28] P S Gaal, M.-A Thermitus, and Daniela E Stroë. THERMAL CONDUCTIVITY MEASUREMENTS USING THE FLASH METHOD. Technical report, 2004.
- [29] Manuela Galati and Paolo Minetola. Analysis of Density, Roughness, and Accuracy of the Atomic Diffusion Additive Manufacturing (ADAM) Process for Metal Parts. *Materials 2019, Vol. 12, Page 4122*, 12(24):4122, dec 2019.
- [30] Manuela Galati and Paolo Minetola. Analysis of Density, Roughness, and Accuracy of the Atomic Diffusion Additive Manufacturing (ADAM) Process for Metal Parts. *Materials 2019, Vol. 12, Page 4122*, 12(24):4122, dec 2019.

- [31] Julien Gardan. Additive manufacturing technologies: state of the art and trends. <http://dx.doi.org/10.1080/00207543.2015.1115909>, 54(10):3118–3132, may 2015.
- [32] GE Additive. 17-4 PH GE. <https://www.ge.com/additive/sites/default/files/2016/05/17-4PH-GE-Additive-Manufacturing-Process-Overview.pdf> page <https://www.ge.com/additive/sites/default/files/2016/05/17-4PH-GE-Additive-Manufacturing-Process-Overview.pdf>.
- [33] GE Additive. 316L GE. <https://www.ge.com/additive/sites/default/files/2016/05/316L-GE-Additive-Manufacturing-Process-Overview.pdf> page <https://www.ge.com/additive/sites/default/files/2016/05/316L-GE-Additive-Manufacturing-Process-Overview.pdf>.
- [34] Aboma Wagari Gebisa and Hirpa G. Lemu. Investigating effects of Fused-deposition modeling (FDM) processing parameters on flexural properties of ULTEM 9085 using designed experiment. *Materials*, 11(4), mar 2018.
- [35] Damir Godec, Santiago Cano, Clemens Holzer, and Joamin Gonzalez-Gutierrez. Optimization of the 3D Printing Parameters for Tensile Properties of Specimens Produced by Fused Filament Fabrication of 17-4PH Stainless Steel. *Materials 2020, Vol. 13, Page 774*, 13(3):774, feb 2020.
- [36] Haijun Gong, Dean Snelling, Kamran Kardel, and Andres Carrano. Comparison of Stainless Steel 316L Parts Made by FDM- and SLM-Based Additive Manufacturing Processes. *JOM 2018 71:3*, 71(3):880–885, nov 2018.
- [37] Haijun Gong, Dean Snelling, Kamran Kardel, and Andres Carrano. Comparison of Stainless Steel 316L Parts Made by FDM- and SLM-Based Additive Manufacturing Processes. *JOM*, 71(3):880–885, mar 2019.
- [38] J. Gonzalez-Gutierrez, D. Godec, R. GuráÅ, M. Spoerk, C. Kukla, and C. Holzer. 3D printing conditions determination for feedstock used in fused filament fabrication (FFF) of 17-4PH stainless steel parts. *METALURGIJA*, 57:1–2, 2018.
- [39] Joamin Gonzalez-Gutierrez, Florian Arbeiter, Thomas Schlauf, Christian Kukla, and Clemens Holzer. Tensile properties of sintered 17-4PH stainless steel fabricated by material extrusion additive manufacturing. *Materials Letters*, 248:165–168, aug 2019.
- [40] Wolfgang Grellmann and Sabine Seidler. *Polymer Testing 2 nd Edition*.
- [41] Gianmarco Griffini, Marta Invernizzi, Marinella Levi, Gabriele Natale, Giovanni Postiglione, and Stefano Turri. 3D-printable CFR polymer composites with dual-cure sequential IPNs. *Polymer*, 91:174–179, may 2016.
- [42] Xinyu GU, Justin POELMA, and P. ROLLAND, Jason. METHODS OF MAKING THREE DIMENSIONAL OBJECTS FROM DUAL CURE RESINS WITH SUPPORTED SECOND CURE. mar 2017.

- [43] Chuigen Guo, Lin Zhou, and Jianxiong Lv. Effects of Expandable Graphite and Modified Ammonium Polyphosphate on the Flame-Retardant and Mechanical Properties of Wood Flour-Polypropylene Composites. <https://doi.org/10.1177/096739111302100706>, 21(7):449–456, sep 2013.
- [44] Muhammad Harris, Johan Potgieter, Richard Archer, and Khalid Mahmood Arif. Effect of material and process specific factors on the strength of printed parts in fused filament fabrication: A review of recent developments. *Materials*, 12(10), may 2019.
- [45] Paul Holt. Methods For Making A Metal, Sand Or Ceramic Object By Additive Manufacture And Formulations For Use In Said Methods Holt; Paul ; et al. [PhotoCentriC Limited].
- [46] N Hopkinson and P Dicknes. Analysis of rapid manufacturing using layer manufacturing processes for production. <http://dx.doi.org/10.1243/095440603762554596>, 217(1):31–40, dec 2005.
- [47] Shrenik Kumar Jain and Yonas Tadesse. Fabrication of Polylactide/Carbon Nanopowder Filament using Melt Extrusion and Filament Characterization for 3D Printing. <https://doi.org/10.1142/S0219581X18500266>, 18(5), jul 2019.
- [48] Shenglong Jiang, Guangxin Liao, Dingding Xu, Fenghua Liu, Wen Li, Yuchuan Cheng, Zhixiang Li, and Gaojie Xu. Mechanical properties analysis of polyetherimide parts fabricated by fused deposition modeling. *High Performance Polymers*, 31(1):97–106, feb 2019.
- [49] Achim Kampker, Peter Ayvaz, and Gerret Lukas. Direct polymer additive tooling – economic analysis of additive manufacturing technologies for fabrication of polymer tools for injection molding. *Key Engineering Materials*, 843 KEM:9–18, 2020.
- [50] Mohammad Reza Khosravani and Ali Zolfagharian. Fracture and load-carrying capacity of 3D-printed cracked components. *Extreme Mechanics Letters*, 37:100692, may 2020.
- [51] Osman Konuray, Xavier Fernández-Francos, Xavier Ramis, and Àngels Serra. State of the art in dual-curing acrylate systems. *Polymers*, 10(2), feb 2018.
- [52] Takashi Kurose, Yoshifumi Abe, Marcelo V.A. Santos, Yota Kanaya, Akira Ishigami, Shigeo Tanaka, and Hiroshi Ito. Influence of the layer directions on the properties of 316l stainless steel parts fabricated through fused deposition of metals. *Materials*, 13(11), jun 2020.

- [53] Tomasz Kurzynowski, Konrad Gruber, Wojciech Stopyra, Bogumiła Kuźnicka, and Edward Chlebus. Correlation between process parameters, microstructure and properties of 316L stainless steel processed by selective laser melting. *Materials Science and Engineering: A*, 718:64–73, mar 2018.
- [54] Vladimir E. Kuznetsov, Alexey N. Solonin, Oleg D. Urzhumtsev, Richard Schilling, and Azamat G. Tavitov. Strength of PLA components fabricated with fused deposition technology using a desktop 3D printer as a function of geometrical parameters of the process. *Polymers*, 10(3), mar 2018.
- [55] Simone Lantean, Ignazio Roppolo, Marco Sangermano, Candido Fabrizio Pirri, and Annalisa Chiappone. Development of new hybrid acrylic/epoxy DLP-3D printable materials. *Inventions*, 3(2), jun 2018.
- [56] B. H. Lee, J. Abdullah, and Z. A. Khan. Optimization of rapid prototyping parameters for production of flexible ABS object. *Journal of Materials Processing Technology*, 169(1):54–61, oct 2005.
- [57] H. Li, G. Taylor, V. Bheemreddy, O. Iyibilgin, M. Leu, and K. Chandrashekhara. Modeling and characterization of fused deposition modeling tooling for vacuum assisted resin transfer molding process. *Additive Manufacturing*, 7:64–72, jul 2015.
- [58] Chya-Yan Liaw and Murat Guvendiren. Current and emerging applications of 3D printing in medicine. *Biofabrication*, 9(2):024102, jun 2017.
- [59] Bin Lin and Uttandaraman Sundararaj. Visualization of Poly(ether imide) and Polycarbonate Blending in an Internal Mixer. *Journal of Applied Polymer Science*, 92(2):1165–1175, apr 2004.
- [60] R van Weeren A Bandyopadhyay P J Whalen A Safari S C Danforth M K Agarwala. Fused Deposition of Ceramics and Metals : An Overview. pages 1–8, 2008.
- [61] A. Maffezzoli, R. Terzi, and L. Nicolais. Cure behaviour of visible light activated dental composites - Part I Isothermal kinetics. *Journal of Materials Science: Materials in Medicine*, 6(3):155–160, mar 1995.
- [62] Valentina Mazzanti, Lorenzo Malagutti, and Francesco Mollica. polymers FDM 3D Printing of Polymers Containing Natural Fillers: A Review of their Mechanical Properties.
- [63] Kevin P. Menard. Dynamic Mechanical Analysis. may 2008.

- [64] Jorge Manuel Mercado-Colmenero, Miguel Angel Rubio-Paramio, M. Dolores La Rubia, David Lozano-Arjona, and Cristina Martin-Doñate. A numerical and experimental study of the compression uniaxial properties of PLA manufactured with FDM technology based on product specifications. *International Journal of Advanced Manufacturing Technology*, 103(5-8):1893–1909, aug 2019.
- [65] Krishna P. Motaparti, Gregory Taylor, Ming C. Leu, K. Chandrashekhara, James Castle, and Mike Matlack. Experimental investigation of effects of build parameters on flexural properties in fused deposition modelling parts. *Virtual and Physical Prototyping*, 12(3):207–220, jul 2017.
- [66] Philip Obst, Julius Riedelbauch, Paul Oehlmann, Dominik Rietzel, Martin Launhardt, Stefan Schmölzer, Tim A. Osswald, and Gerd Witt. Investigation of the influence of exposure time on the dual-curing reaction of RPU 70 during the DLS process and the resulting mechanical part properties. *Additive Manufacturing*, 32, mar 2020.
- [67] Heather J. O’Connor and Denis P. Dowling. Low-pressure additive manufacturing of continuous fiber-reinforced polymer composites. *Polymer Composites*, 40(11):4329–4339, nov 2019.
- [68] Optimim. 316L Stainless Steel - MIM Materials. <https://www.optimim.com/metal-injection-molding-mi>. pages <https://www.optimim.com/metal-injection-molding-mi>.
- [69] Antonella Patti, Domenico Acierno, Alberta Latteri, Claudio Tosto, Eugenio Pergolizzi, Giuseppe Recca, Mirko Cristaudo, and Gianluca Cicala. Influence of the Processing Conditions on the Mechanical Performance of Sustainable Bio-Based PLA Compounds.
- [70] Xingshuang Peng, Miaomiao Zhang, Zhengchuan Guo, Lin Sang, and Wenbin Hou. Investigation of processing parameters on tensile performance for FDM-printed carbon fiber reinforced polyamide 6 composites. *Composites Communications*, 22:100478, dec 2020.
- [71] Proto Pasta. Proto Pasta - PLA. <https://www.kickstarter.com/projects/1375236253/pr>. page <https://www.kickstarter.com/projects/1375236253/pr>.
- [72] Haoyuan Quan, Ting Zhang, Hang Xu, Shen Luo, Jun Nie, and Xiaoqun Zhu. Photo-curing 3D printing technique and its challenges. *Bioactive Materials*, 5(1):110–115, mar 2020.
- [73] Alec Redmann, Paul Oehlmann, Thomas Scheffler, Lukas Kagermeier, and Tim A. Osswald. Thermal curing kinetics optimization of epoxy resin in Digital Light Synthesis. *Additive Manufacturing*, 32, mar 2020.

- [74] Cynthia Richard, Cynthia Richard, Adrian Neild, Victor J. Cadarso, and Victor J. Cadarso. The emerging role of microfluidics in multi-material 3D bio-printing. *Lab on a Chip*, 20(12):2044–2056, jun 2020.
- [75] Madhuparna Roy and Tarik J. Dickens. Additive technology of soluble mold tooling for embedded devices in composite structures: A study on manufactured tolerances. *Additive Manufacturing*, 15:78–86, may 2017.
- [76] M. Ruffo, C. Tuck, and R. Hague. Cost estimation for rapid manufacturing - Laser sintering production for low to medium volumes. *Proceedings of the Institution of Mechanical Engineers, Part B: Journal of Engineering Manufacture*, 220(9):1417–1427, 2006.
- [77] S Rusnakova, A Capka, L Fojtl, M Zaludek Manufacturing . . . , and undefined 2016. Technology and mold design for production of hollow carbon composite parts. *journalmt.com*, 16(4), 2016.
- [78] F. Sapuppo, M. Bucolo, M. Intaglietta, L. Fortuna, and P. Arena. A cellular nonlinear network: Real-time technology for the analysis of microfluidic phenomena in blood vessels. *Nanotechnology*, 17(4), feb 2006.
- [79] Sd3d. Sd3d. <https://www.sd3d.com/portfolio/carbon-fiber-pla/>. pages <https://www.sd3d.com/portfolio/carbon-fiber-pla/>.
- [80] Juliana Breda Soares, João Finamor, Fabio Pinto Silva, Liane Roldo, and Luis Henrique Cândido. Analysis of the influence of polylactic acid (PLA) colour on FDM 3D printing temperature and part finishing. *Rapid Prototyping Journal*, 24(8):1305–1316, nov 2018.
- [81] V. Tambrallimath, R. Keshavamurthy, Saravanabavan D, Praveennath G. Koppad, and G. S.Pradeep Kumar. Thermal behavior of PC-ABS based graphene filled polymer nanocomposite synthesized by FDM process. *Composites Communications*, 15:129–134, oct 2019.
- [82] Yvonne Thompson, Joamin Gonzalez-Gutierrez, Christian Kukla, and Peter Felfer. Fused filament fabrication, debinding and sintering as a low cost additive manufacturing method of 316L stainless steel. *Additive Manufacturing*, 30:100861, dec 2019.
- [83] Angel R. Torrado and David A. Roberson. Failure Analysis and Anisotropy Evaluation of 3D-Printed Tensile Test Specimens of Different Geometries and Print Raster Patterns. *Journal of Failure Analysis and Prevention*, 16(1):154–164, feb 2016.

-
- [84] Claudio Tosto, Alberta Latteri, Eugenio Pergolizzi, Davide Giordano, Giuseppe Abramo, Roberto Catenaro, Nazzareno Pignotti, and Gianluca Cicala. Additive Manufacturing of Plastics: An Efficient Approach for Composite Tooling. *Macromolecular Symposia*, 389(1), feb 2020.
- [85] Claudio Tosto, Eugenio Pergolizzi, Ignazio Blanco, Antonella Patti, Paul Holt, Sarah Karmel, and Gianluca Cicala. Epoxy based blends for additive manufacturing by liquid crystal display (LCD) printing: The effect of blending and dual curing on daylight curable resins. *Polymers*, 12(7), 2020.
- [86] Claudio Tosto, Lorena Saitta, Eugenio Pergolizzi, Ignazio Blanco, Giovanni Celano, and Gianluca Cicala. Methods for the Characterization of Polyetherimide Based Materials Processed by Fused Deposition Modelling. *Applied Sciences 2020*, Vol. 10, Page 3195, 10(9):3195, may 2020.
- [87] Claudio Tosto, Jacopo Tirillò, Fabrizio Sarasini, and Gianluca Cicala. Hybrid Metal/Polymer Filaments for Fused Filament Fabrication (FFF) to Print Metal Parts. 2021.
- [88] Sigmund A. Tronvoll, Torgeir Welo, and Christer W. Elverum. The effects of voids on structural properties of fused deposition modelled parts: a probabilistic approach. *The International Journal of Advanced Manufacturing Technology 2018 97:9*, 97(9):3607–3618, may 2018.
- [89] John R. Tumbleston, David Shirvanyants, Nikita Ermoshkin, Rima Januszewicz, Ashley R. Johnson, David Kelly, Kai Chen, Robert Pinschmidt, Jason P. Rolland, Alexander Ermoshkin, Edward T. Samulski, and Joseph M. DeSimone. Continuous liquid interface production of 3D objects. *Science*, 347(6228):1349–1352, mar 2015.
- [90] Daniel Alexander Turk, Andreas Ebnother, Markus Zogg, and Mirko Meboldt. Additive manufacturing of structural cores and washout tooling for autoclave curing of hybrid composite structures. *Journal of Manufacturing Science and Engineering, Transactions of the ASME*, 140(10), oct 2018.
- [91] Daniel Alexander Türk, Ralph Kussmaul, Markus Zogg, Christoph Klahn, Bastian Leutenecker-Twelsiek, and Mirko Meboldt. Composites Part Production with Additive Manufacturing Technologies. *Procedia CIRP*, 66:306–311, jan 2017.
- [92] Ultimaker. Ultimaker - PLA. <https://ultimaker.com/it/materials/pla>. page <https://ultimaker.com/it/materials/pla>.
- [93] Uzair Khaleeq uz Zaman, Emilien Boesch, Ali Siadat, Mickael Rivette, and Aamer Ahmed Baqai. Impact of fused deposition modeling (FDM) process

- parameters on strength of built parts using Taguchi's design of experiments. *International Journal of Advanced Manufacturing Technology*, 101(5-8):1215–1226, apr 2019.
- [94] Ana Pilar Valerga, Moisés Batista, Jorge Salguero, and Frank Girot. Influence of PLA filament conditions on characteristics of FDM parts. *Materials*, 11(8), jul 2018.
- [95] Verbatim. Verbatim - PLA. <https://www.verbatim.it/it/prod/verbatim-pla-filam>. pages <https://www.verbatim.it/it/prod/verbatim-pla-filam>.
- [96] Carlos M.S. Vicente, Tomás S. Martins, Marco Leite, António Ribeiro, and Luís Reis. Influence of fused deposition modeling parameters on the mechanical properties of ABS parts. *Polymers for Advanced Technologies*, 31(3):501–507, mar 2020.
- [97] Sidra Waheed, Joan M. Cabot, Niall P. Macdonald, Trevor Lewis, Rosanne M. Guijt, Brett Paull, and Michael C. Breadmore. 3D printed microfluidic devices: Enablers and barriers. *Lab on a Chip*, 16(11):1993–2013, 2016.
- [98] Jianlei Wang, Suhail Mubarak, Duraisami Dhamodharan, Nidhin Divakaran, Lixin Wu, and Xu Zhang. Fabrication of thermoplastic functionally gradient composite parts with anisotropic thermal conductive properties based on multicomponent fused deposition modeling 3D printing. *Composites Communications*, 19:142–146, jun 2020.
- [99] Ben Wittbrodt and Joshua M. Pearce. The effects of PLA color on material properties of 3-D printed components. *Additive Manufacturing*, 8:110–116, oct 2015.
- [100] Guohua Wu, Noshir Langrana, Sriram Rangarajan, Rajendra Sadangi, Amhad Safari, and Stephen C. Danforth. Feasibility of Fabricating Metal Parts from 17-4PH Stainless Steel Powder. *Proceedings of Solid Freeform Fabrication Symposium*, pages 479–486, 1998.
- [101] R. J. Zaldivar, D. B. Witkin, T. McLouth, D. N. Patel, K. Schmitt, and J. P. Nokes. Influence of processing and orientation print effects on the mechanical and thermal behavior of 3D-Printed ULTEM [®] 9085 Material. *Additive Manufacturing*, 13:71–80, jan 2017.
- [102] Wei Zhang, Chase Cotton, Jessica Sun, Dirk Heider, Bohong Gu, Baozhong Sun, and Tsu Wei Chou. Interfacial bonding strength of short carbon fiber/acrylonitrile-butadiene-styrene composites fabricated by fused deposition modeling. *Composites Part B: Engineering*, 137:51–59, mar 2018.

- [103] Junzhe Zhu, Qiang Zhang, Tianqing Yang, Yu Liu, and Ren Liu. 3D printing of multi-scalable structures via high penetration near-infrared photopolymerization. *Nature Communications*, 11(1), dec 2020.

Appendix A

AM Standards and Filaments

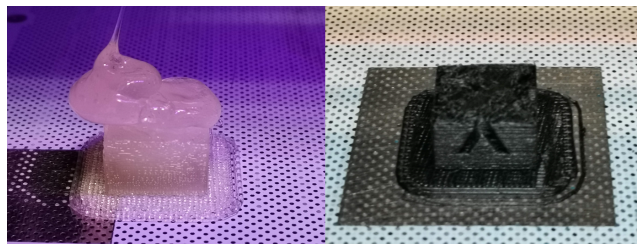


Figure A.1: Calibration cubes from a printing with wrong settings.

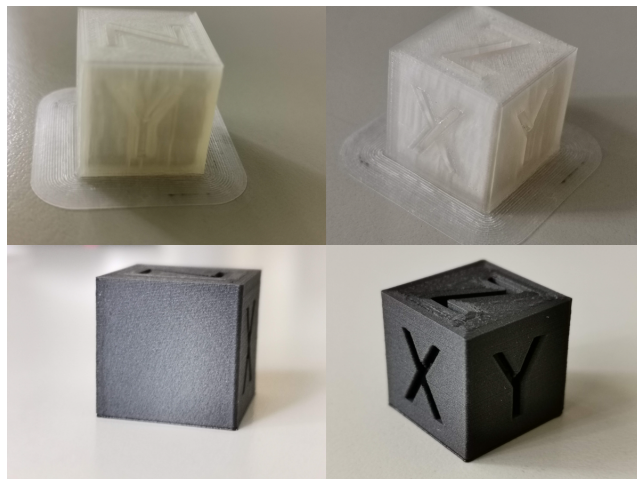


Figure A.2: Calibration cubes from optimized printing.

Printing parameter	Unit	Value	
		PLA	PLA+CF
Nozzle diameter	mm	0.4	0.6
Wall thickness	mm	1	1
Wall line count	-	3	3
Layer thickness	mm	0.2	0.2
Infill	%	100	100
Raster angles	deg	[0][45,135][0,90]	
Printing temperature	°C	200	210
Plate temperature	°C	60	60
Print speed	mm/s	70	45
Fan speed	%	100	50
Retraction distance	mm	6,5	6,5
Retraction speed	mm/s	25	25

Table A.1: Printing parameter for PLA and PLA CF-reinforced on Ultimaker S5.

Response	1 Tensile Modulus					
ANOVA for selected factorial model						
Analysis of variance table [Classical sum of squares - Type II]						
Source	Sum of Squares	df	Mean Square	F Value	p-value Prob > F	
Model	49.91	11	4.54	324.25	< 0.0001	significant
<i>A-Material</i>	41.81	3	13.94	995.97	< 0.0001	
<i>B-Raster Angle</i>	5.64	2	2.82	201.63	< 0.0001	
<i>AB</i>	2.46	6	0.41	29.27	< 0.0001	
Pure Error	0.34	24	0.014			
Cor Total	50.24	35				
Std. Dev.	0.12		R-Squared	0.9933		
Mean	6.00		Adj R-Squarec	0.9903		
C.V. %	1.97		Pred R-Square	0.9850		

Figure A.3: ANOVA table for tensile modulus response.

Response 2		Tensile Strength				
ANOVA for selected factorial model						
Analysis of variance table [Classical sum of squares - Type II]						
Source	Sum of Squares	df	Mean Square	F Value	p-value Prob > F	
Model	8501.30	5	1700.26	652.19	< 0.0001	significant
<i>A-Material</i>	<i>8186.06</i>	<i>3</i>	<i>2728.69</i>	<i>1046.67</i>	<i>< 0.0001</i>	
<i>B-Raster Angle</i>	<i>315.24</i>	<i>2</i>	<i>157.62</i>	<i>60.46</i>	<i>< 0.0001</i>	
Residual	78.21	30	2.61			
<i>Lack of Fit</i>	<i>29.85</i>	<i>6</i>	<i>4.97</i>	<i>2.47</i>	<i>0.0530</i>	<i>not significant</i>
<i>Pure Error</i>	<i>48.36</i>	<i>24</i>	<i>2.02</i>			
Cor Total	8579.51	35				
Std. Dev.	1.61		R-Squared	0.9909		
Mean	63.02		Adj R-Squared	0.9894		
C.V. %	2.56		Pred R-Squared	0.9869		

Figure A.4: ANOVA table for tensile strength response.

Response 3		Elongation at Break				
ANOVA for selected factorial model						
Analysis of variance table [Classical sum of squares - Type II]						
Source	Sum of Squares	df	Mean Square	F Value	p-value Prob > F	
Model	7.07	11	0.64	68.97	< 0.0001	significant
<i>A-Material</i>	<i>6.81</i>	<i>3</i>	<i>2.27</i>	<i>243.68</i>	<i>< 0.0001</i>	
<i>B-Raster Angle</i>	<i>0.014</i>	<i>2</i>	<i>7.169E-003</i>	<i>0.77</i>	<i>0.4744</i>	
<i>AB</i>	<i>0.24</i>	<i>6</i>	<i>0.041</i>	<i>4.35</i>	<i>0.0042</i>	
Pure Error	0.22	24	9.318E-003			
Cor Total	7.29	35				
Std. Dev.	0.097		R-Squared	0.9693		
Mean	1.53		Adj R-Squared	0.9553		
C.V. %	6.32		Pred R-Squared	0.9310		

Figure A.5: ANOVA table for elongation at break response.

Standard order	Run order	Factor A: Material	Factor B: Geometry	Response 1: Young's Modulus [GPa]	Response 2: UTS [MPa]
1	6	Tan	Type I	2.14	61.061
2	16	Tan	Type I	2.17	59.863
3	9	Tan	Type I	2.22	61.983
4	20	Tan	Type I	2.24	60.657
5	1	Tan	Type I	2.13	58.545
6	7	Black	Type I	2.17	57.522
7	12	Black	Type I	2.2	59.065
8	19	Black	Type I	2.15	57.817
9	14	Black	Type I	2.17	57.61
10	3	Black	Type I	2.21	60.552
11	17	Tan	Type IV	2.32	64.08
12	2	Tan	Type IV	2.16	48.99
13	11	Tan	Type IV	2.34	57.389
14	13	Tan	Type IV	2.33	60.004
15	15	Tan	Type IV	2.31	61.845
16	4	Black	Type IV	2.08	59.717
17	18	Black	Type IV	2.05	59.352
18	5	Black	Type IV	2.08	59.579
19	8	Black	Type IV	2.16	58.974
20	10	Black	Type IV	2.15	58.332

Table A.2: Tensile test experimental results obtained from 20 runs.

Standard order	Run order	Factor A: Material	Factor B: Geometry [mm]	Response 1: Flexural Strength [MPa]
1	1	Tan	122	94.09
2	13	Tan	122	98.3
3	9	Tan	122	112.9
4	17	Tan	122	101
5	19	Tan	122	95.19
6	8	Black	122	85.07
7	15	Black	122	96.39
8	14	Black	122	102.09
9	3	Black	122	101.2
10	6	Black	122	86.2
11	7	Tan	165	108.02
12	20	Tan	165	97.54
13	5	Tan	165	95.93
14	10	Tan	165	106.98
15	16	Tan	165	92.81
16	2	Black	165	106.54
17	12	Black	165	77.48
18	11	Black	165	85.55
19	18	Black	165	96.5
20	4	Black	165	77.96

Table A.3: Flexural test experimental results obtained from 20 runs.

Standard order	Run order	Factor A: Material	Factor B: Geometry [mm]	Response: ILSS [MPa]
1	9	Tan	122	12.66
2	5	Tan	122	12.6
3	17	Tan	122	12.68
4	16	Tan	122	12.76
5	10	Tan	122	12.46
6	19	Black	122	16
7	11	Black	122	16.06
8	4	Black	122	16.74
9	7	Black	122	14.75
10	12	Black	122	14.99
11	18	Tan	165	11.82
12	20	Tan	165	11.99
13	6	Tan	165	12.32
14	15	Tan	165	11.92
15	2	Tan	165	12.44
16	3	Black	165	15.96
17	1	Black	165	15.65
18	8	Black	165	16.62
19	14	Black	165	15.35
20	13	Black	165	15.54

Table A.4: SBS test experimental results obtained from 20 runs.

Material	Raster Angle [deg]	Conditioning	Young's Modulus [GPa]	Yield Stress [MPa]	Elongation at Break [%]
PA66-CF10	0	NoDrying	3.07	47.61	7.14
PA66-CF10	0	NoDrying	3.20	48.32	4.25
PA66-CF10	0	NoDrying	3.03	44.01	4.77
PA66-CF10	45/135	NoDrying	2.31	42.10	5.84
PA66-CF10	45/135	NoDrying	2.32	42.51	8.05
PA66-CF10	45/135	NoDrying	2.26	41.32	7.26
PA66-CF10	0/90	NoDrying	2.44	42.88	5.75
PA66-CF10	0/90	NoDrying	2.40	42.45	6.48
PA66-CF10	0/90	NoDrying	2.43	41.45	5.34
PA66-CF10	0	Drying	4.69	66.81	4.10
PA66-CF10	0	Drying	4.71	65.51	3.49
PA66-CF10	0	Drying	4.53	63.51	3.94
PA66-CF10	45/135	Drying	3.52	56.50	4.22
PA66-CF10	45/135	Drying	3.30	54.67	4.10
PA66-CF10	45/135	Drying	3.46	54.80	4.13
PA66-CF10	0/90	Drying	3.81	58.39	3.79
PA66-CF10	0/90	Drying	3.83	57.85	4.12
PA66-CF10	0/90	Drying	3.82	57.84	4.04
XT-CF20	0	NoDrying	4.265	37.172	1.569
XT-CF20	0	NoDrying	4.245	38.356	2.063
XT-CF20	0	NoDrying	4.289	38.835	1.729
XT-CF20	45/135	NoDrying	3.492	36.418	1.938
XT-CF20	45/135	NoDrying	3.502	36.27	2.011
XT-CF20	45/135	NoDrying	3.543	37.13	2.48
XT-CF20	0/90	NoDrying	3.686	36.551	2.119
XT-CF20	0/90	NoDrying	3.7	37.403	2.528
XT-CF20	0/90	NoDrying	3.613	35.104	1.715
XT-CF20	0	Drying	4.383	41.672	1.834
XT-CF20	0	Drying	4.444	38.777	1.333
XT-CF20	0	Drying	4.567	43.012	1.642
XT-CF20	45/135	Drying	3.614	40.898	2.466
XT-CF20	45/135	Drying	3.742	40.885	1.991
XT-CF20	45/135	Drying	3.71	41.213	2.443
XT-CF20	0/90	Drying	3.73	38.765	1.789
XT-CF20	0/90	Drying	3.796	39.6	1.971
XT-CF20	0/90	Drying	3.825	40.581	2.313

Figure A.6: Collected data for tensile test of CF-reinforced filaments.

Appendix B

LCD Formulations

ID Sample	Uncured	Photocured	Postcured in Oven	Isothermal [°C]	Peak ₁ [°C]	Onset ₁ [°C]	Heat ₁ [J/g]	Peak ₂ [°C]	Onset ₂ [°C]	Heat ₂ [J/g]
E	•				171.79	129.59	264.52	-	-	-
CE5050	•				183.23	148.69	174.53	259.3	253	9.88
CE7030	•				186.56	143.7	227.98	261.06	243.93	9.31
C	•				181	150.24	168.35	264.83	245.33	41.4
C		•			185.56	183.25	115.71	-	-	-
C		•	•	100	188.22	184.52	55.16	-	-	-
C		•	•	140	189.54	185.71	12.05	-	-	-
C		•	•	150	-	-	-	-	-	-

Figure B.1: Data obtained from the DSC analysis of the uncured blends.

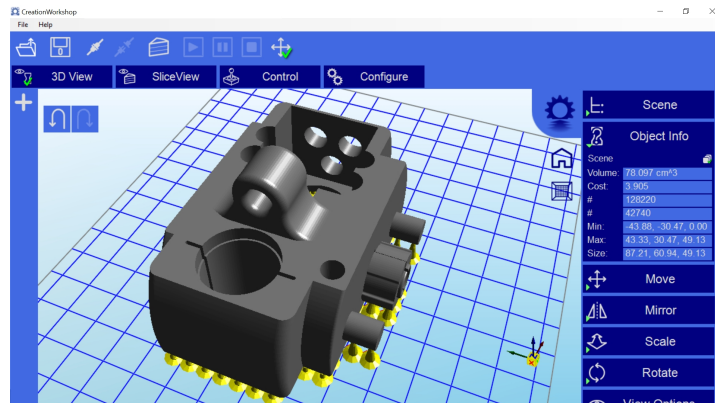


Figure B.2: Sample part for LCD printing.

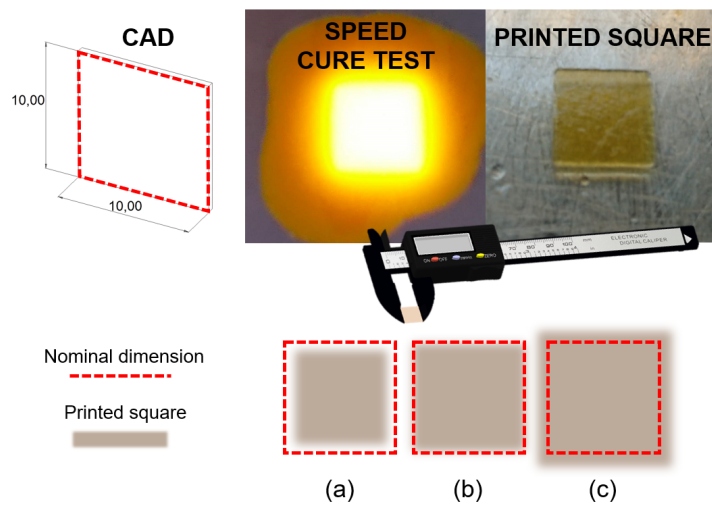


Figure B.3: Width overcure: (a) negative, resin not fully cured; (b) null, properly cured resin; (c) positive, resin over cured.

Resin Trade name	Producer	3D Technology	Tg [°C]	Viscosity [Poise]
Cyanate Ester	Carbon3D	DLS -Dual Curing	175	5
Prototyping Acrylate	Carbon3D	DLS -Dual Curing	47	-
Standard Resin	Wanhao	LCD	104	0.9
Fusion Gray	Asiga	DLP	160	-
PlasGray	Asiga	DLP	84	3.43
Basic	Zortrax	DLP	80*	1.7
PLASTCure Rigid 10 500	Prodways	DLP	125*	1.1
Cream Hard	Photocentric	LCD Daylight-Dual Cure	45	1.2
Cream Hard	Photocentric	LCD Daylight-Dual Cure (Post thermal curing - in this study)	137	1.2
CE7030	This study	LCD Daylight-Dual Cure	165	6.3
CE5050	This study	LCD Daylight-Dual Cure	174	12

Figure B.4: Comparison of the properties of epoxy based blends with some commercial LCD/DLS-Dual Curing resin. *Producers reported HDT rather than Tg.

Appendix C

Metal AM

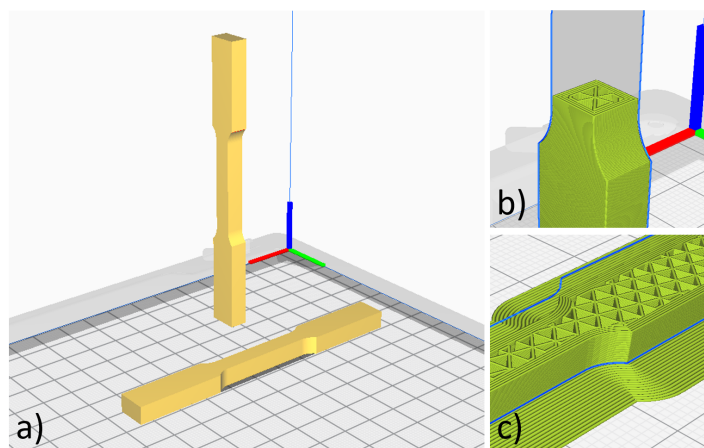


Figure C.1: Slicing view of the 17-4PH samples: a) Upright and flatwise build orientations; b) Infill of the upright samples; c) Infill of the flatwise samples.



Figure C.2: Tensile test configuration.

Acknowledgments

This PhD project was funded by MIUR, CUP E67I18001120006, Title “Advanced Materials for Additive manufacturing” (AMA), within the PON Ricerca e Innovazione 2014–2020 Asse I “Investimenti in Capitale Umano” -Azione I.1 “Dottorati Innovativi Con Caratterizzazione Industriale” .

